



crystals

Ice Crystals

Edited by
Yoshinori Furukawa

Printed Edition of the Special Issue Published in *Crystals*

Ice Crystals

Ice Crystals

Special Issue Editor

Yoshinori Furukawa

MDPI • Basel • Beijing • Wuhan • Barcelona • Belgrade



Special Issue Editor

Yoshinori Furukawa

Hokkaido University

Japan

Editorial Office

MDPI

St. Alban-Anlage 66

4052 Basel, Switzerland

This is a reprint of articles from the Special Issue published online in the open access journal *Crystals* (ISSN 2073-4352) in 2019 (available at: https://www.mdpi.com/journal/crystals/special_issues/Ice-Crystals).

For citation purposes, cite each article independently as indicated on the article page online and as indicated below:

LastName, A.A.; LastName, B.B.; LastName, C.C. Article Title. *Journal Name* **Year**, Article Number, Page Range.

ISBN 978-3-03921-890-5 (Pblk)

ISBN 978-3-03921-891-2 (PDF)

© 2019 by the authors. Articles in this book are Open Access and distributed under the Creative Commons Attribution (CC BY) license, which allows users to download, copy and build upon published articles, as long as the author and publisher are properly credited, which ensures maximum dissemination and a wider impact of our publications.

The book as a whole is distributed by MDPI under the terms and conditions of the Creative Commons license CC BY-NC-ND.

Contents

About the Special Issue Editor	vii
Yoshinori Furukawa	
Ice Crystals	
Reprinted from: <i>Crystals</i> 2019, 9, 540, doi:10.3390/crust9100540	1
Adiel F. Perez, Kyle R. Taing, Justin C. Quon, Antonia Flores and Yong Ba	
Effect of Type I Antifreeze Proteins on the Freezing and Melting Processes of Cryoprotective Solutions Studied by Site-Directed Spin Labeling Technique	
Reprinted from: <i>Crystals</i> 2019, 9, 352, doi:10.3390/crust9070352	3
Jingyi Mo, Robert D. Groot, Graham McCartney, Enyu Guo, Julian Bent, Gerard van Dalen, Peter Schuetz, Peter Rockett and Peter D. Lee	
Ice Crystal Coarsening in Ice Cream during Cooling: A Comparison of Theory and Experiment	
Reprinted from: <i>Crystals</i> 2019, 9, 321, doi:10.3390/crust9060321	18
Qiang Zeng and Kefei Li	
Quasi-Liquid Layer on Ice and Its Effect on the Confined Freezing of Porous Materials	
Reprinted from: <i>Crystals</i> 2019, 9, 250, doi:10.3390/crust9050250	32
Negative Thermal Expansivity of Ice: Comparison of the Monatomic mW Model with the All-Atom TIP4P/2005 Water Model	
Reprinted from: <i>Crystals</i> 2019, 9, 248, doi:10.3390/crust9050248	48
Lihua Wan, Xuebing Zhou, Peili Chen, Xiaoya Zang, Deqing Liang and Jinan Guan	
Decomposition Characterizations of Methane Hydrate Confined inside Nanoscale Pores of Silica Gel below 273.15 K	
Reprinted from: <i>Crystals</i> 2019, 9, 200, doi:10.3390/crust9040200	59
Kenji Mochizuki and Masakazu Matsumoto	
Collective Transformation of Water between Hyperactive Antifreeze Proteins: RiAFPs	
Reprinted from: <i>Crystals</i> 2019, 9, 188, doi:10.3390/crust9040188	76
Jinxiang Liu, Yujie Yan, Youguo Yan and Jun Zhang	
Tetrahydrofuran (THF)-Mediated Structure of THF-(H ₂ O) _{n=1-10} : A Computational Study on the Formation of the THF Hydrate	
Reprinted from: <i>Crystals</i> 2019, 9, 73, doi:10.3390/crust9020073	86

About the Special Issue Editor

Yoshinori Furukawa is Professor Emeritus at the Institute of Low Temperature Science (ILTS) at Hokkaido University, Sapporo, Japan. He obtained his Ph.D. in 1981 in Geophysics at Hokkaido University, where he earlier graduated. Prof. Furukawa has pursued his professional carrier in research at the ILTS from 1978 to 2016 and has been the Director of ILTS in the period of 2011–2014. He has been Visiting Scientist at the Desert Research Institute at the University of Nevada System (USA, 1985–1987) as well as the University of Washington, (USA 1995). He has been also Visiting Professor at the Institute for Solid State Physics at the University of Tokyo (Japan, 2002) and at the Institute of Space and Astronautical Science at the Japan Aerospace Exploration Agency (Japan, 2007–2010). He has served as President of the Japanese Association for Crystal Growth (JACG, 2012–2014). He is also Associate Editor for the *Journal of Crystal Growth* (2006–present). He received the Award of the Japanese Society of Snow and Ice (1991), the JACG Best Paper Award (1994), the Best Paper Award of the Society for Science on Form, Japan (2015), and numerous other accolades. Concerning ice, his research is focused on crystal growth, surface structure and pattern formation. In 2008, he successfully demonstrated, for the first time, ice crystal growth at the International Space Station.

Editorial

Ice Crystals

Yoshinori Furukawa

Institute of Low Temperature Science, Hokkaido University, Sapporo 060-0819, Japan;
frkw@lowtem.hokudai.ac.jp

Received: 17 October 2019; Accepted: 19 October 2019; Published: 19 October 2019

Abstract: The special issue on “Ice Crystals” includes seven contributed papers, which give the wide varieties of topics related to ice crystals. They focus on the interface structure of ice, the physical properties of hydrate crystals and the freezing properties of water controlled by antifreeze proteins. The present issue can be considered as a status report reviewing the research that has been made recently on ice crystals. These papers provide research information about the recent development of ice crystal research to readers.

Keywords: ice crystal

Ice crystals are the most ubiquitous material in the cryosphere environment of the Earth, in the planetary system, and also in our daily lives. In recent years, ice crystals have increased in importance as one of the key materials for finding solutions to settle various environmental concerns at a global scale. Furthermore, ice crystals are also expected as one of the unique materials which are extremely useful to various applications, for example, the food sciences, medical sciences, and other various fields. Dealing with these interesting subjects, research on ice crystals has been more actively pursued in recent years.

Since research on ice crystals is included in many different fields, communications and discussions among researchers are not sufficient, nor are they smooth. Publications related to ice crystals are also distributed in various journals, such as those dealing with physics, chemistry, biology, geoscience, planetary science, crystal growth, and others. Consequently, this special issue will provide a platform for discussion among the researchers working in different fields.

This special issue may include various subjects related to the structures, phase transitions, surface and interfaces, defects, crystal growth, clathrate hydrate, chemical properties, biological aspects, glaciological aspects, planetary aspects, and others for ice crystals, studied by theoretical, experimental, numerical and observational methods. This special issue presents seven papers, covering phase transition, surface and interface, clathrate, and biological aspects. Here we will briefly summarize the contents of papers appeared in this issue.

Two contributions related to the structures and physical properties of ice crystals confined in nanoscale porous materials. Zeng and Li [1] discussed the formation of the quasi-liquid layer (QLL) at the interface between the confined ice and the pore walls. Freezing of the water confined in thin pores can be destructive to the porous frame, but the effect of QLL remains still far from being fully understood. They clarified that the existence of QLL at the interface narrows the gaps between the predicted and measured freezing deformations. On the other hand, Wan et al. [2] discussed the decomposition of methane hydrate confined inside the nanoscale pores of silica gel.

Computer simulation studies for ice crystals are important in order to understand the structure and the dynamic properties of ice. This special issue includes three interesting papers related to the computer simulation. Huda et al. [3] discussed the origin of negative thermal expansivity of ice crystal, which has been experimentally observed at low temperature conditions. They first showed that the original monatomic water model using the quasi-harmonic approximation could not this

property of ice, but a simple prescription, namely re-adjusting a so-called tetrahedrality parameter, proposed to recover the negative thermal expansion. This is an interesting result to understand one of the mysterious ice crystal properties. Liu et al. [4] discussed the formation mechanism of THF hydrate based on the ab initio calculations and ab initio molecular dynamics simulations. They found that weak hydrogen bonds exist between THF and water molecules. This finding suggests that the THF can promote water molecules from the planar pentagonal or hexagonal ring. On the other hand, Mochizuki and Matsumoto [5] presents an interesting paper related to the activities of antifreeze proteins. It is well-known that antifreeze proteins protect organisms living in subzero environments from freezing injury, which render them potential applications for cryopreservation of living cells, organs, and tissues. They clarified that the water molecules confined between a pair of insect hyperactive antifreeze proteins is discontinuously expelled as the two proteins approach each other at a certain distance.

Another article related to the antifreeze protein was presented by Perez et al. [6] They assessed the function of antifreeze proteins in the solution of cryoprotective agents such as glycerol and propylene glycol, we have the applied site-directed spin labeling technique to a Type I antifreeze protein. They finally illustrate that antifreeze proteins can also play an active role in cryoprotective agent solutions for cryopreservation applications.

The last paper published in this special issue was an interesting and unique one. Mo et al. [7] discussed the ice crystal coarsening in ice cream during the cooling process. Ice cream is a complex multi-phase structure and its perceived quality is closely related to the small size of ice crystals in the product. Consequently, quantitative understanding of the coarsening process of ice particles is important to optimize the manufacturing process of ice cream. They discuss the relation between the coarsening process and the sugar concentration in ice cream.

In conclusion, this special issue presents advances in recent studies about ice crystals and provides helpful information for future studies related to ice crystals.

Acknowledgments: I thank all the authors who contributed to this special issue for preparing interesting papers.

Conflicts of Interest: The author declare no conflict of interest.

References

- Zeng, Q.; Li, K. Quasi-Liquid Layer on Ice and Its Effect on the Confined Freezing of Porous Materials. *Crystals* **2019**, *9*, 250. [[CrossRef](#)]
- Wan, L.; Zhou, X.; Chen, P.; Zang, X.; Liang, D.; Guan, J. Decomposition Characterizations of Methane Hydrate Confined inside Nanoscale Pores of Silica Gel below 273.15 K. *Crystals* **2019**, *9*, 200. [[CrossRef](#)]
- Huda, M.M.; Yagasaki, T.; Matsumoto, M.; Tanaka, H. Negative Thermal Expansivity of Ice: Comparison of the Monatomic mW Model with the All-Atom TIP4P/2005 Water Model. *Crystals* **2019**, *9*, 248. [[CrossRef](#)]
- Liu, J.; Yan, Y.; Yan, Y.; Zhang, J. Tetrahydrofuran (THF)-Mediated Structure of THF·(H₂O)_{n=1–10}: A Computational Study on the Formation of the THF Hydrate. *Crystals* **2019**, *9*, 73. [[CrossRef](#)]
- Mochizuki, K.; Matsumoto, M. Collective Transformation of Water between Hyperactive Antifreeze Proteins: RiAFPs. *Crystals* **2019**, *9*, 188. [[CrossRef](#)]
- Perez, A.F.; Taing, K.R.; Quon, J.C.; Flores, A.; Ba, Y. Effect of Type I Antifreeze Proteins on the Freezing and Melting Processes of Cryoprotective Solutions Studied by Site-Directed Spin Labeling Technique. *Crystals* **2019**, *9*, 352. [[CrossRef](#)]
- Mo, J.; Groot, R.D.; McCartney, G.; Guo, E.; Bent, J.; van Dalen, G.; Schuetz, P.; Rockett, P.; Lee, P.D. Ice Crystal Coarsening in Ice Cream during Cooling: A Comparison of Theory and Experiment. *Crystals* **2019**, *9*, 321. [[CrossRef](#)]



© 2019 by the author. Licensee MDPI, Basel, Switzerland. This article is an open access article distributed under the terms and conditions of the Creative Commons Attribution (CC BY) license (<http://creativecommons.org/licenses/by/4.0/>).

Article

Effect of Type I Antifreeze Proteins on the Freezing and Melting Processes of Cryoprotective Solutions Studied by Site-Directed Spin Labeling Technique

Adiel F. Perez, Kyle R. Taing, Justin C. Quon, Antonia Flores and Yong Ba *

Department of Chemistry and Biochemistry, California State University, Los Angeles, 5151 State University Drive, Los Angeles, CA 90032, USA

* Correspondence: yba@calstatela.edu; Tel.: +1-323-343-2360

Received: 19 April 2019; Accepted: 9 July 2019; Published: 11 July 2019

Abstract: Antifreeze proteins (AFPs) protect organisms living in subzero environments from freezing injury, which render them potential applications for cryopreservation of living cells, organs, and tissues. Cryoprotective agents (CPAs), such as glycerol and propylene glycol, have been used as ingredients to treat cellular tissues and organs to prevent ice crystal's formation at low temperatures. To assess AFP's function in CPA solutions, we have the applied site-directed spin labeling technique to a Type I AFP. A two-step process to prevent bulk freezing of the CPA solutions was observed by the cryo-photo microscopy, i.e., (1) thermodynamic freezing point depression by the CPAs; and (2) inhibition to the growth of seed ice crystals by the AFP. Electron paramagnetic resonance (EPR) experiments were also carried out from room temperature to 97 K, and vice versa. The EPR results indicate that the spin labeled AFP bound to ice surfaces, and inhibit the growths of ice through the bulk freezing processes in the CPA solutions. The ice-surface bound AFP in the frozen matrices could also prevent the formation of large ice crystals during the melting processes of the solutions. Our study illustrates that AFPs can play an active role in CPA solutions for cryopreservation applications.

Keywords: antifreeze protein; spin labeling; cryo-photo microscopy; electron paramagnetic resonance; cryoprotective agent; ice crystal

1. Introduction

Antifreeze proteins (AFPs) and antifreeze glycoproteins (AFGPs) protect organisms living in subzero environments from freezing injury, and even death [1–10]. The mechanism relies on inhibiting the growth of seed ice crystals, and the recrystallization of ice [11]. Type I AFPs have α -helical secondary structures with molecular weights in the range of 3.3–4.5 kDa [4,12–14]. The HPLC6 isoform of type I AFPs [12,13,15–19] has the amino acid sequence: DTASDAAAAAL TAANAKAAEL TAANAAAAATAR, which contains three 11-residue repeat units beginning with Thr residues [15,20–23]. It was reported that HPLC6 peptides bind to the 12 equivalent bipyramidal planes of ice Ih (hexagonal ice) along the <1 1 0 2> direction [24]. Thus, the binding of the AFP to these surfaces confines the growth of ice crystal to a bipyramidal shape [25–27]. Many experimental results from the studies of mutagenesis and their antifreeze activities [27–33], solid-state NMR [17–19], and site-directed spin labeling technique [34] have demonstrated that the underlined residues in the above sequence bind to the ice surface.

It was also discovered that some northern fishes, such as rainbow smelt, *Osmerus mordax dentex*, produced glycerol in addition to AFPs when the seawater was at subzero temperatures to avoid freezing by increasing the osmolality of their body fluids [35]. The concentration of glycerol was found to be temperature dependent. Because glycerol did not appear to be widely distributed among arctic fishes, it was, thus, suggested that two potential problems might be associated with the smelt

antifreeze proteins, including not being entirely effective in stopping ice growth, and being excluded from cells because of its small molecular size, which in turn provided limited freezing protection to cells. Therefore, glycerol might be a solution against freezing damage because it is nontoxic at low concentrations, and could also freely pass through cell membranes to lower the freezing points of water on both sides through colligative effect. It was proposed that antifreeze proteins are the first line of defense against freezing, while glycerol production is reserved as a backup for the time when minimum temperatures were encountered.

AFPs are potentially useful for cryopreservation of living cells, tissues, and organs [36]. Cryopreservation is a method for long-term preservation of living substances at low temperatures without causing fatal freezing damage [37]. Cryoprotective agents (CPAs), such as glycerol, dimethyl sulfoxide, and propylene glycol, have been used as the major ingredients of CPA solutions to treat cellular tissues and organs to prevent the formation of ice crystals, which may cause cell and tissue damages [38]. We believe that the addition of AFPs to CPA solutions could add an additional protective mechanism for cryopreservation applications.

Glycerol was also used as a major ingredient of antifreeze fluids in automotive applications [39] before being replaced by ethylene glycol. The latter has a lower freezing point. Glycerol is non-toxic at low concentration and non-corrosive as well, while can withstand relatively high temperatures. Deicing and anti-icing fluids, used in surface applications to melt ice and prevent ice formation in winter, respectively, are typically composed of ethylene glycol or propylene glycol, along with other additives, such as thickening agents, surfactants, corrosion inhibitors, and colored UV-sensitive dyes. These additives could be toxic to environments. Ethylene glycol is toxic to living organisms, and could remain in the ground even during rainfall because it has high adhesion to soil. Propylene glycol is considerably less toxic, and has lower adhesion to soil. Thus, propylene glycol has high mobility in soil and potentially leaches into groundwater, while being rapidly degraded in all environmental media [40]. Research in the area of antifreeze fluidics is significantly towards the direction for ecological environment. Thus, the use of AFPs as an active ingredient in deicing and anti-icing fluids could enhance their antifreeze property, and meanwhile is eco-friendly.

In this study, site-directed spin labeling (SDSL) technique [34,41–49] was used to study the effect of type I AFPs on the freezing and melting processes of solutions comprised of glycerol, and propylene glycol, respectively, through analyzing the cryo-photo microscopic images of ice crystals, and the EPR (electron paramagnetic resonance) spectra. The molecular information obtained from the EPR spectra and the microscopic information from the observed ice crystals provide complementary information to show how the AFP interacted with ice surfaces and the surrounding solutions during the freezing and melting processes.

2. Materials and Methods

2.1. Materials

The wild Type I AFPs were purchased from A/F Protein Inc. (Waltham MA, USA) (99%). The cysteine-substituted HPLC6 isoforms of type I AFPs in the 23rd leucine residue (L23C), and the 17th alanine residue (A23C), respectively, were synthesized by Biomatik Corporation (Wilmington, Delaware). The purities of the peptides are > 95%. L23C has the following sequence DTASDAAAAAALTAANAKAAECTAANAAAAAATAR, and A17C has the following sequence DTASDAAAAAALTAANCKAAAELTAANAAAAAATAR, where the underlined residues bind to ice surface [17–19,34,50–53]. The L23C cysteine side chain points to the water phase [34] after binding to the ice surface, while the A17C cysteine replaced the ice binding alanine residue. The MSL (4-maleimido-2, 2,6,6-tetramethyl-1-piperidinyloxy) spin label was purchased from Sigma-Aldrich (CAS Number 15178-63-9). Dialysis tubes with a membrane mesh size of 1 kDa were purchased from Sigma-Aldrich (CAS Number PURD10005-1KT). Phosphate buffered saline tablets (Cas # BP2944-100) were purchased from Fisher Scientific to make the buffer solution at pH 7.4.

2.2. Syntheses of the Spin Labeled HPLC6 Peptides

One (1.0) mg of L23C peptides were dissolved in a 0.5 mL pH 7.4 buffer solution held in an Eppendorf vial (2-mL volume), and 1.565 mg of MSL was dissolved in a 0.25 mL 100% ethanol. The two solutions were mixed in a vial. The vial was wrapped with aluminum foil, and the reaction took place under shaking conditions via a vortex mixer for 2–4 h in a 4 °C cold room. Then, the sample was lyophilized. The obtained solid powder was dissolved in 0.5 mL deionized (DI) water and transferred into a dialysis tube. The dialysis was done in DI water at 4 °C. Several changes of water were made at 1 h, 2 h, 4 h, 6 h, and overnight. The dialyses were continued for a longer time (if needed) until no EPR signal could be detected in the DI water. The purified products were lyophilized and stored in a –20 °C freezer.

A MALDI-TOF mass spectrometer (Voyager-DE™ STR Biospectrometry™ Workstation) was used to verify the masses of the spin-labeled L23C and A17C HPLC6 mutants. The matrix was comprised of alpha-cyano-4-hydroxycinnamic acid, 3% TFA, acetonitrile, and DI water. The mass spectra of the original L23C and A17C peptides, and their spin-labeled products have been provided in the supplemental file of our previous publication [34].

2.3. EPR Experiments and Line-Shape Simulations

Three solutions were analyzed by the EPR method, including 2.0 mg/mL of the spin-labeled L23C peptide in DI water, that in 5 (volume) % glycerol, and that in 5 (volume) % propylene glycol. Solutions were placed in individual capillaries and fire sealed. The capillaries were immersed in hexane solvent in EPR tubes.

EPR experiments were carried out using a Bruker X-Band CW EMX EPR Spectrometer (Bruker BioSpin Corporation, Billerica, MA, USA). The following EPR parameters were used: Center field—3360.880 G; sweep width—300.00 G; resolution—1024 points; time constant—0.640 ms; sweep time—5.243 s; modulation frequency—100.0 kHz; and modulation amplitude—1.00 G. X-band frequencies from 9.445 to 9.460 GHz were used. Sample temperatures were controlled using an ER 4141VT-UM nitrogen variable-temperature system (77–500 K). EPR temperature readings were corrected using a thermocouple with iced water. Samples were first run at room temperature, then at lower temperatures using heater-regulated cold nitrogen gas generated from a liquid-nitrogen tank. When the assigned temperature was reached (usually in 5–10 min, depending on the cooling conditions), the temperature was maintained for five more minutes. We repeatedly ran the EPR spectra at the same temperatures for a longer time to ensure that the EPR spectra did not change any further after 5 min.

Rotational correlation times of the spin label, along with the component line-shapes, were calculated for each EPR spectrum. Theoretical simulations of the EPR spectra of the spin-labeled peptides were performed using the Multi-Component EPR Fitting program (version 742) and LabVIEW software. This EPR simulation program was developed by Dr. Christian Altenbach (University of California, Los Angeles, CA, USA) [54–56].

2.4. Cryo-Photo Microscopic Method

Optical observations of the ice crystals in the AFP solutions were carried out with a set of equipment, including a custom-built Otago nanoliter osmometer, a thermoelectric temperature controlling device with a temperature-controlled cooling stage, an Olympus BX 51 microscope (maximum magnification 800× with a resolution of 1 micron), and a RETIGA 2000R Color Video Camera. The temperature sensor is placed directly on the sample holder; thus, providing a sensitive temperature probe with the accuracy of the temperature reading within ±0.01 °C. The temperature was controlled through the electrical thermostat on the stage, and the cooling process was assisted by heat exchange with 50% isopropyl flowing through tubing at –15 °C by the aid of two cooling pumps cooling at –2 °C and –20 °C, respectively.

3. Results and Discussion

3.1. The Growths of Ice Crystals in the Spin-Labeled L23C and A17C CPA Solutions

A seed ice crystal in an AFP solution was initiated by rapidly decreasing the temperature of the sample approximately four degrees per second until reaching $-10\text{ }^{\circ}\text{C}$, then continue decreasing until reaching $-20\text{ }^{\circ}\text{C}$ with a rate of six degrees per second, referred to as flash-freezing. After flash freezing the whole solution to a low temperature ($<-20\text{ }^{\circ}\text{C}$), the temperature was raised to $-10\text{ }^{\circ}\text{C}$ at a rate of four degrees per second, then the temperature was slowly increased to the melting point of the frozen bulk solution. From this point on, the temperature was manually controlled with a rate of $\pm 0.01\text{ }^{\circ}\text{C}$. The temperature was then varied around the bulk melting point to capture a seed ice crystal. A seed ice crystal had to grow on the basal planes with the decrease in temperature due to the binding of AFP to the other facets, and its shape was finally confined to a bipyramid by the AFP while the rest of the solution stayed in super-cooled condition. Further lowering the temperature to a point allowed the ice crystal to grow abruptly (the so-called ‘burst’ in literature) typically from the tips of the bipyramid and spreading into the whole solution. Figure 1a shows the cryo-photo microscopic images of the growth of an ice crystal in a 2.0 mg/mL spin-labeled L23C water solution (solution a), (b) shows those in a 2.0 mg/mL spin-labeled L23C in a 5% glycerol solution (solution b), and (c) shows those in a 2.0 mg/mL spin-labeled L23C in a 5% propylene glycol solution (solution c). All the ice crystals were confined to bipyramidal shapes when the temperatures were decreased to some points, and the ice crystals eventually burst into the solutions at further lowered temperatures. We define the *antifreeze activity* of an AFP as the difference between the melting point of the single ice crystal and the bursting point of the single ice crystal in an AFP solution. (The antifreeze activity so defined was also called thermal hysteresis in most other publications. Here, we focus on the behavior of a single ice crystal in an AFP solution, while the definition of thermal hysteresis emphasizes the bulk freezing property of an AFP solution.) For example, the melting point of the single ice crystal in the spin labeled AFP water solution was $0.0\text{ }^{\circ}\text{C}$, and the bursting point of the ice crystal was $-0.29\text{ }^{\circ}\text{C}$. Thus, the antifreeze activity of the spin labeled AFP in water is $0.29\text{ }^{\circ}\text{C}$ in the 2.0 mg/mL AFP solution. The melting points of the other two ice crystals in solution (b) and solution (c) were $-0.79\text{ }^{\circ}\text{C}$ and $-1.70\text{ }^{\circ}\text{C}$, respectively, and the corresponding bursting points of these single ice crystals were $-1.08\text{ }^{\circ}\text{C}$ and $-1.99\text{ }^{\circ}\text{C}$, resulting in antifreeze activities of $0.29\text{ }^{\circ}\text{C}$ in both of the CPA solutions. To compare with the negative control, spin labeled A17C, we have also studied the behaviors of ice crystals in the A17C CPA solutions. Figure 1d,e show the growths of ice crystals in a 2.0 mg/mL spin-labeled A17C in the 5% glycerol solution, and those in the 5% propylene glycol solution, respectively. As expected, the seed ice crystals grew into sheet-like shapes, showing that the ice crystals grew primarily on the prisms because the spin labeled A17C did not bind to the ice surfaces.

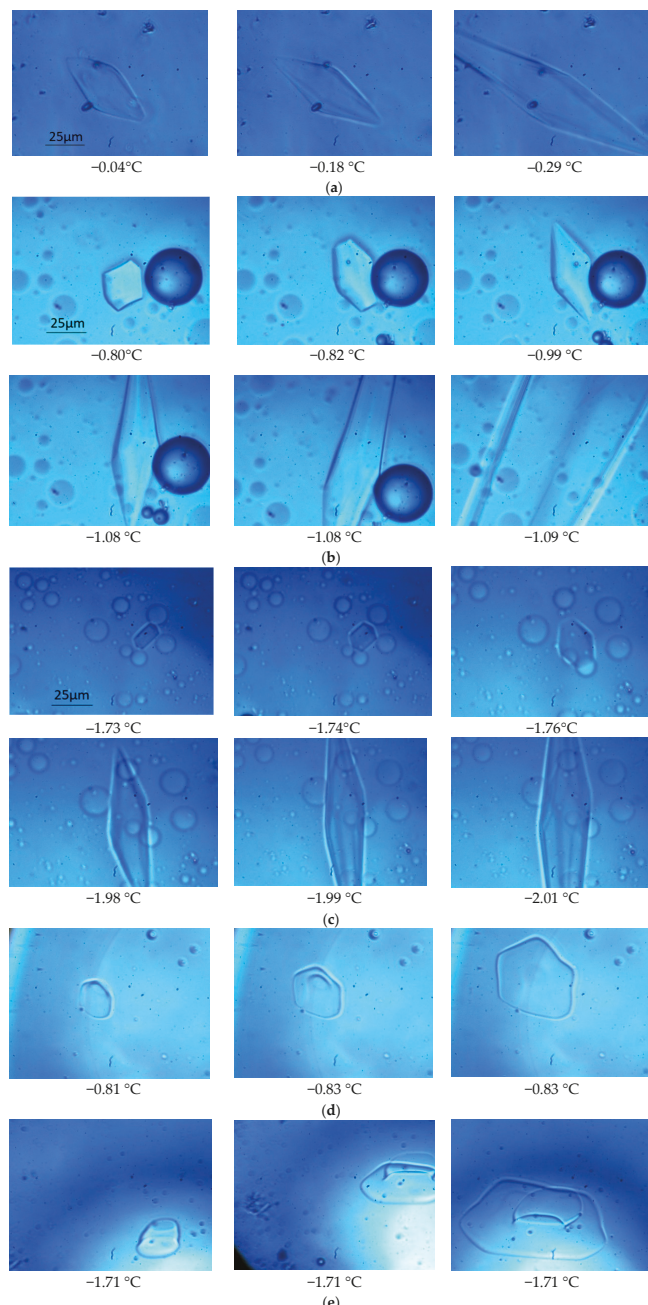


Figure 1. Cryo-photo microscopic images of ice crystals confined by 2.0 mg/mL spin-labeled L23C in (a) water; (b) 5% glycerol solution, and (c) 5% propylene glycol solution, and (d) and (e) cryo-photo microscopic images of ice crystals grown in the 2.0 mg/mL spin labeled A17C in the 5% glycerol solution, and 5% propylene glycol solution, respectively. (The differences in hue were caused by different filters used when the images were taken, and the bubbles were caused by the dissolved air in the solutions.)

Figure 2a shows the melting and bursting points of the ice crystals versus the concentrations of the spin-labeled L23C in water and the CPA solutions. (See the inset for the belongings of the curves.) It shows that the melting points of the ice crystals in these solutions did not vary with the increase of the concentrations of the spin-labeled AFP, but the bursting points decreased. Figure 2b shows the antifreeze activities of the spin-labeled AFP in these solutions at different concentrations. It shows that all the antifreeze activities of the spin labeled AFPs were the same at the same AFP concentrations in the three solutions although the melting points and bursting points of the ice crystals in these solutions with the same AFP concentrations were different. The results indicate that the antifreeze activities solely reflects the effect of the AFP on inhibiting the growth of ice crystals in the water and CPA solutions. It appears that the CPAs did not have a collaborative effect on the antifreeze activities. Thus, the experimental results show a two-step process to prevent ice growths in the AFP CPA solutions, i.e., (1) the thermodynamic freezing point depressions by glycerol and propylene glycol, respectively; and (2) inhibition to the growth of seed ice crystals by the AFPs.

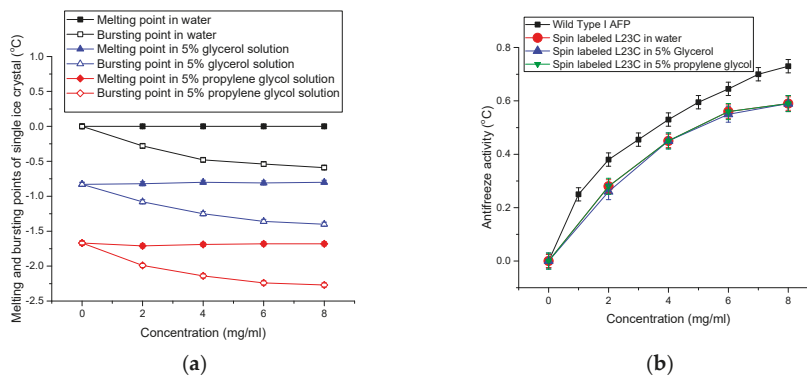


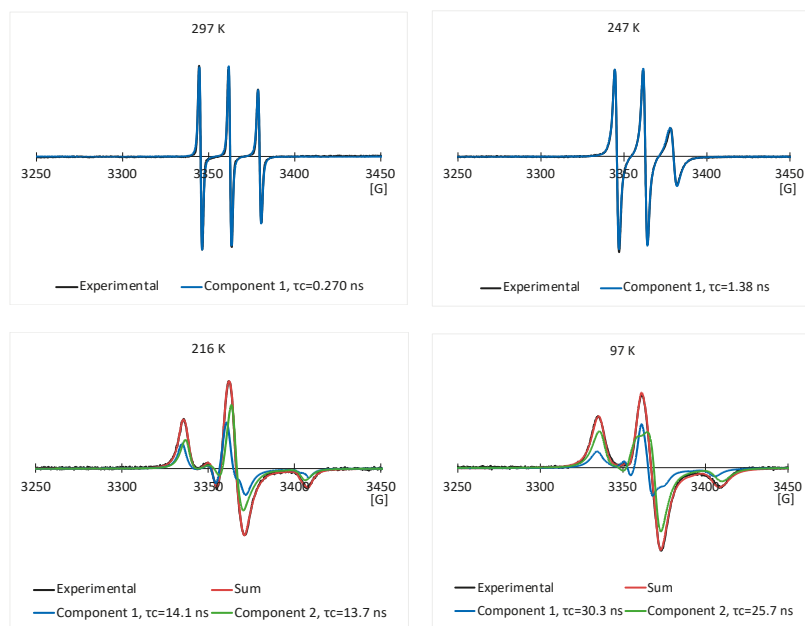
Figure 2. (a) Melting and bursting points of ice crystals in the spin labeled L23C water, 5% glycerol, and 5% propylene glycol solutions, respectively; and (b) antifreeze activities of the wild Type I AFP, and the spin-labeled L23C in water, 5% glycerol and 5% propylene glycol solutions, respectively.

For comparison, the antifreeze activities of wild Type I AFPs in water are also given in Figure 2b. The antifreeze activities of the spin-labeled L23C are a little lower than those of the wild type I AFPs. Although the spin label was attached to the non-ice binding residue, which faces the water phase, the antifreeze activities were affected to some extent. This is also true for a few other spin-labeled type I AFPs on other non-ice binding residues [34]. The experimental results indicate that the binding constant of an AFP to the ice surface is determined by both the ice-binding motifs and the properties of other residues. We believe that the binding of AFP to ice surface induced a Water-AFP-Ice (WAI) interphase between the ice phase and water phase [57]. The concentration of AFP in the interphase is much higher than that in the bulk water phase, thus the lowered freezing point of water in the interphase. The spin label is hydrophobic and bulkier than the replaced leucine side chain, which slightly changed the balance between the hydrophobicity and hydrophilicity of the wild type I AFP, resulting in a decreased spontaneity to form the WAI interphase, and, thus, less antifreeze activity. This behavior shows the nature of thermodynamic equilibrium of AFP's ice binding. Otherwise, if the binding of AFP to ice surface were irreversible, all kinds of AFPs would have the same antifreeze activity, which would disagree with literature on this subject. Our theoretical model is the ice surface adsorption enhanced the colligative effect of AFPs in the WAI interphase [57]. An AFP's antifreeze activity is determined by the decreased Gibbs energy of the WAI interphase leading to the decreased freezing point in the interphase. A larger binding constant makes the AFP's concentration higher in the WAI interphase; thus a lowered freezing point of water in the WAI interphase. The WAI interphase

acts as a thermodynamic barrier between the ice phase and the water phase. The ice phase was in thermal equilibrium with the WAI interphase while the water phase was in super-cooled condition.

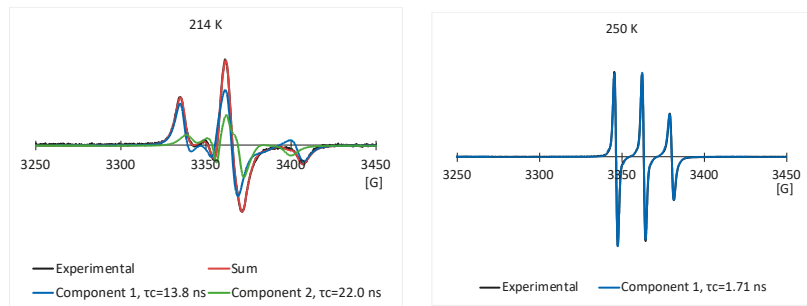
3.2. EPR Results of the Spin Labeled Type I AFP in the CPA Solutions

Figure 3a,b show some typical experimental EPR spectra, and their simulated EPR spectra of the 2.0 mg/mL spin labeled L23C in the 5% glycerol solution through the freezing process, and melting process, respectively. The temperatures and corresponding correlation times are given in the inset of the spectra. The nitroxide radical has a triplet EPR spectrum, due to the coupling of the electron spin with the ^{14}N nucleus spin. Narrow lineshape shows free tumbling of the molecule in a solution. With the decrease in temperature, the lineshape became broader, showing the restricted motion of the spin labels, due to the freezing of the solution. Spectral simulation allows us to obtain the rotational correlation time (τ_c) for the motion of the spin labels, and also possibly the number of components included in the spectrum. For a random molecular tumbling, τ_c roughly corresponds to the average time for a molecule to progress through one radian. Here, the correlation time primarily represents that of chemical bond rotation of the MSL spin label, while the tumbling of the whole spin labeled AFP was much slower, especially after the solutions were frozen. Figure 4a,b show those of the 2.0 mg/mL spin labeled L23C in the 5% propylene glycol solution. The simulations show that one EPR spectral component existed at higher temperatures ($> \sim 245\text{ K}$), and minimum two components could fit the spectra well at lower temperatures for both the freezing and melting processes.



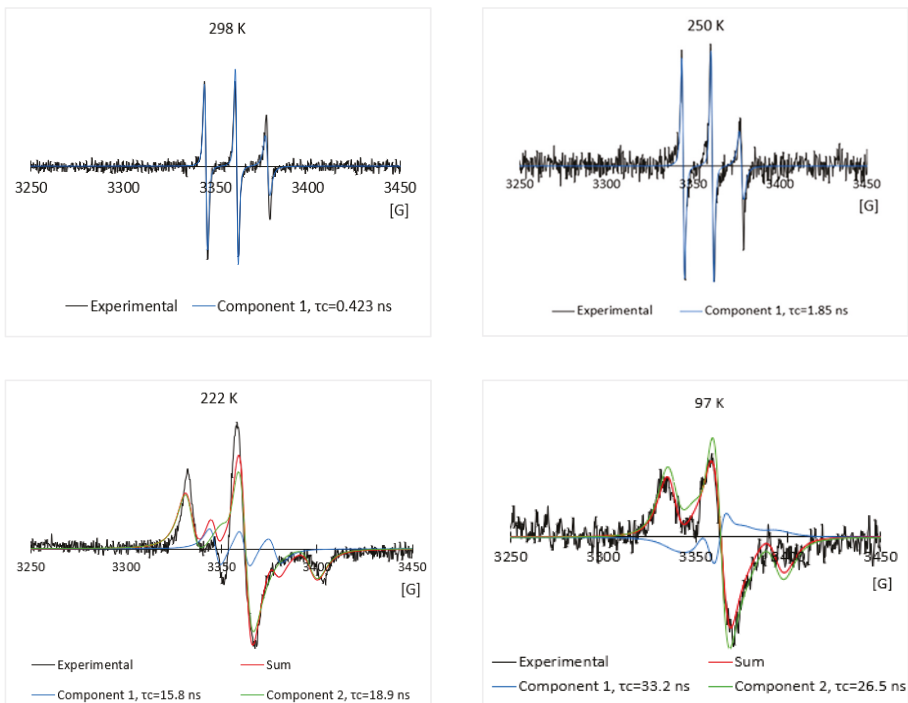
(a)

Figure 3. Cont.



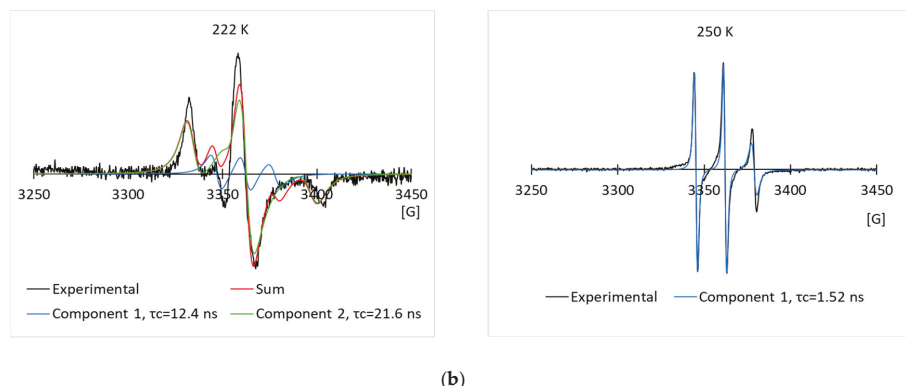
(b)

Figure 3. Typical experimental EPR spectra and their simulated EPR spectra of the 2.0 mg/mL spin labeled L23C in the 5% glycerol solution through the freezing process (a), and melting process (b), respectively.



(a)

Figure 4. Cont.



(b)

Figure 4. Typical experimental EPR spectra, and their simulated EPR spectra of the 2.0 mg/mL spin labeled L23C in the 5% propylene glycol solution through the freezing process (a), and melting process (b), respectively.

Figure 5a shows the curves of correlation times (τ_c) of the 2.0 mg/mL spin labeled L23C in the 5% glycerol solution versus temperature (T) through the freezing process and melting process, respectively. (See the inset for belongings of the curves.) The correlation times increased with the decrease in temperature in the freezing process, showing the decreased kinetic energy of the chemical bond rotation of the spin label, and also steric hindrance of the chemical bond rotation, due to the freezing of the surrounding fluid at low temperatures. The slope of the curve changed rapidly between 250.0 K and 230.0 K, and meanwhile, more than one component of the simulated EPR spectra started appearing at 243.0 K, which shows that the surroundings of the MSL spin labels began to freeze at temperatures below 245 K. To show the sharp changes of the curves more visually, dotted red lines were drawn through the average values of the three near linear regions. The two-component model allowed us to fit the EPR spectra well at low temperatures, while the one-component model yielded poor fitting. However, more-component models would also allow us to fit the EPR spectra at the low temperatures. Thus, the two-component model should be understood as the distribution of correlation times between the shorter one and the longer one of the two components. The correlation times increased rapidly from 230.0 to 210.0 K, and then turned to increase slowly until the lowest experimental temperature of 97.0 K. The steep slope ranging from 230.0 to 210.0 K indicates that freezing of the surroundings around the MSL spin labels progressed quickly, while the slow increase below 200 K indicates that the surroundings of the MSL spin labels became solidified although hardness of the frozen solution continued to increase until 97 K. As shown in Figure 5b, curves of the correlation times versus temperature for the spin labeled L23C in the propylene glycol solution are similar to those of the glycerol solution. The freezing processes monitored by the spin labels attached to the L23C in the CPA solutions were quite different from that in water [34]. The latter showed a sharp local phase transition at 251.6 K. However, no sharp phase transitions were observed in the CPA solutions. The freezing curves in Figure 5a,b illustrate that the eutectic points decreased with the decrease in temperature, due to the increased amount of ice, which made the concentrations of the CPAs in the solution phases higher at lower temperatures. Distributions of the correlation times during the freezing processes indicate the heterogeneous environments surrounding different spin labels although not significant above 200 K. The spin labeled L23C bound to ice surfaces, while the spin labels interacted with water and glycerol, or propylene glycol in the WAI interphase during the freezing process. The thickness of the WAI interphase could have a distribution, which affected the mobility of the spin labels in a range. The solidified matrices below 200 K made the spin label's surroundings more anisotropic, thus broader distributions of the correlation times.

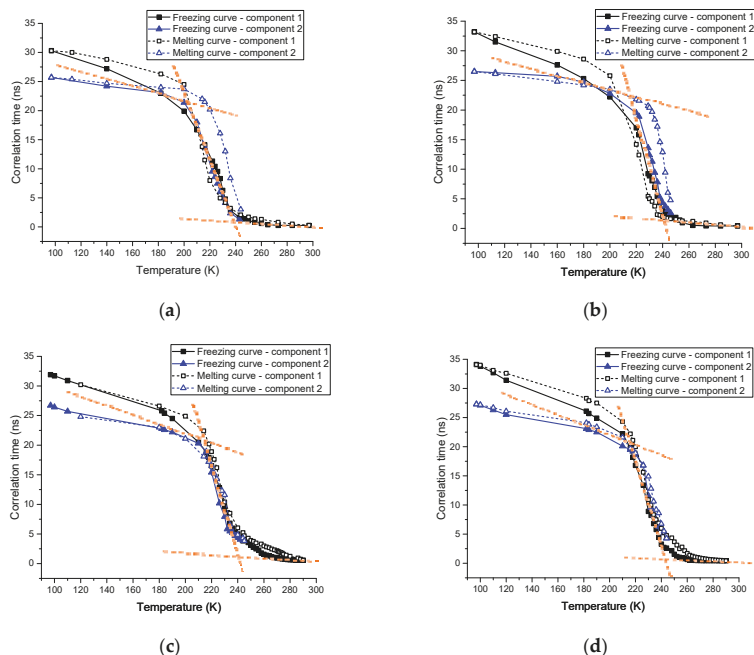


Figure 5. (a) Curves of correlation times (τ_c) of the 2.0 mg/mL spin labeled L23C in the 5% glycerol solution versus temperature through the freezing process, and melting process; (see the inset in the Figure.); (b) those of the 2.0 mg/mL spin labeled L23C in the 5% propylene glycol solution; (c) those of the 2.0 mg/mL spin labeled A17C in the 5% glycerol solution; and (d) those of the 2.0 mg/mL spin labeled A17C in the 5% propylene glycol solution.

Curves of the correlation times versus temperature through the melting processes are similar to those of the freezing processes, but with broader distributions of correlation times, and larger average correlation times than those of the freezing curves for both of the CPA solutions. Recall that a larger correlation time means less mobility of the spin label. Therefore, it appears that the spin labeled L23C inhibited the ice growth during the freezing processes of the CPA solutions, thus shorter correlation times compared with those during the melting processes at the same temperatures. In other words, the melting happened at closer thermal equilibrium temperatures. The broader distributions of the correlation times during the melting processes could indicate that the melting points (eutectic points) are not quite spatially homogeneous in the samples. As compared with the inactive spin labeled A17C below, this phenomenon can be related to the ice surface binding of spin labeled L23C possibly during the freezing processes.

To compare with the negative control, we have run the EPR experiments on the 2.0 mg/mL spin labeled A17C in the 5% glycerol solution, and the 5% propylene glycol solution through the freezing and melting processes. The experimental and simulated EPR spectra are shown in Figure 6a,b and Figure 7a,b respectively. As in the L23C CPA solutions, the two-component model was used to simulate the EPR spectra at low temperatures. Curves of the corresponding correlation times versus temperatures are shown in Figure 5c,d for the A17C in the glycerol, and propylene glycol solutions, respectively. Different from the spin labeled L23C CPA solutions, the freezing curves and melting curves are quite close, showing that the inactive spin labeled A17C did not bind to ice surfaces. As shown by the crossing points of the dotted red lines between 250 K and 230 K, the freezing point of the A17C CPA solutions were about five degrees higher than the L23C CPA solutions, further showing that the active spin labeled L23C inhibited the ice growths during the freezing process. Another

noticeable phenomenon is that the correlation times of the A17C CPA solutions decreased slower during the melting processes at temperatures higher than 240 K, which can also be observed on the corresponding EPR spectra in Figure 6 (260 K) and Figure 7 (248 K). The broader EPR linewidths during the melting processes indicate slower rotational motions, or longer correlation times of the spin labels. This phenomenon shows that the spin labeled A17C peptides did not bind to ice surfaces, but were instead pushed to aggregate due to the freezing of the solutions. Thus, the dissolution process of the spin labeled A17C peptides could not be as fast as the individually ice surface bound spin labeled L23C peptides during the melting process. Results of the control experiments further indicate that the spin labeled L23C bound to ice surfaces during the frozen process and in the frozen CPA matrices.

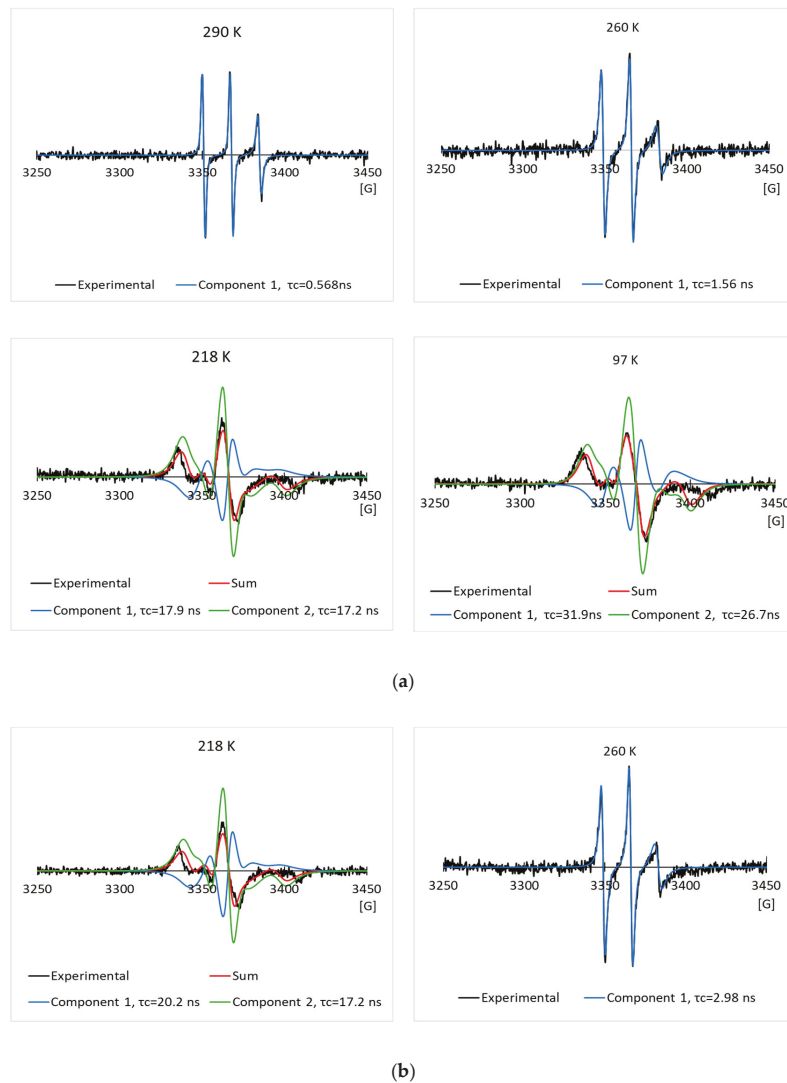


Figure 6. Typical experimental EPR spectra, and their simulated EPR spectra of the 2.0 mg/mL spin labeled A17C in the 5% glycerol solution in the freezing process (a), and melting process (b), respectively.

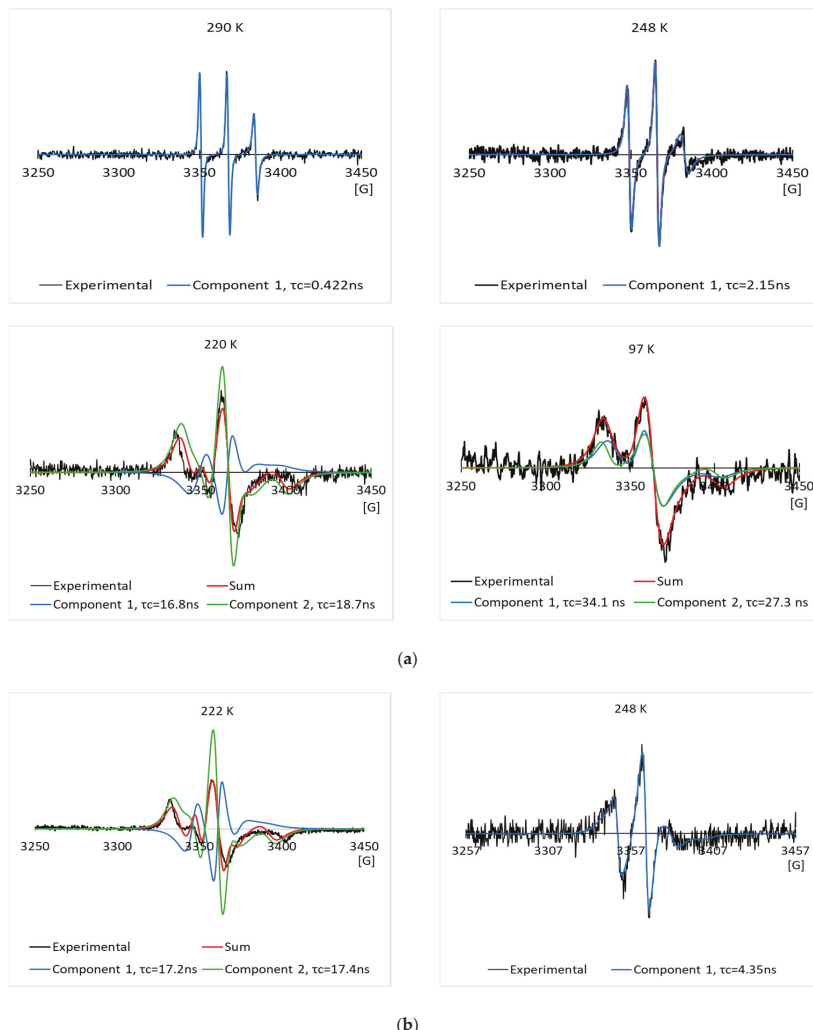


Figure 7. Typical experimental EPR spectra, and their simulated EPR spectra of the 2.0 mg/mL spin labeled A17C in the 5% propylene glycol solution in the freezing process (a), and melting process (b), respectively.

4. Conclusions

Both results of cryo-photo microscopy and EPR spectral analysis indicate that the spin labeled AFP bound to ice surfaces at all temperatures as long as ice formed in the CPA solutions. A two-step process, i.e., (1) thermodynamic freezing point depression by the CPAs, and (2) inhibition on the growth of ice crystals by the AFP, occurred to prevent the formation of bulk ice in the CPA solutions at low temperatures. The spin labeled AFP bound to ice surfaces during the bulk freezing process, and appeared to inhibit the ice growth in the CPA solutions at low temperatures. The ice surface bound AFP in the frozen bulk solutions could also prevent ice recrystallization during the melting process. We, therefore, conclude that AFPs are potentially useful as an active ingredient to make CPA solutions for preventing cryo-damages of living cells, organs and tissues, and for industrial applications.

Author Contributions: Conceptualization, Y.B.; methodology, Y.B., A.P., K.T., J.Q., and A.F.; software, Y.B., A.P., K.T., J.Q., and A.F.; validation, Y.B., A.P., K.T., J.Q.; formal analysis, Y.B., A.P., K.T., J.Q., and A.F.; investigation, Y.B., A.P., K.T., J.Q., and A.F.; resources, Y.B.; data curation, Y.B., A.P., K.T., J.Q., and A.F.; writing—original draft preparation, Y.B., A.P.; writing—review and editing, Y.B., A.P., K.T. and J.Q.; visualization, Y.B., A.P., K.T., J.Q., and A.F.; supervision, Y.B.; project administration, Y.B.; funding acquisition, Y.B.

Funding: This research was funded by the National Institute of General Medical Sciences (NIGMS) of the National Institutes of Health (NIH) (grant number R15GM106249). A.P. would also like to thank the NIGMS and NIH for support through the TWD RISE award (grant number 4R25GM049001).

Acknowledgments: The authors would like to thank Michael Bridges, Christian Altenbach, and the Hubbell Lab at the University of California, Los Angeles, for their invaluable assistance and providing the EPR simulation program.

Conflicts of Interest: The authors declare no conflict of interest. The funders had no role in the design of the study; in the collection, analyses, or interpretation of data; in the writing of the manuscript, or in the decision to publish the results.

References

1. DeVries, A.L.; Komatsu, S.K.; Feeney, R.E. Chemical and physical properties of freezing point-depressing glycoproteins from Antarctic fishes. *J. Biol. Chem.* **1970**, *245*, 2901–2908. [\[PubMed\]](#)
2. DeVries, A.L. Antifreeze peptides and glycopeptides in cold-water fishes. *Annu. Rev. Physiol.* **1983**, *45*, 245–260. [\[CrossRef\]](#) [\[PubMed\]](#)
3. Duman, J.G.; DeVries, A.L. Freezing behavior of aqueous solutions of glycoproteins from the blood of an Antarctic fish. *Cryobiology* **1972**, *9*, 469–472. [\[CrossRef\]](#)
4. DeVries, A.L.; Wohlschlag, D.E. Freezing resistance in some Antarctic fishes. *Science* **1969**, *163*, 1073–1075. [\[CrossRef\]](#) [\[PubMed\]](#)
5. Komatsu, S.; DeVries, A.L.; Feeney, R.E. Studies of the structure of freezing point-depressing glycoproteins from an Antarctic fish. *J. Biol. Chem.* **1970**, *245*, 2909–2913. [\[PubMed\]](#)
6. Feeney, R.E. A biological antifreeze. *Am. Sci.* **1974**, *62*, 712–719. [\[PubMed\]](#)
7. Feeney, R.E.; Yeh, Y. Antifreeze proteins from fish bloods. *Adv. Protein. Chem.* **1978**, *32*, 191–282. [\[PubMed\]](#)
8. Davies, P.L.; Hew, C.L. Biochemistry of fish antifreeze proteins. *FASEB J.* **1990**, *4*, 2460–2468. [\[CrossRef\]](#)
9. Cheng, C.H.; DeVries, A.L. Structures of antifreeze peptides from the antarctic eel pout, *Austrolycichthys brachycephalus*. *Biochim. Biophys. Acta* **1989**, *997*, 55–64. [\[CrossRef\]](#)
10. Duman, J.G.; Wu, D.W.; Olsen, T.M.; Urrutia, M.; Turaman, D. Thermal-Hysteresis Proteins. *Adv. Low Temp. Biol.* **1993**, *2*, 131.
11. Knight, C.A.; DeVries, A.L.; Oolman, L.D. Fish antifreeze protein and the freezing and recrystallization of ice. *Nature* **1984**, *308*, 295–296. [\[CrossRef\]](#) [\[PubMed\]](#)
12. Duman, J.G.; DeVries, A.L. Freezing resistance in winter flounder *Pseudopleuronectes americanus*. *Nature* **1974**, *247*, 237–238. [\[CrossRef\]](#)
13. Duman, J.G.; DeVries, A.L. Isolation, characterization and physical properties of protein antifreeze from the winter flounder *Pseudopleuronectes americanus*. *Comp. Biochem. Physiol.* **1976**, *54*, 375–380.
14. Hew, C.L.; Joshi, S.; Wang, N.-C.; Kao, M.-H.; Ananthanarayanan, V.S. Structure of shorthorn sculpin antifreeze polypeptides. *Eur. J. Biochem.* **1985**, *151*, 167–172. [\[CrossRef\]](#)
15. Sönichsen, F.D.; Davies, P.L.; Sykes, B.D. NMR structural studies on antifreeze proteins. *Biochem. Cell Biol.* **1998**, *76*, 284–293. [\[CrossRef\]](#)
16. Harding, M.M.; Ward, L.G.; Haymet, A.D. Type I ‘antifreeze’ proteins. Structure-activity studies and mechanisms of ice growth inhibition. *Eur. J. Biochem.* **1999**, *264*, 653–665. [\[CrossRef\]](#) [\[PubMed\]](#)
17. Mao, Y.; Lin, W.; Ba, Y. Antifreeze protein NMR sensor to detect water molecular reorientation in the surface of ice. *J. Chem. Phys.* **2009**, *131*, 101102. [\[CrossRef\]](#)
18. Mao, Y.; Jeong, M.; Wang, T.; Ba, Y. Threonine side chain conformational population distribution of a type I antifreeze protein on interacting with ice surface studied via ^{13}C – ^{15}N dynamic REDOR NMR. *Solid State Nucl. Magn. Reson.* **2011**, *39*, 7–13. [\[CrossRef\]](#)
19. Mao, Y.; Ba, Y. Insight into the Binding of Antifreeze Proteins to Ice Surfaces via ^{13}C Spin Lattice Relaxation Solid State NMR. *Biophys. J.* **2006**, *91*, 1059–1068. [\[CrossRef\]](#)
20. Sicheri, F.; Yang, D.S. Ice-binding structure and mechanism of an antifreeze protein from winter flounder. *Nature* **1995**, *375*, 427–431. [\[CrossRef\]](#)

21. Yang, D.S.; Sax, M.; Chakrabarty, A.; Hew, C.L. Crystal structure of an antifreeze polypeptide and its mechanistic implications. *Nature* **1988**, *333*, 232–237. [[CrossRef](#)] [[PubMed](#)]
22. Sicheri, F.; Yang, D.S.C. Structure determination of a lone α-helical antifreeze protein from winter flounder. *Acta Cryst. D* **1996**, *52*, 486–498. [[CrossRef](#)] [[PubMed](#)]
23. Gronwald, W.; Chao, H.; Reddy, D.V.; Davies, P.L.; Sykes, B.D.; Sönnichsen, F.D. NMR characterization of side chain flexibility and backbone structure in the type I antifreeze protein at near freezing temperatures. *Biochemistry* **1996**, *35*, 16698–16704. [[CrossRef](#)] [[PubMed](#)]
24. Knight, C.A.; Cheng, C.C.; DeVries, A.L. Adsorption of alpha-helical antifreeze peptides on specific ice crystal surface planes. *Biophys. J.* **1991**, *59*, 409–418. [[CrossRef](#)]
25. Wen, D.; Laursen, R.A. A model for binding of an antifreeze polypeptide to ice. *Biophys. J.* **1992**, *63*, 1659–1662. [[CrossRef](#)]
26. Chao, H.; DeLuca, C.I.; Davies, P.L. Mixing antifreeze protein types changes ice crystal morphology without affecting antifreeze activity. *FEBS Lett.* **1995**, *357*, 183–186.
27. Haymet, A.D.J.; Ward, L.G.; Harding, M.M. Winter Flounder “Antifreeze” Proteins: Synthesis and Ice Growth Inhibition of Analogue that Probe the Relative Importance of Hydrophobic and Hydrogen-Bonding Interactions. *J. Am. Chem. Soc.* **1999**, *121*, 941–948. [[CrossRef](#)]
28. Baardsnes, J.; Kondejewski, L.H.; Hodges, R.S.; Chao, H.; Kay, C.; Davies, P.L. New ice-binding face for type I antifreeze protein. *FEBS Lett.* **1999**, *463*, 87–91. [[CrossRef](#)]
29. Chao, H.; Houston, M.E.; Hodges, R.S.; Kay, C.M.; Sykes, B.D.; Loewen, M.C.; Davies, P.L.; Sönnichsen, F.D.; et al. A diminished role for hydrogen bonds in antifreeze protein binding to ice. *Biochemistry* **1997**, *36*, 14652–14660. [[CrossRef](#)]
30. Haymet, A.D.; Ward, L.G.; Harding, M.M.; Knight, C.A. Valine substituted winter flounder ‘antifreeze’ preservation of ice growth hysteresis. *FEBS Lett.* **1998**, *430*, 301–306. [[CrossRef](#)]
31. Zhang, W.; Laursen, R.A. Structure-function relationships in a type I antifreeze polypeptide. The role of threonine methyl and hydroxyl groups in antifreeze activity. *J. Biol. Chem.* **1998**, *273*, 34806–34812. [[CrossRef](#)] [[PubMed](#)]
32. Haymet, A.D.; Ward, L.G.; Harding, M.M. Hydrophobic analogues of the winter flounder ‘antifreeze’ protein. *FEBS Lett.* **2001**, *491*, 285–288. [[CrossRef](#)]
33. Loewen, M.C.; Chao, H.; Houston, M.E.; Baardsnes, J.; Hodges, R.S.; Kay, C.M.; Sykes, B.D.; Sönnichsen, F.D.; Davies, P.L. Alternative roles for putative ice-binding residues in type I antifreeze protein. *Biochemistry* **1999**, *38*, 4743–4749. [[CrossRef](#)] [[PubMed](#)]
34. Flores, A.; Quon, J.C.; Perez, A.F.; Ba, Y. Mechanisms of Antifreeze Proteins Investigated via the Site-Directed Spin Labeling Technique. *Eur. Biophys. J.* **2018**, *47*, 611–630. [[CrossRef](#)] [[PubMed](#)]
35. Raymond, J.A. Glycerol Is a Colligative Antifreeze in Some Northern Fishes. *J. Exp. Zool.* **1992**, *262*, 347–352. [[CrossRef](#)]
36. Rubinsky, B.; Arav, A.; Hong, J.-S.; Lee, C.Y. Freezing of Mammalian Livers with Glycerol and Antifreeze Proteins. *Biochem. Biophys. Res. Commun.* **1994**, *200*, 732–741. [[CrossRef](#)]
37. Guiberta, E.E.; Petrenkob, A.Y.; Balabana, C.L.; Somovb, A.Y.; Rodriguez, J.V.; Fullerc, B.J. Organ Preservation: Current Concepts and New Strategies for the Next Decade. *Transfus. Med. Hemotherapy* **2011**, *38*, 125–142. [[CrossRef](#)]
38. Bhattacharya, S.; Prajapati, B.G. A Review on Cryoprotectant and its Modern Implication in Cryonics. *Asian J. Pharm.* **2016**, *10*, 154–159.
39. Wood, D.L. Antifreeze Compositions. U.S. Patent 4,455,248, 19 June 1984.
40. *Toxicological Profile for Propylene Glycol*; Agency for Toxic Substances and Disease Registry (ATSDR): Atlanta, GA, USA, 1997; pp. 90–94.
41. Hubbell, W.L.; Gross, A.; Langen, R.; Lietzow, M.A. Recent advances in site-directed spin labeling of proteins. *Curr. Opin. Struct. Biol.* **1998**, *8*, 649–656. [[CrossRef](#)]
42. Hubbell, W.L.; Altenbach, C. Site-directed spin labeling of membrane proteins. *Methods Physiol. Ser.* **1994**, *1*, 224–248.
43. Hubbell, W.L.; Altenbach, C.; Langen, R.; Oh, K.J.; Cascio, D.; Columbus, L.; Hideg, K.; Cai, K.; Klein-Seetharaman, J.; Kim, J.; et al. *Nitroxide’s View of Membrane Protein Structure and Conformational Switching*; American Chemical Society: Washington, NY, USA, 2000; p. PHYS-454.

44. Galiano, L.; Blackburn, M.E.; Veloro, A.M.; Bonora, M.; Fanucci, G.E. Solute Effects on Spin Labels at an Aqueous-Exposed Site in the Flap Region of HIV-1 Protease. *J. Phys. Chem. B.* **2009**, *113*, 1673–1680. [[CrossRef](#)] [[PubMed](#)]
45. Steinhoff, H.-J.; Suess, B. Molecular mechanisms of gene regulation studied by site-directed spin labeling. *Methods* **2003**, *29*, 188–195. [[CrossRef](#)]
46. Longhi, S.; Belle, V.; Fournel, A.; Guigliarelli, B.; Carriére, F. Probing structural transitions in both structured and disordered proteins using site-directed spin-labeling EPR spectroscopy. *J. Pept. Sci.* **2011**, *17*, 315–328. [[CrossRef](#)] [[PubMed](#)]
47. Štrancar, J.; Kavalenka, A.; Urbančič, I.; Ljubetič, A.; Hemminga, M.A. SDSL-ESR-based protein structure characterization. *Eur. Biophys. J.* **2010**, *39*, 499–511. [[CrossRef](#)] [[PubMed](#)]
48. Klare, J.P.; Steinhoff, H.-J. Spin labeling EPR. *Photosynth Res.* **2009**, *102*, 377–390. [[CrossRef](#)] [[PubMed](#)]
49. Hideg, K.; Hankovszky, O.H. Chemistry of Spin-labeled Amino Acids and Peptides. In *Spin Labeling Theory and Applications*; Berliner, L.J., Reuben, J., Eds.; Plenum Press: New York, NY, USA; London, UK, 1989; pp. 427–487.
50. Chao, H.; Sønnichsen, F.D.; DeLuca, C.I.; Sykes, B.D.; Davies, P.L. Structure-function relationship in the globular type III antifreeze protein: identification of a cluster of surface residues required for binding to ice. *Protein Sci.* **1994**, *3*, 1760–1769. [[CrossRef](#)]
51. DeLuca, C.I.; Chao, H.; Sonnichsen, F.D.; Sykes, B.D.; Davies, P.L. Effect of type III antifreeze protein dilution and mutation on the growth inhibition of ice. *Biophys. J.* **1996**, *71*, 2346–2355. [[CrossRef](#)]
52. Deluca, C.I.; Davies, P.L.; Ye, Q.; Jia, Z. The effects of steric mutations on the structure of type III antifreeze protein and its interaction with ice. *J. Mol. Biol.* **1998**, *275*, 515–525. [[CrossRef](#)]
53. Graether, S.P.; DeLuca, C.I.; Baardsnes, J.; Hill, G.A.; Davies, P.L.; Jia, Z. Quantitative and qualitative analysis of type III antifreeze protein structure and function. *J. Biol. Chem.* **1999**, *274*, 11842–11847. [[CrossRef](#)]
54. Altenbach, C. *Multi-Component EPR Fitting Version 742*, LabVIEW Software: Austin, TX, USA.
55. Takacs, I.M.; Mot, A.; Silaghi-Dumitrescu, R.; Damian, G. Hemoglobin Side Chains by Spin Labeled EPR Spectroscopy. *Studia UBB Phys.* **2013**, *58*, 49–58.
56. Couto, S.G.; Nonato, M.C.; Costa-Filho, A.J. Site directed spin labeling studies of Escherichia coli dihydroorotate dehydrogenase N-terminal extension. *Biochem. Biophys. Res. Commun.* **2011**, *414*, 487–492. [[CrossRef](#)] [[PubMed](#)]
57. Mao, Y.; Ba, Y. Ice-Surface Adsorption Enhanced Colligative Effect of Antifreeze Proteins in Ice Growth Inhibition. *J. Chem. Phys.* **2006**, *125*, 091102. [[CrossRef](#)] [[PubMed](#)]



© 2019 by the authors. Licensee MDPI, Basel, Switzerland. This article is an open access article distributed under the terms and conditions of the Creative Commons Attribution (CC BY) license (<http://creativecommons.org/licenses/by/4.0/>).

Article

Ice Crystal Coarsening in Ice Cream during Cooling: A Comparison of Theory and Experiment

Jingyi Mo ^{1,2,*}, Robert D. Groot ³, Graham McCartney ^{1,2}, Enyu Guo ⁴, Julian Bent ⁵, Gerard van Dalen ³, Peter Schuetz ⁵, Peter Rockett ¹ and Peter D. Lee ^{1,2,*}

¹ Department of Mechanical Engineering, University College London, London WC1E 7JE, UK; Graham.McCartney@nottingham.ac.uk (G.M.); peterrockett33@gmail.com (P.R.)

² Research Complex at Harwell, RAL, Didcot OX11 0FA, UK

³ Unilever Research & Development, Olivier van Noortlaan, 3133AT Vlaardingen, The Netherlands; Rob.Groot@unilever.com (R.D.G.); Gerard-van.Dalen@unilever.com (G.v.D.)

⁴ School of Materials Science and Engineering, Dalian University of Technology, Dalian 116024, China; eyguo@dlut.edu.cn

⁵ Unilever R&D, Colworth MK44 1LQ, UK; Julian.Bent@unilever.com (J.B.); Peter.Schuetz@unilever.com (P.S.)

* Correspondence: j.mo@ucl.ac.uk (J.M.); peter.lee@ucl.ac.uk (P.D.L.); Tel.: +44-(0)-1235-567789 (P.D.L.)

Received: 19 April 2019; Accepted: 21 June 2019; Published: 25 June 2019

Abstract: Ice cream is a complex multi-phase structure and its perceived quality is closely related to the small size of ice crystals in the product. Understanding the quantitative coarsening behaviour of ice crystals will help manufacturers optimise ice cream formulations and processing. Using synchrotron X-ray tomography, we measured the time-dependent coarsening (Ostwald ripening) of ice crystals in ice cream during cooling at 0.05 °C/min. The results show ice crystal coarsening is highly temperature dependent, being rapid from ca. –6 to –12 °C but significantly slower at lower temperatures. We developed a numerical model, based on established coarsening theory, to calculate the relationship between crystal diameter, cooling rate and the weight fraction of sucrose in solution. The ice crystal diameters predicted by the model are found to agree well with the measured values if matrix diffusion is assumed to be slowed by a factor of 1.2 due to the presence of stabilizers or high molecular weight sugars in the ice cream formulation.

Keywords: ice cream; microstructure; ice crystals; tomography; modelling; coarsening kinetics

1. Introduction

Ice cream is a popular dairy product whose microstructure is one of the critical factors that determines its sensorial perception. Structurally, ice cream is a complex colloid system that is composed of ice crystals, air bubbles and partially coalesced fat droplets, all of which are surrounded by an unfrozen matrix containing sucrose, proteins and stabilizer [1–3]. However, an assembly of fine crystals is thermodynamically far from equilibrium and crystals coarsen over time [4–6]. The control of the crystal size is widely recognized as a critical factor in the development of a smooth and creamy texture desired by consumers; large ice crystals will be perceived as being grainy and coarse [1].

Therefore, it is of great interest for the food scientist to develop a predictive description of physical mechanisms that govern the kinetics of the coarsening in order to inhibit a deterioration in the quality of ice cream. The characteristic sizes of this multi-phase material vary considerably, e.g., air bubbles 20–150 µm, ice crystals 10–75 µm, and fat particles 0.4–4 µm as well as fat particle aggregates ~10 µm [1]. A glass transition is observed around –30 °C at which the microstructure is relatively stable. However, experimental studies on the growth of ice crystals in ice cream have shown that phase coarsening is very significant in the temperature range –15 to –5 °C [7]. The manufacture of ice cream commonly involves two stages: Freezing and hardening. During initial freezing, occurring

in a scraped-surface freezer (SSF) at around $-5\text{ }^{\circ}\text{C}$, about half of the water in a homogenised ice cream mixture is frozen rapidly, and air is also incorporated into the product. After exiting the SSF, the bulk of the mixture is filled into containers and placed in an air blast freezer for hardening until the temperature in the core of the mixture reaches $\sim -18\text{ }^{\circ}\text{C}$ over a period of time, usually around 2 hours with a cooling rate $\sim 0.1\text{ }^{\circ}\text{C}/\text{min}$. The final product is stored at temperatures ranging from -23 to $-18\text{ }^{\circ}\text{C}$ before distribution to the consumer. Thus, the factors affecting ice crystal size variation during these stages need to be well understood.

The microstructural coarsening observed in many systems (including ice crystals in sucrose solutions and in ice cream) comprising a dispersion of fine particles in a matrix phase, is an effect which is known as Ostwald ripening [6,8–11]. This refers to the increase in the size-scale of the dispersed phase with time to minimize the total surface energy coming from curvature effects [12]. The process occurs by diffusion through the matrix. The diffusion is driven by the Gibbs Thomson effect i.e., the solute concentration in the matrix in equilibrium with larger particles is different from that with the smaller particles such that the larger particles grow in size at the expense of the smaller ones, which shrink.

The earliest work of Lifshitz-Slyozov and Wagner (LSW) on Ostwald ripening dates to 1961 and is referred to as the LSW theory [12,13]. It is only strictly valid for a precipitate (particle) volume fraction approaching zero and ignores the effect of volume fraction of the dispersed phase. In real systems e.g., ice crystal—sucrose solution, as is found in ice cream, a finite volume fraction (typically 20 to 30%) of ice crystals is present. Many attempts have been developed to improve upon the LSW theory by extending its applicability to a finite volume fraction. Marsh and Glicksman [14], for example, employed the concept of a statistical “field cell” and “transport field” to describe the diffusional interaction among each particle size class. Other approaches are reviewed in reference [15–22].

In a recent paper, van Westen and Groot [23] demonstrated that for a model system of polycrystalline ice within an aqueous solution of sugars the coarsening rates could be predicted on the basis of Ostwald ripening theory with relative deviations to experimental values not exceeding a factor of 2. However, this required that the theory accounts for a number of effects. First, that the solution is nonideal, nondilute and of different density from the crystals, secondly, the effect of ice-phase volume fraction on the diffusional flux between crystals is accurately described, and thirdly, all relevant material properties are carefully estimated. In a further paper the same authors [24] simulated the effect of thermal cycling on ice crystal coarsening in aqueous sucrose solutions and showed that their model correctly predicted an experimentally observed increase in coarsening rate for a thermally cycled sample compared to one that is coarsened isothermally. They identified that faster diffusivity at elevated temperatures is an important factor for enhanced ripening as observed in temperature cycling, which suggests that slow cooling from a high initial temperature may be important for the growth of large ice crystals.

However, it is a major challenge to validate models of the behaviour of ice crystals in ice cream due to the lack of methods which can visualise its three-dimensional (3D) microstructure. Pinzer et al. [25] used a laboratory X-ray microCT in a cold room to investigate the long term microstructural evolution of ice cream and quantified changes in air cell and ice crystal size during thermal cycles between -16 to $-5\text{ }^{\circ}\text{C}$ over a period of 24 hours. However, resolution of the structure was a limitation with this instrument. More recently Guo et al. [7,26] and Mo et al. [27] have reported time-resolved synchrotron computed tomography (sCT) studies of the microstructural evolution of ice cream. In the work of Mo et al. [27] in situ experimental observations clearly reveal the coarsening of ice crystals during continuous cooling experiments on ice cream in the range -5 to $-23\text{ }^{\circ}\text{C}$ but only a limited quantification of crystal dimensions was undertaken.

Therefore, the main aim of the present study on ice cream was to compare the predictions of a model for coarsening in a sample undergoing continuous cooling with ice crystal size measurements obtained from in situ sCT studies. In this paper we first extend our original isothermal Ostwald ripening model [23,24] to distinguish the effects of diffusivity and ice fraction from the effect of phase

ripening at a fixed cooling rate. Next, we simulate phase coarsening in microstructures reflecting the same volume fraction as used experimentally. Finally, we compare predictions based on simulation with the in situ experimental measurements of ice crystal dimensions.

2. Model Theory

Our previous papers concerning the Ostwald ripening of ice crystals in aqueous sucrose solution [23,24] have provided a detailed analysis of Ostwald ripening and have addressed both isothermal Ostwald ripening in aqueous solutions [23] and also the effect of temperature cycling on the Ostwald ripening of ice crystals in an aqueous solution of sugars [24]. In this section we aim to provide only a brief overview of the background theory which will be sufficient to understand the modelling results reported in the present paper.

The kinetic equation describing the growth or shrinkage rate of an individual particle of radius, a , is given by Equation (1) [20,21]:

$$\frac{da}{dt} = \frac{D}{a} \left(\Delta - \frac{2d_0}{a} \right) \quad (1)$$

where $\Delta = 1 - C_s/C_{s,eq}$ is the supersaturation far away from the particle surface (C_s is the concentration of solute in the matrix phase at the interface with the particle and $C_{s,eq}$ is the thermodynamic equilibrium solute concentration at that temperature). D is the Fick diffusion coefficient and d_0 is the (chemical) capillary length of the Gibbs Thomson equation [8] and t is time. The definition of d_0 is given in detail in Supplementary Materials.

Crystals will grow when they are larger than a critical radius $a^* = 2d_0/\Delta$ and shrink when they are smaller than a^* . An alternative formulation can be obtained in terms of mole fractions and Maxwell–Stefan diffusion [23].

2.1. Isothermal Coarsening

When the temperature is constant, the dispersed phase fraction quickly approaches its quasi-equilibrium value. The particle size distribution approaches a scaling function $f(a/\langle a \rangle, \phi)$ which depends on the relative crystal size $z = a/\langle a \rangle$, and on the particle volume fraction ϕ . Typical examples of a stationary crystal size distribution are shown in Figure 1. The black curve marked LSW shows the distribution from the Lifshitz–Slyozov–Wagner theory. This theory is only valid for vanishing ice volume fraction, however. The red curve is calculated from the Marsh–Glicksman (MG) theory [14] for an ice volume fraction ϕ of 0.6.

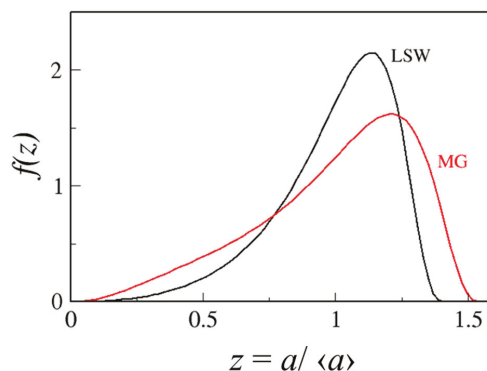


Figure 1. Stationary crystal size distribution for volume fraction $\phi = 0$ (LSW) and for $\phi = 0.6$ (MG).

At a fixed temperature, the mean particle radius, $\langle a \rangle$, grows at a rate that is proportional to $t^{1/n}$, where n depends on the growth mechanism. When growth is controlled by diffusion through the matrix, n takes the value 3,

$$\langle a \rangle^n = \langle a \rangle_0^n + Kt \quad (2)$$

where $\langle a \rangle_0$ is the mean radius at time $t = 0$, and K is the coarsening rate constant and Equation (2) describes how the mean radius increases over time at constant temperature.

The earliest work of Lifshitz-Slyozov and Wagner (LSW) on Ostwald ripening in which Equation (2) was derived is strictly valid in the limit of zero dispersed phase volume fraction. Many extensions of the LSW approach have been developed but all predict the temporal law given by Equation (2) but with a rate constant K that increases with volume fraction [15].

This coarsening rate constant K has two main contributions and can be written as [23]

$$K = \frac{8}{9} \xi(T) g(\phi) \quad (3)$$

The factor $8/9$ is the classical LSW result for vanishing volume fraction. The factor $\xi(T)$ depends on surface energy and diffusivity, the driving forces responsible for coarsening and $g(\phi)$ is a non-dimensional geometric factor that accounts for the diffusion distance. It depends on the mathematical form of the crystal size distribution and on the ice volume fraction, ϕ .

The dimensional factor $\xi(T)$ is given by a complicated expression containing the molar volumes of ice and water, the melting curve of the phase diagram (liquidus line), the surface energy between ice and water (temperature dependent), and the Maxwell-Stefan diffusion coefficient.

For the sucrose-water system a polynomial fit to the temperature-dependent contribution is given in Ref. [23], but this may not allow extrapolation to temperatures far below -14°C . Based on the raw data, a new Padé fit is made which is more reliable for extrapolations. This is represented by Equation (4):

$$\ln \xi(T) = \frac{b_0 + b_1 T + b_2 T^2}{1 + b_3 T + b_4 T^2} \quad (4)$$

with $b_0 = 7.874452 \mu\text{m}^3/\text{min}$, $b_1 = -2.84417 \mu\text{m}^3/\text{min/K}$, $b_2 = -0.38216 \mu\text{m}^3/\text{min/K}^2$, $b_3 = -0.78445 \mu\text{m}^3/\text{min/K}$ and $b_4 = 0.020165 \mu\text{m}^3/\text{min/K}^2$, where $\xi(T)$ is expressed in $\mu\text{m}^3/\text{min}$, and temperature in $^\circ\text{C}$. This fit was based on the data between $-14^\circ\text{C} < T < -1.5^\circ\text{C}$, where the raw data were most reliable, i.e., the equilibrium ice fraction was not based on extrapolation. Both fits are shown in Figure 2.

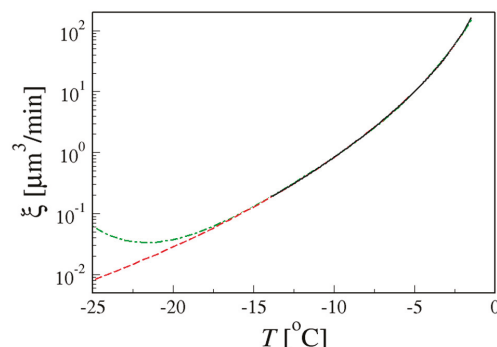


Figure 2. Dimensional factor $\xi(T)$ appearing in the coarsening rate (black curve). The green dash-dot curve is the polynomial fit by Van Westen and Groot [23] and the red dashed curve is the present Padé fit.

The geometric factor $g(\phi)$ has been the subject of several theories and simulation methods. Following the earlier work by Van Westen and Groot, a convenient fit to simulation data is given by their Equation (37) [23] which is Equation (5) below:

$$g(\phi) = 1 + 2.04 \frac{\phi^{3/7}}{1 - \phi} \quad (5)$$

2.2. Coarsening during Cooling

When a system is cooled the supersaturation in Equation (1) increases hence more crystals start to grow. This changes the size distribution and the rate of Ostwald ripening.

During continuous cooling the total variation of the mean cubed particle radius involves the sum of two terms as follows:

$$\begin{aligned} d\langle a^3 \rangle &= \left(\frac{\partial \langle a^3 \rangle}{\partial f} \right)_t df + \left(\frac{\partial \langle a^3 \rangle}{\partial t} \right)_f dt \\ &= \frac{\langle a^3 \rangle}{f} df + \frac{(\partial \langle a^3 \rangle / \partial t)_f}{(d\langle a \rangle^3 / \partial t)_f} Kdt \\ &= \frac{\langle a^3 \rangle}{f} df + h(\phi) Kdt \end{aligned} \quad (6)$$

where f is the ice crystal mass fraction.

This is an approximation, because we assume quasi-equilibrium conditions at each point in time. This is justified in the Supplementary Materials.

The first term describes the change of mean crystal volume under an infinitely fast ice fraction variation, for which the number of ice crystals is fixed. In that case we have $\langle a^3 \rangle \propto f$, hence $(\partial \langle a^3 \rangle / \partial f)_t = \langle a^3 \rangle / f$. The second term describes the change of mean crystal volume due to isothermal Ostwald ripening. It contains a factor $h(\phi) = (\partial \langle a^3 \rangle / \partial t)_f / (d\langle a \rangle^3 / \partial t)_f = \langle a^3 \rangle / \langle a \rangle^3$ to correct the growth law (Equation (2)) to calculate $d\langle a^3 \rangle$ rather than $d\langle a \rangle^3$. For an equilibrium distribution in isothermal conditions the ratio $\langle a^3 \rangle / \langle a \rangle^3$ is constant over time, because the distribution has scaling behaviour. Therefore, the ratio of the above partial time derivatives is equal to the ratio $\langle a^3 \rangle / \langle a \rangle^3$ itself.

The geometric function $h(\phi) = \langle a^3 \rangle / \langle a \rangle^3$ which appears in Equation (6) is needed to transform radius-averaged Ostwald ripening into volume-averaged ripening. Marsh and Glicksman gave tabulated data for the first three moments of the size distribution as function of the crystal volume fraction [14]. From these data we calculate a fit that is given by:

$$h(\phi) = 1 + \left(\frac{3}{5} \right)^4 + 0.1167 \frac{\phi^{0.32}}{1 - 0.38 \phi^{2.5}} \quad (7)$$

To find the mean cubed particle diameter, $2\langle a^3 \rangle^{1/3}$, (also known as $D_{3,0}$) as a function of time we employ a numerical integration scheme to solve Equation (6). We decrease the temperature by a small step δT (< 0) and calculate the corresponding time step from a chosen cooling rate $B = -dT/dt$. The calculation uses critically assessed thermophysical and phase diagram data that have been described previously [23,24].

3. Experimental Procedures and Data Analysis

To validate the model for Ostwald ripening of ice cream, a bespoke cold stage capable of precise thermal cycling combined with the in situ synchrotron tomographic imaging technique described in detail previously was employed to determine the structural changes undergone [7,26,27].

3.1. Sample Preparation and Thermal Cycling

Fresh ice cream (40% ice and 5% fat), prepared by Unilever R&D (Colworth, UK) was scooped out and left at room temperature to melt. Kapton tubes (specification: inner diameter 3 mm and wall thickness 67 μm , American Durafilm Co. Inc, Holliston, MA, USA) were filled with this liquid mixture with a syringe, followed by mounting them onto a cold stage specially designed for operation in the synchrotron beamline which is described in our previous papers [7,26,27].

The in situ experiments were performed in the following manner. The Kapton tube with the ice cream specimen was mounted onto the cold stage at -3°C (just below the melting point). Then its temperature was rapidly reduced down to -23°C with a fast ramp rate of $-5^\circ\text{C}/\text{min}$ and held at this temperature for 10 min. The specimen was subsequently heated to -6°C , at the same ramp rate as the cooling ramp rate, and maintained there for 10 min. A long-term slow cooling was then applied to study global parameters for phase coarsening, such as the particle size distribution. The system was subsequently cooled down from -6°C until a temperature of -23°C was reached with a slow cooling ramp rate of $-0.05^\circ\text{C}/\text{min}$. The overall thermal history for coarsening experiments is shown in Figure 3. Eight tomographic scans were performed at the temperatures indicated by the diamond symbols on Figure 3 to study the phase coarsening changes during cooling. Care was taken to ensure that the sub-volumes used for the measurements were free from bubbles. Therefore, the model assumption of a continuous unfrozen matrix phase was valid for the measured volumes.

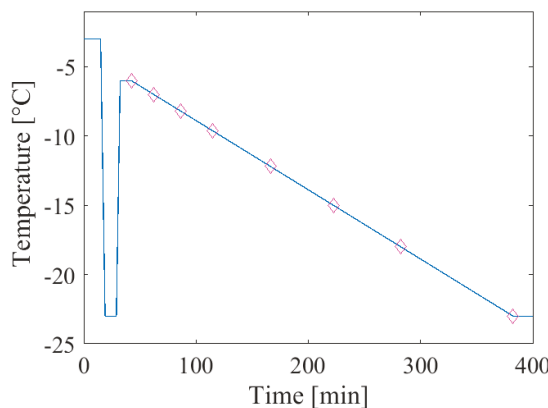


Figure 3. The thermal history of the ice cream mixture specimen during the in situ coarsening experiments. The temperature points where the tomographic scans were reconstructed are indicated as pink diamond markers.

3.2. Characterization by Synchrotron X-ray Computed Tomography (sCT)

A detailed description of the sCT approach has been reported previously [7,26,27] and is briefly summarised here. Combined coarsening experiments with in situ acquisition of tomographic scans were carried out at the high brilliance I13-2 beamline at Diamond Light Source (DLS, Harwell, UK) using a pink beam. The tomographic scans were recorded by a 2560×2160 pixel PCO Edge 5.5 CMOS camera combined with a single crystal CdWO₄ scintillator. The specimen-to-camera distance was optimized to ~ 35 mm with a final pixel-resolution of $0.81\text{ }\mu\text{m}$. During the in situ experiments, each tomographic run includes collecting 720 projections evenly spaced over a 180° rotation with the exposure time of 0.1 s. In this study, a total of eight tomographic scans were recorded at the following temperatures: -6.0 , -7.0 , -8.2 , -9.6 , -12.2 , -15.5 , -18.0 and -23°C ; these are indicated by the diamond symbols on Figure 3. These scans were then pre-processed and the tomographic slices for the respective temperatures were reconstructed.

3.3. Volume Data Reconstruction and Pre-Processing

The collected 2D projections, i.e. radiographs, were virtually stacked to form sinograms. Any apparent continuous lines from sinogram images were removed by interpolation in order to reduce ring artefacts which is a result from imperfections from the detector/camera. The sinograms were then used to mathematically reconstruct the volume slices using a filtered back projection (FBP) based algorithm. Because the ice cream samples were relatively low attenuating to the incident X-ray beam, the reconstructed volumes exhibited a relatively high level of background noise. In order to reduce noise, the 3D volumes were first median ($3 \times 3 \times 3$) filtered and then followed by a morphological operation-based method as described previously [27]. The data were then binarised using global thresholding. All the volumes were carefully checked visually, and any obvious segmentation imperfections were corrected manually using Avizo 9.4 (FEI Visualization Sciences Group, Mérignac, 33700, France).

3.4. 3D Based Quantification of Ice Crystal Dimensions

Owing to the interconnected–network structure of ice crystals, it is not appropriate to segment them into individual components as they appear as interconnected clusters. Thus, a 3D image-based quantification method was developed and employed to analyze the size of ice crystals in the ice cream samples. This method is similar to the techniques for 3D porous structure characterisation and quantification for biomedical and geological materials as described in detail previously [27–29]. Briefly, we employed a series of sampling spheres with varying diameter, and the size distribution in the ice crystal phase was obtained by measuring the cumulative volume of ice crystal that can be reached by different sampling spheres [27]. Using this methodology, a modal value of the crystal diameter was obtained for each of the four sub-volumes examined at each of the temperatures for which sCT scans were performed.

4. Results and Discussion

4.1. Model Calculations

4.1.1. Relative Importance of Diffusivity and Ice Fraction

To gain insight into the relative importance of the factors driving Ostwald ripening during cooling, the rate constant $h \cdot K$ was calculated for a range of sucrose solution concentrations and the results are shown in Figure 4. The term $h \cdot K$ is proportional to $g(\phi) \cdot h(\phi) \cdot \xi(T)$ where h is given by Equation (7), K is given by Equation (3) and the temperature dependent ice volume fraction, ϕ , is calculated as set out in Supplementary Materials.

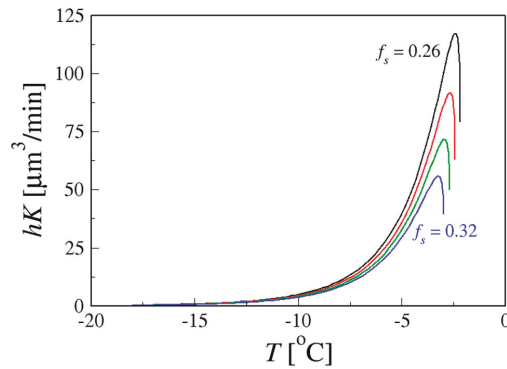


Figure 4. Coarsening rate constant for sucrose weight fractions of 26%, 28%, 30% and 32%. The curves end at the respective melting points.

The rate constant depends on temperature and on ice volume fraction, but it does not depend on the crystal size. At the melting point, the crystals are far apart because the ice volume fraction tends to zero. As temperature drops, the rate passes through a maximum and then drops again because diffusivity decreases towards lower temperatures. The position of the maximum shifts to lower temperatures and lower coarsening rates when sucrose concentration is increased. In fact, the amount of coarsening is quite sensitive to the sucrose fraction; if the weight fraction of sucrose (denoted as f_s) is increased from 26% to 32%, the maximum coarsening rate reduces by a factor 2.

The variation of the two factors namely the geometrical factor $g(\phi) \cdot h(\phi)$, and the dimensional temperature dependent factor $\xi(T)$ were also examined independently. It is found that the geometric factor varies only slightly over a wide sucrose composition range whereas the dimensional temperature dependent factor increases significantly at lower sucrose fractions, shown in Figure 5.

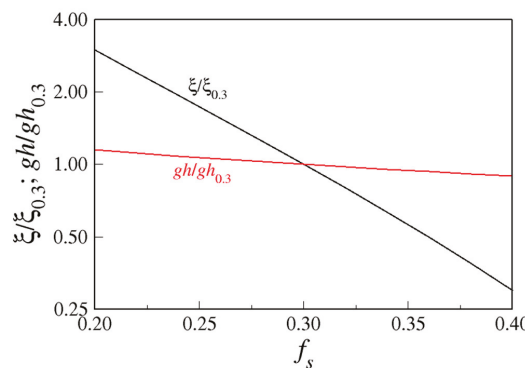


Figure 5. Contributions to the volumetric Ostwald ripening rate (at the temperature where $hK(T)$ has its maximum) plotted against sucrose mass fraction, f_s . Values are normalised relative to their value at $f_s = 0.3$.

Since the variation in $\xi(T)$ is dominated by the variation of diffusivity, we conclude that fast diffusivity at high temperatures is the most important factor responsible for strong crystal coarsening at slow cooling rates; geometric structure effects are secondary.

4.1.2. Coarsening at a Fixed Cooling Rate in Sucrose Solutions

Consider now a sample containing ice crystals that starts at temperature T_H and then drops to a final temperature T_F at a fixed rate $B = -dT/dt$. In that case, the crystal size is calculated by numerically integrating the following equation:

$$d\langle a^3 \rangle = \left(\frac{\langle a^3 \rangle}{f} \frac{df}{dT} - \frac{hK}{B} \right) dT \quad (8)$$

This follows directly from Equation (6) where the first term represents the increase in mean crystal volume due to cooling alone and the second term represents the contribution of Ostwald ripening during continuous cooling. See Supplementary Materials for details of the numerical procedure.

Whether the first or the second term in Equation (8) dominates the crystal size depends on the initial crystal size and on the cooling rate. Selected model calculations are shown in Figure 6 in which the volumetric mean diameter, $D_{3,0}$, is plotted versus temperature, T . The volumetric mean diameter is defined as $D_{3,0} = 2\langle a^3 \rangle^{1/3}$. The calculation was performed for ice crystals in a 30 wt% sucrose solution (melting point -2.7°C), cooled at a rate of $0.01^\circ\text{C}/\text{min}$ (full curves) and at $0.1^\circ\text{C}/\text{min}$ (dashed curves), starting at $5\text{ }\mu\text{m}$ (black) and $10\text{ }\mu\text{m}$ (green) initial radius. The initial temperature, T_H , is chosen as -3.0°C . The calculations show that fast or slow cooling may change the crystal diameter by a factor ~ 2 for the same composition, hence the number of crystals may change by an order of magnitude.

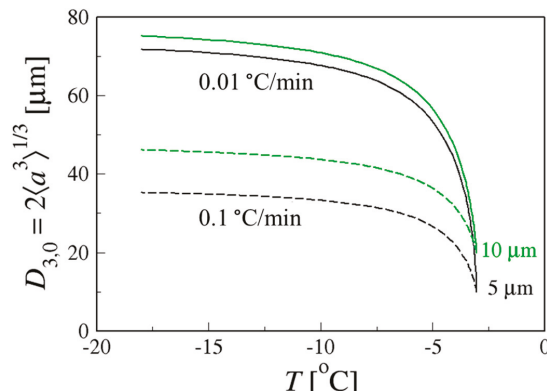


Figure 6. Volumetric mean diameter $D_{3,0}$ calculated for ice crystals in 30 wt% sucrose solution, cooled at a rate of $0.01^\circ\text{C}/\text{min}$ (full curves) and for $0.1^\circ\text{C}/\text{min}$ (dashed curves), starting at 5 (black) and 10 (green) μm radius.

4.1.3. Influence of Additives in Ice Cream Formulations

In full ice cream formulations, polymers are added that give enhanced storage stability. We suggest that the reason for this enhanced storage stability is that the time scale of Ostwald ripening is governed by the slowest mass transport process, which in the case of a polymer network in a sucrose solution will be the collective motion of the polymer. The sucrose solution is then acting as a viscous background medium through which the polymer moves. The rate by which the polymer network diffuses depends on elasticity modulus of the network, and the viscous flow through the network pores [30,31]. The collective diffusion coefficient of a polymer network is then inversely proportional to its friction factor, which in turn depends on the pore size of the network, and hence on the polymer concentration. Following the theory of Barrière and Leibler [32], it could be suggested that the rate of Ostwald ripening might be related to $f_p^{-3/2}$, where f_p is the polymer mass fraction in the formulation. For example,

λ -carrageenan (which is a common additive to ice cream) behaves as a loosely entangled polymer network [33], and could possibly reduce the ripening rate.

4.2. Experimental Observations and Comparison with Numerical Model

4.2.1. Morphological Evolution of Ice Crystals and Quantification of Dimensions

Figure 7 shows the 3D rendering of ice crystals from representative regions of the same size and the colour rendering represents the local thickness of each particle. The 3D evolution during the slow cooling cycle imposed in the sCT experiment with a cooling rate of $0.05\text{ }^{\circ}\text{C}/\text{min}$ is clearly observable. The ice crystals are very fine initially. During the initial stages of cooling from -6 to $-8.2\text{ }^{\circ}\text{C}$ there is significant microstructural evolution with clear coarsening, Figure 7a–c, as well as an increase in ice volume fraction due to the decreasing temperature.

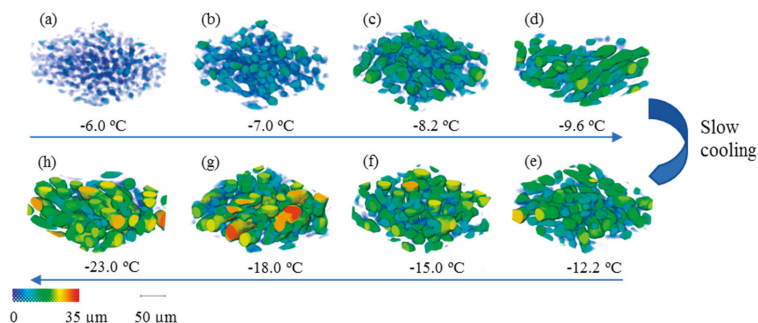


Figure 7. 3D visualisation of ice crystal morphological evolution during the slow cooling experiment: (a) $-6\text{ }^{\circ}\text{C}$, (b) $-7.0\text{ }^{\circ}\text{C}$, (c) $-8.2\text{ }^{\circ}\text{C}$, (d) $-9.6\text{ }^{\circ}\text{C}$, (e) $-12.2\text{ }^{\circ}\text{C}$, (f) $15\text{ }^{\circ}\text{C}$, (g) $-18.0\text{ }^{\circ}\text{C}$ and (h) $-23.0\text{ }^{\circ}\text{C}$. Ice crystals are colour-rendered using local thickness. Scale bar is $50\text{ }\mu\text{m}$.

Averaged modal values of ice phase dimensions were calculated by the 3D accessible volume method described in Section 3.4. The averaged modal values were computed from four sub-volumes which were randomly extracted from the global reconstructed volume. As expected from the 3D visualisations, at the beginning of the slow cooling regime, the ice crystals were very fine with a modal size of $7.8\text{ }\mu\text{m}$. During the slow cooling regime with a ramp rate of $0.05\text{ }^{\circ}\text{C}/\text{min}$, the modal size first increased significantly from $7.8\text{ }\mu\text{m}$ at $-6\text{ }^{\circ}\text{C}$ and to $21.8\text{ }\mu\text{m}$ at $-15.0\text{ }^{\circ}\text{C}$. Thereafter, the trend of increasing crystal size continued but at a much lower coarsening rate. This is presumably due to the slower diffusivity at lower temperature (as predicted by the model), resulting in a reduced rate of ice crystal coarsening.

4.2.2. Comparison between Measured and Calculated Ice Crystal Dimensions

In Figure 8, which are the plots of ice crystal diameter versus temperature, our measured modal dimensions from the sCT in situ experiment are compared to the mean crystal diameters calculated by the numerical model for a cooling rate of $0.05\text{ }^{\circ}\text{C}/\text{min}$ from $-6\text{ }^{\circ}\text{C}$ to $-23\text{ }^{\circ}\text{C}$. The detailed data used for this calculation are given in the Supplementary Materials. There is evidently a difference between the calculated and measured crystal dimensions during continuous cooling. In order to achieve a fit of the model to the experimental data shown in Figure 8 ($R^2 = 0.97$) the diffusivity used in the calculations had to be decreased by an overall factor of 1.2 compared to that for a pure sucrose solution containing the same wt% of sucrose (solid yellow line). This offset can be explained by a reduction in ripening rate due to the addition of hydrocolloid viscosifiers in the ice cream mix studied, in line with the behaviour proposed by Barrière and Leibler [32]. This observed reduction in rate lies well within the reduction in rates of crystal ripening for additions of λ -carrageenan to sucrose solutions which

have been observed in a separate study which will be the subject of a future paper. This observed reduction in rate lies well within the reduction in rates of crystal ripening for additions of l-carrageenan to sucrose solutions which have been observed in a separate study which will be the subject of a future paper. The diffusivity reduction factor is expected to be larger at higher ice fractions because the polymer network gets more concentrated in the matrix phase as the temperature falls. This effect has been neglected here. Note further, that the model calculates $D_{3,0}$ whereas in the experimental work the 3D accessible volume method was used to calculate modal values of crystal dimensions. Given the differences in measured and calculated dimensional features, the most notable finding is that the model correctly predicts the trend in ice crystal coarsening as the temperature decreases during continuous cooling. In conclusion, the presence of stabilisers or high molecular weight sugars, which are empirically added to ice cream, possibly improve product quality through their effect on reducing the coarsening of ice crystals especially at higher temperatures.

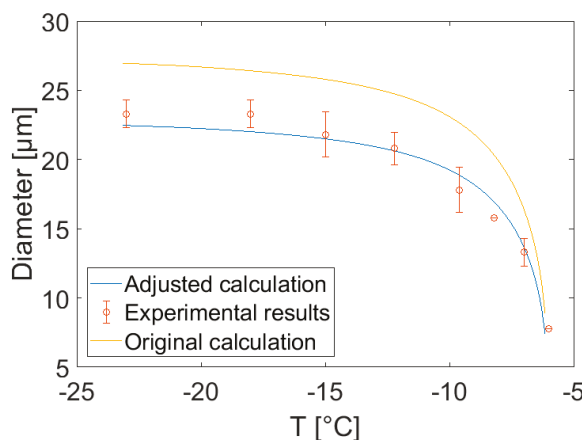


Figure 8. The diameter of ice crystals (modal values obtained from the 3D accessible volume method) measured from in situ sCT data (orange circles), compared with the diameter predicted by the present numerical model (solid blue line, the adjusted calculation; solid yellow line, the original calculation). Model diameter is calculated as $D_{3,0}$. For the calculations, we used the water and sucrose fractions $f_w = 0.55$ and $f_s = 0.29$ respectively. Error bars correspond to the range of the modal values.

5. Conclusions

The microstructural evolution of ice crystals in a commercial ice cream during continuous slow cooling was visualised and quantified with synchrotron X-ray tomography. Ice crystals present at a relatively high temperature of $-6\text{ }^{\circ}\text{C}$ coarsen by the well-known Ostwald ripening mechanism: Small crystals, or areas of high curvature, dissolve and large crystals grow. This process is strongly temperature-dependent, and to a lesser extent dependent on the geometry of the ice suspension structure. To model this process during continuous cooling, equilibrium theory of Ostwald ripening of dense suspensions of spherical crystals is applied. Our results reveal the following:

- (1) As expected, the 4D measurements (3D plus time) from synchrotron X-ray tomography show that coarsening of ice crystals occurs during cooling at $0.05\text{ }^{\circ}\text{C}/\text{min}$. The coarsening rate is rapid at high temperature (-6 to $-15\text{ }^{\circ}\text{C}$) but slows down significantly as the temperature falls further. Qualitatively, the number density of crystals also decreases during the cooling.
- (2) The numerical model to calculate Ostwald ripening of ice crystals in a sucrose solution (with a finite volume fraction) cooled at a steady rate to $-18\text{ }^{\circ}\text{C}$ predicts that fast ($0.1\text{ }^{\circ}\text{C}/\text{min}$) or slow cooling ($0.01\text{ }^{\circ}\text{C}/\text{min}$) will lead to significantly different crystal sizes. The volumetric mean diameter, $D_{3,0}$, differs by a factor of ~ 2 for the same sucrose mass fraction and starting crystal size.

- (3) The diameters of ice crystals in an ice cream formulation, measured by in situ sCT experiments, show good agreement with the model calculations if the diffusivity used in the calculations is reduced by a factor of 1.2 compared to that for a pure sucrose solution. Since the Ostwald ripening theory compares well with the experimental data for sucrose solutions [30,31] we conjecture that stabilisers and high molecular weight sugars in ice cream retard diffusion and hence slow down Ostwald ripening. More experiments are needed to confirm this conjecture.

In summary, the results demonstrate the powerful insights into material behaviour that can be achieved by combining 4D synchrotron X-ray tomography with physically based numerical modelling. They clearly reveal the critical temperature range for controlling the coarsening behaviour of ice particles in ice cream that is crucial to maintaining product quality and good sensory perception.

Supplementary Materials: Supplementary information is available online at <http://www.mdpi.com/2073-4352/9/6/321/s1>.

Author Contributions: Conception and design of the study: P.D.L., J.B., E.G., J.M., G.v.D., P.S. Design of equipment: P.R., E.G., J.M., P.D.L. Acquisition of data: E.G., J.M., G.v.D., P.S. Model development: R.D.G. Interpretation of data, revising the manuscript and final approval, and agreement to be accountable for all aspects of the work: all authors. Drafting the manuscript: J.M., R.D.G., G.M., P.S., P.D.L.

Funding: This research was funded by Unilever R&D (Colworth, U.K.), financially supported in part by the EPSRC (EP/I02249X/1, EP/J010456/1 and EP/M009688/1).

Acknowledgments: The authors acknowledge the use of the facility access in Diamond Light Source (MT12195, MT1216 and MT17609) and Research Complex at Harwell. The authors also thank I13 staff of Diamond Light Source (especially Silvia Cipiccia) and group members for technical support, including David Eastwood, Sam Clark, Yunhui Chen, Sebastian Marussi, and Lorna Sinclair.

Conflicts of Interest: The authors declare no conflict of interest.

List of Symbols

a	Particle radius
a^*	Critical particle radius
$\langle a \rangle$	Mean particle radius
$\langle a \rangle_0$	Mean particle radius at time $t = 0$
$\langle a^3 \rangle$	Mean value of the cube of the particle radius
b_i	Fitting constant in the equation for $\xi(T)$
B	Cooling rate
C_s	Concentration of solute in the matrix phase at the interface
$C_{s,eq}$	Thermodynamic equilibrium concentration of solute in the matrix phase
D	Fick diffusion coefficient
$D_{3,0}$	Mean cubed particle diameter = $2\langle a^3 \rangle^{1/3}$
d_0	Capillary length of the Gibbs Thomson equation
f	Ice phase mass fraction
f_p	Polymer mass fraction
f_s	Sucrose mass fraction
$g(\phi)$	Non-dimensional geometric factor accounting for diffusion distance
$h(\phi)$	Non-dimensional geometric factor relating radius and volume coarsening
K	Rate constant for isothermal coarsening
T	Temperature, °C
T_H	Initial temperature, °C
T_F	Final temperature, °C
t	Time
Δ	Supersaturation far away from the particle surface
ϕ	Particle or ice phase volume fraction
$\xi(T)$	Dimensional factor

References

- Clarke, C. *The Science of Ice Cream*; Royal Society of Chemistry: London, UK, 2015.
- Goff, H.D.; Hartel, R.W. *Ice Cream*; Springer Science & Business Media: Berlin, Germany, 2013.

3. Goff, H.D. Colloidal aspects of ice cream—A review. *Int. Dairy J.* **1997**, *7*, 363–373. [[CrossRef](#)]
4. Hartel, R.W. Mechanisms and kinetics of recrystallization in ice cream. In *The Properties of Water in Foods ISOPOW 6*; Springer: Boston, MA, USA, 1998; pp. 287–319.
5. Hagiwara, T.; Hartel, R.W.; Matsukawa, S. Relationship between recrystallization rate of ice crystals in sugar solutions and water mobility in freeze-concentrated matrix. *Food Biophys.* **2006**, *1*, 74–82. [[CrossRef](#)]
6. Cook, K.L.K.; Hartel, R.W. Mechanisms of ice crystallization in ice cream production. *Compr. Rev. Food Sci. F.* **2010**, *9*, 213–222. [[CrossRef](#)]
7. Guo, E.; Zeng, G.; Kazantsev, D.; Rocketta, P.; Bentc, J.; Kirklandc, M.; Van Dalenc, G.; Eastwoodab, D.S.; StJohn, D.; Lee, P.D. Synchrotron X-ray tomographic quantification of microstructural evolution in ice cream—a multi-phase soft solid. *Rsc Adv.* **2017**, *7*, 15561–15573. [[CrossRef](#)]
8. Ratke, L.; Voorhees, P.W. *Growth and Coarsening: Ostwald Ripening in Material Processing*; Springer Science & Business Media: Berlin, Germany, 2013.
9. Harper, E.K.; Shoemaker, C.F. Effect of locust bean gum and selected sweetening agents on ice recrystallization rates. *J. Food Sci.* **1983**, *48*, 1801–1803. [[CrossRef](#)]
10. Donhowe, D.P.; Hartel, R.W. Recrystallization of ice in ice cream during controlled accelerated storage. *Int. Dairy J.* **1996**, *6*, 1191–1208. [[CrossRef](#)]
11. Donhowe, D.P.; Hartel, R.W. Recrystallization of ice during bulk storage of ice cream. *Int. Dairy J.* **1996**, *6*, 1209–1221. [[CrossRef](#)]
12. Lifshitz, I.M.; Slyozov, V.V. The kinetics of precipitation from supersaturated solid solutions. *J. Phys. Chem. Solids* **1961**, *19*, 35–50. [[CrossRef](#)]
13. Wagner, C. Theorie der alterung von niederschlägen durch umlösen (Ostwald-reifung). *Zeitschrift für Elektrochemie, Berichte der Bunsengesellschaft für physikalische Chemie* **1961**, *65*, 581–591.
14. Marsh, S.P.; Glicksman, M.E. Kinetics of phase coarsening in dense systems. *Acta Mater.* **1996**, *44*, 3761–3771. [[CrossRef](#)]
15. Baldan, A. Review progress in Ostwald ripening theories and their applications to nickel-base superalloys Part I: Ostwald ripening theories. *J. Mater. Sci.* **2002**, *37*, 2171–2202. [[CrossRef](#)]
16. Ardell, A. The effect of volume fraction on particle coarsening: Theoretical considerations. *Acta Metall.* **1972**, *20*, 61–71. [[CrossRef](#)]
17. Brailsford, A.; Wynblatt, P. The dependence of Ostwald ripening kinetics on particle volume fraction. *Acta Metall.* **1979**, *27*, 489–497. [[CrossRef](#)]
18. Davies, C.; Nash, P.; Stevens, R.N. The effect of volume fraction of precipitate on Ostwald ripening. *Acta Metall.* **1980**, *28*, 179–189. [[CrossRef](#)]
19. Marqusee, J.; Ross, J. Theory of Ostwald ripening: Competitive growth and its dependence on volume fraction. *J. Chem. Phys.* **1984**, *80*, 536–543. [[CrossRef](#)]
20. Tsumuraya, K.; Miyata, Y. Coarsening models incorporating both diffusion geometry and volume fraction of particles. *Acta Metall.* **1983**, *31*, 437–452. [[CrossRef](#)]
21. Wang, K.; Wang, G.Q. Phase coarsening in multicomponent systems. *Phys. Rev. E* **2017**, *95*, 022609. [[CrossRef](#)]
22. Yan, H.; Wang, K.; Jones, J.E. Large-scale three-dimensional phase-field simulations for phase coarsening at ultrahigh volume fraction on high-performance architectures. *Model. Simul. Mater. Sci. Eng.* **2016**, *24*, 055016. [[CrossRef](#)]
23. Van Westen, T.; Groot, R.D. Predicting the Kinetics of Ice Recrystallization in Aqueous Sugar Solutions. *Cryst. Growth Des.* **2018**, *18*, 2405–2416. [[CrossRef](#)]
24. Van Westen, T.; Groot, R.D. Effect of Temperature Cycling on Ostwald Ripening. *Cryst. Growth Des.* **2018**, *18*, 4952–4962. [[CrossRef](#)]
25. Pinzer, B.R.; Medebach, A.; Limbach, H.J.; Dubois, C.; Stampanoni, M.; Schneebeli, M. 3D-characterization of three-phase systems using X-ray tomography: Tracking the microstructural evolution in ice cream. *Soft Matter* **2012**, *8*, 4584–4594. [[CrossRef](#)]
26. Guo, E.; Kazantsev, D.; Mo, J.; Bent, J.; Van Dalen, G.; Schuetz, P.; Rockett, P.; StJohn, D.; Lee, P.D. Revealing the microstructural stability of a three-phase soft solid (ice cream) by 4D synchrotron X-ray tomography. *J. Food Eng.* **2018**, *237*, 204–214. [[CrossRef](#)]
27. Mo, J.; Guo, E.; McCartney, D.G.; Eastwood, D.S.; Bent, J.; Van Dalen, G.; Schuetz, P.; Rockett, P.; Lee, P.D. Time-Resolved Tomographic Quantification of the Microstructural Evolution of Ice Cream. *Materials* **2018**, *11*, 2031. [[CrossRef](#)]

28. Wu, Z.Y.; Hill, R.G.; Yue, S.; Nightingale, D.; Lee, P.D.; Jones, J.R. Melt-derived bioactive glass scaffolds produced by a gel-cast foaming technique. *Acta Biomater.* **2011**, *7*, 1807–1816. [[CrossRef](#)]
29. Yue, S. Non-Destructive quantification of tissue scaffolds and augmentation implants using X-ray microtomography. Ph.D. Theses, Imperial College London, London, UK, 2011.
30. Peters, A.; Canda, S. Kinetics of swelling of spherical and cylindrical gels. *Macromolecules* **1988**, *21*, 2278–2282. [[CrossRef](#)]
31. Li, Y.; Tanaka, T. Kinetics of swelling and shrinking of gels. *J. Chem. Phys.* **1990**, *92*, 1365–1371.
32. Barrière, B.; Leibler, L. Kinetics of solvent absorption and permeation through a highly swellable elastomeric network. *J. Polym. Sci. Pol. Phys.* **2003**, *41*, 166–182. [[CrossRef](#)]
33. Del Rio, A.R.; Ramírez-Gilly, M.; Tecante, A. Flow Properties of Lambda Carrageenan in Aqueous Systems. In *Biological Activities and Application of Marine Polysaccharides*; IntechOpen: London, UK, 2017.



© 2019 by the authors. Licensee MDPI, Basel, Switzerland. This article is an open access article distributed under the terms and conditions of the Creative Commons Attribution (CC BY) license (<http://creativecommons.org/licenses/by/4.0/>).

Article

Quasi-Liquid Layer on Ice and Its Effect on the Confined Freezing of Porous Materials

Qiang Zeng ¹ and Kefei Li ^{2,*}

¹ College of Civil Engineering and Architecture, Zhejiang University, Hangzhou 310058, China; cengq14@zju.edu.cn

² Department of Civil Engineering, Tsinghua University, Beijing 100084, China

* Correspondence: likefei@tsinghua.edu.cn; Tel.: +86-10-62781408

Received: 31 March 2019; Accepted: 6 May 2019; Published: 14 May 2019

Abstract: Freezing of the water confined in thin pores can be destructive to the porous frame, but the effect of the quasi-liquid layer (QLL) between the confined ice and the pore walls remains still far from being fully understood. In the present study, the physical origins of the intermediate phase of QLL were discussed by thermodynamic analyses. Different interactions on QLL bring different models to estimate its thickness, which generally decays with temperature decreasing. Four representative models of QLL thickness were selected to unveil its effect on the growing rates and extents of ice in a concrete. The engineering consequences of the confined freezing were then discussed in the aspects of effective pore pressures built from the confined ice growth and deformations framed by a poro-elastic model. Overall, thickening QLL depresses ice growing rates and contents and, consequentially, decreases pore pressures and material deformations during freezing. The QLL corrections also narrow the gaps between the predicted and measured freezing deformations. The findings of this study contribute to profound understandings of confined freezing that may bridge over physical principles and engineering observations.

Keywords: freezing; quasi-liquid layer; pressure; deformation

1. Introduction

Since the first postulation of a quasi-liquid layer (QLL) on ice over 160 years ago, the understandings of its structure and links to our daily life (e.g., skating on ice and anti-freezing agent to keep food fresh) have been increasingly advanced [1–5]. Generally, this QLL, depending on the environmental temperature and what media ice is exposed to, ranges from one to several water molecular layers [6–13]. Predicting the thickness of QLL always faces challenges especially when the phase transition from water to ice is beyond the bulk freezing. A pertinent example is the freezing of the water confined in thin pores, which can be influenced by many factors such as the geometry confinement that regulates the crystal anisotropy, the curvature effect that depresses the freezing temperature, and the actions of the pore walls on the pore fluid [1,3,11,14–17]. Indeed, in chemical, environmental, and civil engineering, the confined freezing is more frequently quoted because almost all materials (except pure metals and crystals) are, more or less, in porous structures, and the phase transition of the water confined in the pores may occur in certain conditions during freezing [3,18]. However, the understandings of the possible influences of QLL on the freezing process of the confined water and the engineering consequences remain far from being completed.

To date, great efforts have been made to accumulate the knowledge of confined freezing by advanced experiments and simulations [6–12,19,20]. An example of the corresponding achievements may be the continually-developed cryoporometry techniques that allow us to measure the pores at nano-scales with the corrections of QLL [19,21]. As a typical porous material, concrete (and other cement-based materials like cement paste and mortar) may perform at low temperature, and confined

freezing will occur in the material. However, the research on the role QLL plays and its effects on the mechanical consequences of concrete has been limitedly reported [20,22–24]. In the present study, attempts were made to address how and to what extent the QLL between ice and the pore wall affects the confined freezing of a porous concrete.

In what follows, physical bases for confined freezing are briefly reviewed to display the generalized links between QLL thickness and temperature. The QLL data were collected from comprehensive experiments and simulations. Four different models of QLL thickness were then selected to demonstrate the QLL effect on the ice rising rates and contents in a porous concrete sample. Those QLL data were then implanted into a poro-elastic model to unravel the influences of QLL on the pore pressures built by ice crystallization and, consequentially, the material deformations. The scope of this study strictly followed the classic physico-chemical regimes of water, ice, pore confinement, and their interactions, and some simplifications of the properties of those phases were necessitated. The results of this study shed light on the understandings of the engineering consequences of confined freezing occurring in porous materials.

2. Physical Bases for Confined Freezing

2.1. Freezing in Pores

Physically, to form ice crystals in either bulk or confined water, the free energy (or chemical potential) of the ice must be lower than (or at least equal to) that of the liquid water. Here, we assumed that ice crystals can spontaneously form in the pores once the ice-water equilibrium was reached, and the kinetic issues (e.g., ice nucleation and water supercooling [25]) are out of the scope of this study. Figure 1 illustrates a snapshot of a partially-freezing pore network at a subzero temperature. For simplification, only a coarse pore chamber with two thin pore entries (or throats) is demonstrated in the figure. As displayed in Figure 1, ice occupies the pore chamber with a unique QLL in the thickness of t between the ice and the pore wall. Due to the curvature effect of the pore, which can lower the free energy of the confined water, freezing takes place at a depressed temperature, which can be described by the Gibbs–Thompson (GT) equation [19],

$$T_0 - T_m = \frac{2\kappa T_0 \gamma_{cl}}{\Delta H_f} \quad (1)$$

where T_m (K) is the melting temperature in equilibrium; T_0 (K) is the bulk freezing temperature of water in the standard condition ($P = 1$ atm); κ (1/m) is the mean curvature of the pore; γ_{cl} (N/m) is the surface tension of ice exposed to liquid water; ΔH_f (J/m³) is the fusion enthalpy. The GT equation has been extensively applied to capture the shifts in freezing temperature of pore fluids confined in various porous materials [19,20,22].

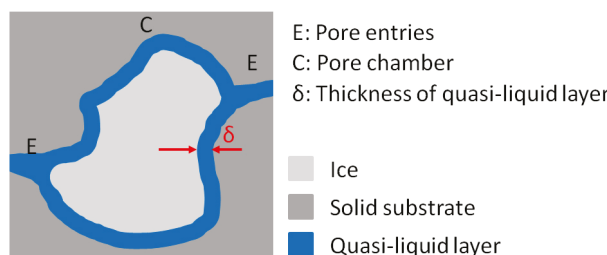


Figure 1. Cross-sectional view of a pore filled with an ice and connected with small entries. A quasi-liquid layer (QLL) with a thickness of t between the ice and the pore wall exists to achieve a physico-chemically-stable status of the confined freezing system.

Due to the complex pore networks of porous materials [26], even if the thickness of QLL is known, it remains difficult to estimate the ice volume due to the complex pore geometry and anisotropy. Here, we assumed that the partially-frozen pores are convex in principle, then the volume V and surface area A of the pores and the confined ice crystals that are separated by the QLLs can be estimated by [27],

$$V_c = V_p - A_p (t - \kappa t^2) \quad (2a)$$

$$A_c = A_p (1 - 2\kappa t) \quad (2b)$$

where the subscripts p and c denote the pores and ice crystals, respectively. Here, the mean pore curvature κ can be determined by the principle radii of curvature r_1 and r_2 through $\kappa = (A/2) \int (1/r_1 + 1/r_2) dr$ [28]. Once the pore geometries in a porous material were identified, Equation (2) helped build an integrated equation to estimate the ice content in the porous medium during freezing.

2.2. QLL on Ice

A disordered phase will exist on a solid ice surface in equilibrium if it can lower the free energy of the system; that is, if by its existence, an intermediate layer of thickness, t , reduces the total excess free energy. Physically, in an ice-QLL-substrate system, the total free energy changes come from (1) the heat release by ice formation, (2) the formation of a new liquid-crystal surface, and (3) the energy disturbance by the sandwich-like ice-QLL-substrate structure [3,4,27].

The thickness of QLL between ice and substrate, t , is intrinsically related to its potential, $F(t)$, which depends on the acting forces between the solid-liquid and liquid-ice interfaces [4,14]. The thermodynamic bases for the relationships between F and t can be found in Appendix A. There are several regimes governing the acting forces on the intermediate QLL phase. One widely-adopted regime is that the forces decay exponentially with the distance between the ice and substrate surfaces [3,14,19], i.e., $F = 1 - \exp(-2t/\varepsilon)$, with ε being the characteristic decay length, which can be determined by experiments [6]. In this case, the QLL thickness can be expressed as,

$$t = \frac{-\varepsilon}{2} \ln \left[\frac{\varepsilon \Delta H_f (T_m - T)}{2T_0 \Delta \gamma} \right] \quad (3)$$

where $\Delta \gamma$ (N/m) is the surface energy differences when the supposed substrate-crystal (sc) interface is replaced by the liquid-crystal (lc) and liquid-substrate (ls) ones (that is, a QLL inserts between the ice and the pore wall shown in Figure 1) and can be expressed as $\Delta \gamma = \gamma_{sc} - (\gamma_{lc} + \gamma_{ls})$. Equation (3), indeed, conforms to the well-used approximating form, $t \propto \ln(T_m - T)$, for representing the $t - T$ relation [14,19,29].

However, there may exist complex physical actions on the QLL phase, e.g., the long- and short-range electrostatic, nonretarded, and retarded van der Waals interactions [3]. Depending on the sorts of interactions, Wettlaufer et al. [30] suggested a generalized power decaying equation of the interfacial potential $F(t)$, $F = t^n / (t^n + \sigma^n)$, with σ being a typical interatomic distance. In general, σ is far lower than t ($\sigma \ll t$), and the potential decaying equation can be simplified to $F \approx 1 - (\sigma/t)^n$. In the case of the power decaying function of the potential, the QLL thickness can be given by:

$$t = \left[\frac{\Delta H_f (T_m - T)}{n \Delta \gamma \sigma^n T_0} \right]^{-1/(1+n)} \quad (4)$$

If, for instance, the interfacial actions between two microscopic bodies in a limiting separation are dominated by the long-range electrostatic forces, whose long-range potential decays with the square of the distance ($n = 2$), $F = t^2 / (t^2 + \sigma^2) \approx 1 - \sigma^2 / t^2$, Equation (4) then reduces to,

$$t = \left[\frac{\Delta H_f (T_m - T)}{2 \Delta \gamma \sigma^2 T_0} \right]^{-1/3} \quad (5)$$

In fact, Equation (5) captures the well-used semi-empirical model for estimating the thickness of QLL on ice, $t \propto (T_m - T)^{-1/3}$ [31].

2.3. Discussion on QLL Data and Models

The continually-developed experimental and simulative techniques have greatly accumulated our knowledge of the molecular structures of QLL and its thickness. Figure 2 illustrates the QLL thickness data acquired from the literature [6–12,19,29,31–36]. When dealing with those data, we ranked the data by author and neglected the thickness differences in different crystal faces, despite that surface melting takes place anisotropically on ice crystal surfaces [1,11].

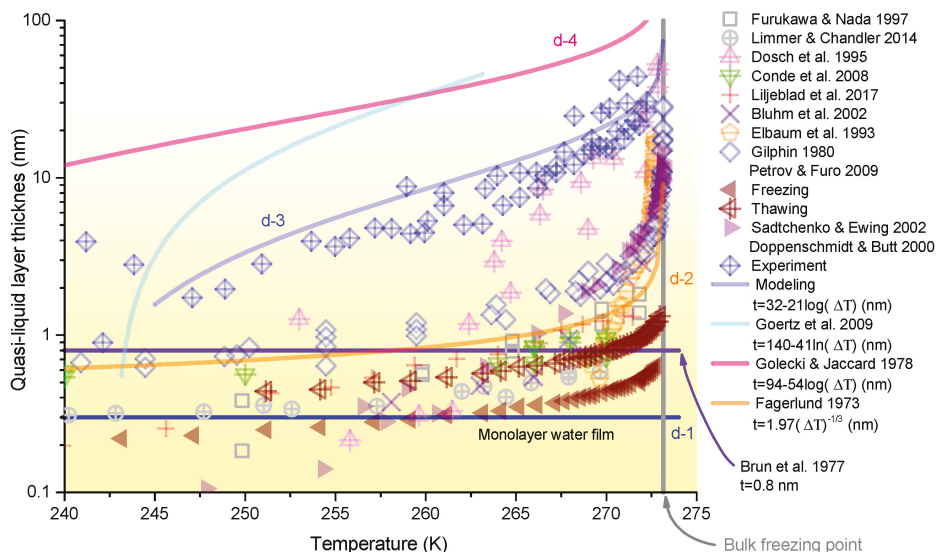


Figure 2. QLL thickness data from the literature [6–12,19,29,31–36]. The QLL thickness data reported in Furukawa and Nada (1997) [11], Conde et al. (2008) [10], and Limmer and Chandler (2014) [7] were obtained by molecular dynamic simulations; those in Elbaum et al. (1993) by interference microscopy; those in Dosch et al. (1995) [12] by glancing-angle X-ray scattering; those in Gilpin (1980) [36] by theoretical calculation; those in Doppenschmidt and Butt (2000) [6] by atomic force microscopy; those in Bluhm et al. (2002) [8] by photoelectron spectroscopy; those in Sadchenko and Ewing (2002) [34] by infrared spectroscopy; those in Petrov and Furo (2009) [19] by thermodynamic estimations; and those in Liljeblad et al. (2017) [9] by total internal reflection Raman, vibrational sum frequency, and NMR spectroscopies. The $t - T$ line reported in Goertz et al. (2009) [33] was regressed from the experimental data measured by interfacial force microscopy and that in Brun et al. (1973) [32] by differential scanning calorimetry. The $t - T$ curves of d-1, d-2, d-3, and d-4 are representatively selected for unraveling the influences of QLL on freezing of porous materials; see Table 1.

At first glance, from Figure 2, the QLL thickness varied by up to three orders of magnitude for a set temperature, depending on the measurements. A primary factor that dominates the QLL thickness may be the different methods used to detect the QLL phase on ice and to measure its thickness. For instance, Golecki and Jaccard [29] employed a channeling technique of nuclear backscattering that is sensitive to crystalline imperfection to detect the thickness of QLL on pure ice and found rather large values of the QLL thickness (e.g., ≈ 100 nm at -1 °C); while Doppenschmidt and Butt [6] measured the QLL thickness on ice surfaces by atomic force microscopy (AFM) and obtained much thinner data (e.g., ≈ 32 nm at -1 °C). Another dominative factor may be the surfaces with which ice crystals are in contact. Indeed, experimental studies have demonstrated that the thickness of the QLL between ice

and amorphous SiO_2 is always less than 10 nm [9,37]. Last but not least, the impurities of ice will also impact the surface melting and its thickness [18]. An AFM measurement on ice containing 10 mM KCl indicated that the QLL on the contaminated ice is much higher than that on pure ice [6]. For more data and discussions about QLL, the readers may refer to the comprehensive reviews [3,14,18] and a book chapter [1].

Since the thickness of QLL on ice is dominated by the actions on the intermediate phase, different physical interactions can induce different models (see for instance the models shown in Section 2.2). Indeed, those physical interactions depend on the surfaces to which ice crystals are exposed. For example, a theoretical study by Wettlaufer et al. [30] revealed that the premelting behavior of the ice confined in soils is beyond the classic van der Waals interactions, rather in the regime of the long-rang electrostatic interactions. This means that the potential-distance function can be represented by $F = 1 - \sigma^2/t^2$, so the thickness of the QLL on the soil-confined ice roughly conforms to Equation (5). Moreover, it was implied that the exponential decaying regime may be suitable to estimate the QLL thickness for freely-exposed ice crystals (Equation (3)), whereas the power decaying regime for those in contact with solid surfaces (Equation (4)) [14]. However, experimental data (e.g., [37]) suggested that the QLL between ice and SiO_2 substrate also conforms to the logarithmic law, $t \propto \ln(T_m - T)$. The data recalled in Figure 2 also imply that both the exponential and power decaying regimes may capture the same $t - T$ data to some extent.

One may also integrally consider both the short-and long-range potentials of the QLL on ice [4], which, however, will bring two inevitable troubles in assessing its thickness. The primary one is that the explicit and simple expressions like Equations (3) and (5) cannot be obtained, and complex numerical calculations are required. The other one is that the parameters of both the short-and long-range potentials are rather difficult to obtain, because how they work in establishing the QLL phase on a surface remains an open question [13]. Here, therefore, the simply uncoupled short-and long-range potentials are discussed to unravel the physical regimes of the QLL on ice.

Table 1. Selected $t - T$ curves.

Item	Value (nm)	Method	Ref.
d-1 (lower bound)	$t = 0.3$	Monolayer water molecule	[3]
d-2	$t = 1.97 \Delta T ^{(-1/3)}$	Estimated from sorption data	[31]
d-3	$t = 32 - 21\lg(\Delta T)$	Measured by AFM	[6]
d-4 (upper bound)	$t = 95 - 54\lg(\Delta T)$	Estimated by proton channeling	[29]

To elucidate the influences of QLL on the freezing behaviors of porous materials, we here representatively selected four $t - T$ curves, i.e., d-1 (monolayer water molecule), d-2 (power decay of the QLL potential, long-rang interaction), d-3, and d-4 (exponential decay of the QLL potential, short-range interaction) marked in Figure 2 and listed in Table 1. Specifically, the size of the monolayer water molecule (d-1) was set as the lower bound of the QLL thickness, even though it is not necessary to limit the QLL thickness [9]. The d-4 curve was set as the upper bound of the QLL thickness. We shall understand that the selected $t - T$ curves may not strictly conform to the freezing regimes we will discuss (i.e., freezing in pores); however, the interpretations on confined freezing with the QLL in different thickness models will shed much light on the engineering consequences of freezing where this intermediate phase is often ignored.

3. Ice Content in Porous Media

3.1. QLL-Modified GT Equation

One of the core issues concerning freezing in porous media is the ice content in the pores at a subzero temperature, which is vitally important due to the significant engineering consequences (e.g., weathering of stones and damage of buildings and infrastructures). Following the GT equation

and assuming that the freezing of water occurs in a cylindrical pore with radius r_p , we can rewrite Equation (1) as,

$$r_p = r_c + t = \frac{2T_0\gamma_{cl}}{\Delta H_f(T_0 - T_m)} + t \quad (6)$$

Here, the possible water-QLL-ice contact-line effect was not considered (if it exists). This expression suggests that the presence of QLL in thickness t can further depress the equilibrium temperature for ice formation in a confined space, as the curvature of the confined ice is altered by the QLL ($\kappa = 1/(r_p - t)$).

Figure 3a shows in what pore sizes the confined water can freeze under a certain temperature depression when different datasets of QLL thickness (Table 1) are employed. When plotting Figure 3, a constant value of $2T_0\gamma_{cl}/\Delta H_f \approx 30 \text{ nm} \cdot \text{K}$ was employed [19]. At a subzero temperature, thickening the QLL tends to enlarge the pore radius to accommodate the ice that should always match the pore curvature in equilibrium. This effect is more significant for the freezing in nanopores [15,38]. If we considered a pore with a radius of 100 nm, which is rigid (no frame deformation) and pre-saturated with water, then the ice content ($= (r - t)^2/r^2$ for cylindrical pores) would vary with the QLL thickness. As displayed in Figure 3b, ice occupies the whole pore in the cases of non-QLL and the QLL thickness of d-1 once the temperature drops to around -0.302°C . For the QLL thickness of d-2, which remains insignificant, the ice content instantaneously rises to around 96% at -0.305°C and then increases slightly due to the continual decrease in the QLL thickness. When the d-3 model of QLL thickness is used, the freezing temperature is depressed to around -0.53°C because the QLL-corrected size for ice is sharply narrowed to around 62 nm at this temperature; and the instantaneous ice content is depressed as well ($\phi_c = 0.62^2 = 0.38$). When the $t - T$ curve is governed by the d-4 model, the freezing temperature and the instantaneous ice content become -1.72°C and 0.03, respectively (Figure 3b). Due to the continually-thinning process of the QLL with the depressed temperature, the ice content continually increases.

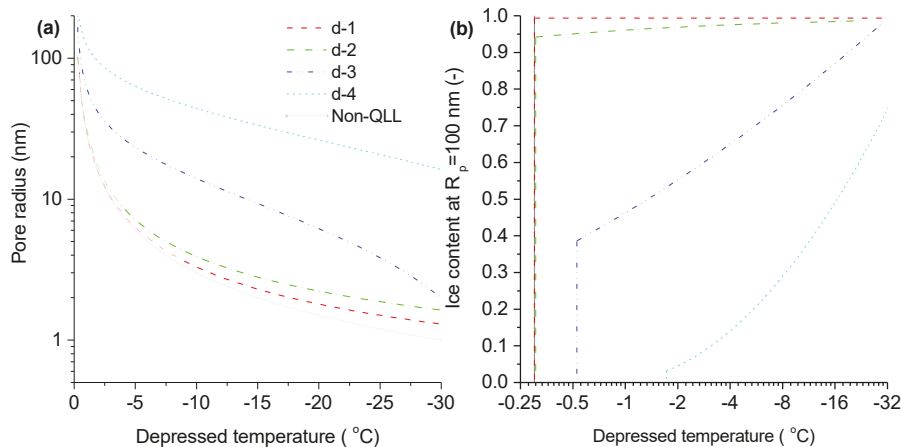


Figure 3. (a) The plots of pore radius against depressed temperature predicted by the Gibbs–Thompson (GT) equation with different datasets of QLL thickness; (b) the variation of ice content with depressed temperature in the pore of 100 nm.

Note that the real pore structure of porous materials would be much more complex than the simply mono-sized and cylindrical pores; therefore, the ice content would be also beyond the results displayed in Figure 3b. For macroporous and mesoporous materials, the contribution of the QLL to the ice (or liquid) fraction would be small relative to that of the GT effect [3,39]. For nano-porous materials, like porous silica [38], the QLL contribution cannot be neglected. Furthermore, for porous building

materials, e.g., cement-based materials that show very broad pore ranges from nano- to macro-sizes, the QLL effect may play its part at different pore scales to different extents. Furthermore, the value of $2T_0\gamma_{cl}/\Delta H_f$ may change with different surface and curvature conditions (21–53 nm·K [19]), but the specific value will not change the main observations displayed in Figure 3.

3.2. Pore Structure Associated Ice Content

We here took a real concrete sample as an example to demonstrate the QLL effect on the ice content in porous materials under freezing. The pore structure of the concrete was determined by mercury intrusion porosimetry (MIP). The MIP porosity and total porosity (in reference to the status of the sample dried at 105 °C) were 0.138 and 0.181, respectively. With the maximum mercury intrusion pressure of 414 MPa, the contact angle between the pore wall and mercury front of 130 ° and the surface tension between vapor and liquid mercury of 485 N/m, the pore size distribution (PSD) of the concrete sample can be obtained by the Washburn equation [40]; see the insert panel of Figure 4. Clearly, multiple peaks in the PSD curve can be observed due to the fact that different pores at different scales integrally dominate the pore spatial distribution. The pore peak around 10 µm (marked A in the insert panel in Figure 4) may denote the coarse capillary pores between the cement clinkers and the coarse pores in the interfacial transition zone (ITZ) between the aggregates and the cement matrix. The pore peak at 200 nm (marked B) may represent the capillary pores between the cement hydrates (or termed as the inter-particle space [41]). The peak at the thinner size (marked C) may reflect the thin capillary pores and coarse gel pores: the space between the layered C-S-H gel clusters. One shall understand that the very fine interlayer pores (<1 nm) cannot be detected by MIP [42]. Last but not the least, the pore structure measured by MIP may be biased by the oversimplified assumptions of the pore geometries and the physical principles (the Washburn equation) applied for the test.

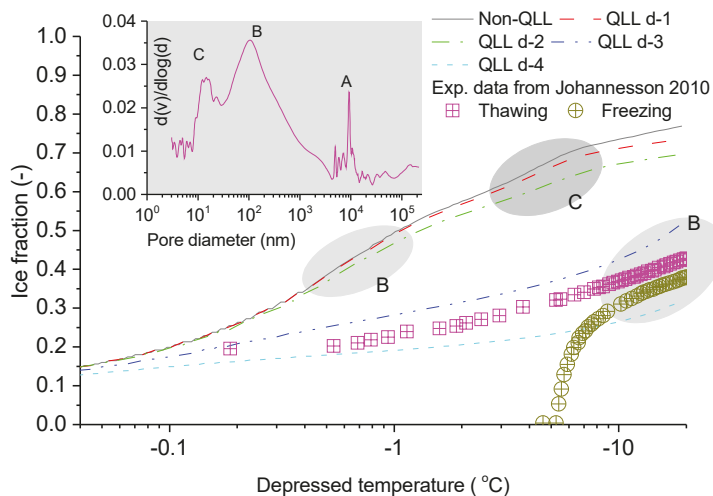


Figure 4. Ice fractions of a concrete sample (water to cement ratio of 0.6) under freezing estimated by the GT equation with the selected QLL models and the experimental ice content reported in [43]. The insert panel is the pore size distribution of the concrete determined by mercury intrusion porosimetry (MIP) with the marks A, B, and C, respectively, representing the coarse pores, capillary pores, and gels pores in the concrete sample. The shadowed areas with the same marks denotes the consequences of ice formation in those pores.

The ice content of the concrete sample can be estimated by the GT equation (Equation (6)) with the PSD data. Again, assuming that the penetration of ice in any pore is strictly under thermodynamic equilibrium and neglecting the possible effect of the ions in the pore fluid [44], the accumulative ice content ϕ_c at a temperature T can be given by:

$$\phi_c = \int_{T_0}^T \frac{\partial \phi_c}{\partial T} dT = \int_{T_0}^T \frac{\partial}{\partial r_c} \left[\int_{r_p}^{r_p^{GT}} \frac{\partial \phi_p}{\partial r_p} \left(1 - \frac{t(T)}{r_p} \right)^2 dr \right] \Big|_{r_p - t \geq r_c} \frac{\partial r_c}{\partial T} dT \quad (7)$$

where r_p^{GT} denotes the minimum pores in which ice can penetrate under the GT equation. In Equation (7), all parameters are known except for $\partial \phi_p / \partial r_p$, which can be read from the MIP PSD data. The expression in the square brackets represents the changes in ice content induced by both the filling of new pores and the thinning of QLLs. The readers may find some alternative methods to Equation (7) for estimating the ice content of porous materials under freezing by different porosimetries (e.g., [24,45,46]). In this study, because the minimum accessible pore radius of the MIP test was 1.5 nm, which yielded the required lowest temperature by the GT equation of -20 °C, the analyses thus stopped at this temperature.

Figure 4 shows the ice contents of the concrete sample with the selected QLL models. At first glance, the existence of QLL will always decrease the ice fraction at any subzero temperature, and the thicker is the QLL, the lower is the ice fraction. These can be reasonably understood as the supposed ice phase that is adjacent to the pore walls is replaced by the interfacial QLL phase. Due to the significant sensitivity of the ice front size to the depressed temperature in equilibrium, a very slight deviation of the temperature from the freezing point will cause a heavy filling of ice in the pores that are larger than the equilibrium GT size. For instance, a temperature shift down to -0.01 °C would cause the freezing of the pores larger than 3 μm, so the freezing of the pores at Mark A will not be shown in Figure 4. These ice-filled pores occupied around 13% of the total pore volume, and the QLL effect, as expected, was minor. This temperature drop is negligible in engineering, but shows remarkable impact on ice formation in macro pores, e.g., the pores in Mark A of the concrete sample. As temperature dropped further, the QLL effect rose. The ice fillings in the capillary pores (Mark B) and the gel pores (Mark C) can be reflected by the steeper plots of ice fraction against depressed temperature (Figure 4). For the cases of relatively small values of QLL thickness (e.g., d-1 and d-2), the similarly-shaped curves with the steep characteristic slopes at the same temperature intervals can be figured out. When the d-3 and d-4 models were used, the freezing of the water confined in the thin pores was significantly delayed or depressed. Obvious evidence was that the steep Stage B that initially began at around -0.4 °C was delayed to around -10 °C for the freezing of the water confined in the same pores with the very thick QLLs (Figure 4). Although those freezing delays were physically exaggerated because of the overestimated thickness values of the QLLs between the pore walls and the ice crystals by the d-3 and d-4 models, the results displayed in Figure 4 were mathematically reasonable. For instance, according to Equation (1), the pores with a width of 100 nm (radius of 50 nm) will freeze at -0.6 °C without the QLL effect, but the freezing temperature will be shifted to -8 °C with the QLL effect following the thickness model of d-4.

For comparison purposes, the experimental ice fractions of a concrete sample with the same water to cement ratio evaluated by the freezing and thawing phases of DSC measurement [43] are plotted in Figure 4. Due to the significant supercooling of water, ice crystals nucleated at -5 °C, then explosively grew in the pores that are larger than the GT size. After that, the ice growth that should be governed by the available pore water became much slower. At -20 °C, only 38% of the total pore water was frozen to ice, and it increased to 50% at -50 °C [43]. The ice fraction data from the thawing phase were slightly higher than those from the freezing phase after the nucleation stage (i.e., <-10 °C, Figure 4). The hysteresis of the ice fraction between freezing and thawing may come from the pore curvature-induced metastability of the confined phase, which is an intrinsic property of the pore system defined by the pore structure and the interfacial interactions [19]. Since the confined

thawing can avoid the supercooling effect, it generally approaches more closely the equilibrium case if the thawing speed is not very fast and thus is often adopted for pore structure measurement by cryoporometry [19,21]. The results plotted in Figure 4 show that the ice fraction curve with the QLL thickness of d-3 was close to that from the DSC thawing data [43]. However, this does not imply that the QLL thickness of d-3 dominated the intermediate QLL phase between the ice crystals and the pore walls of the concrete sample. As a matter of fact, two reasons may account for this observation. Firstly, the pore structure of the concrete sample may deviate from the real one since MIP only detects open pores in limited pore ranges (e.g., 3 nm in this study), and secondly, our estimation strictly relied on thermodynamic equilibrium, which cannot be achieved in either practice or rigorous experimental tests. Overall, the results displayed in Figure 4 indeed evidence the significant role QLL plays, and the integral understandings of this interfacial phase between ice crystals and substrates are wanted in the future.

4. Mechanical Consequences of Confined Freezing

4.1. Freezing Pressures

Once confined freezing takes place, the significant volume difference between ice and water will induce large hydraulic pressures on pore walls, which may mainly account for the frost damage in cement-based materials [23] and rocks [47], the frost heave in soils, and other relevant issues [3,48]. Here, we employed a simplified poroelastic model that involves the interactions among the ice, unfrozen water, and the material skeleton in the elastic regimes [24] to evaluate the hydraulic pressures. The effective hydraulic pressure over the pore-fluid domain in a porous material, $\langle P_d\phi \rangle$, can be given by [24]:

$$\langle P_d\phi \rangle \approx \frac{0.09K_s(1-\phi)^3\phi\phi_c}{2-2\phi^2+\phi^3} \quad (8)$$

where K_s is the bulk modulus of the material skeleton, and the constant 0.09 denotes the volume fraction change when water crystallizes to ice during freezing. When deducing Equation (8), the small density variations of ice and water were neglected, and the relation of $K = K_s(1-\phi)^3$ with K being the bulk modulus of the empty porous sample [49] was employed for exploring the porosity variation due to the deformation of the skeleton under pressure. Equation (8) indicates that the hydraulic pressure induced by the confined freezing was proportional to the ice content. Furthermore, softening the material skeleton will decrease the hydraulic pressure due to the fact that the deformations by the material itself can provide more space for pressure relaxation.

In addition to the hydraulic pressure, the crystallization process itself will also generate a pressure (termed as the crystallization pressure) on local pore walls even without volume change [50]. Unlike the hydraulic pressure that should be evenly and isotropically exerted on the entire pore system, the crystallization pressures acted on pore walls locally depending on the pore geometries and the depressed temperature. Therefore, the effective crystallization pressure over the ice-filled domain, $\langle P_c\phi_c \rangle$, can be given by,

$$\langle P_c\phi_c \rangle = \int_0^{\phi_c^{GT}} P_c d\phi_c \approx \sum (1-\lambda) \frac{\Delta H_f}{T_0} (T_0 - T_m) \Delta\phi_c \quad (9)$$

where ϕ_c^{GT} is the maximum equilibrium ice content according to the GT equation and λ is the shape factor, with $\lambda = 0.5$ and 1, respectively, representing the cylindrical and spherical pores [45]. An unsaturated freezing-thawing test suggested that the shape factor of concrete varied from 0.3–0.6 depending on the pore sizes [51]. In this study, $\lambda = 0.5$ was used, because the ice contents were calculated based on the pores of the cylinder.

Figure 5 displays the hydraulic and crystallization pressures estimated by Equations (8) and (9), respectively, based on the ice content data shown in Figure 4. During calculating, $K_s = 25$ GPa [52]

was used. As shown in Figure 5a, the significant hydraulic pressure shifts up to 14 MPa can be found immediately after the freezing begins (-0.01°C). This can be due to the instantaneous ice filling in the macro-pores (Figure 4). For the cases of non-QLL and low QLL thickness values (d-1 and d-2), the hydraulic pressures accumulated continually, heavily, and rapidly as the temperature decreased down to -1°C due to the large amount of ice forming in the capillary pores (Mark B in Figure 4). The further decreases in temperature to -6°C remained promoting the hydraulic pressures, but at slower rates, owing to the delayed ice formation in the gel pores at nano-scales. After that, decreasing temperature only generated limited ice crystals due to the limited pore water for freezing, which consequentially accumulates only slight hydraulic pressures. For the thick QLL cases (d-3 and d-4), the hydraulic pressures augmented continually and consistently at relatively slow rates after the rapid rises at the beginning stage of freezing (Figure 5a). Those, again, were the consequences of ice formations in confined freezing that were sensitive to the QLL thickness (Figure 4). For example, due to the very depressed ice formation in the pores with the thick QLL of d-4, the final hydraulic pressure at -20°C arrived at 36 MPa, only 40% of that without the QLL (88.5 MPa).

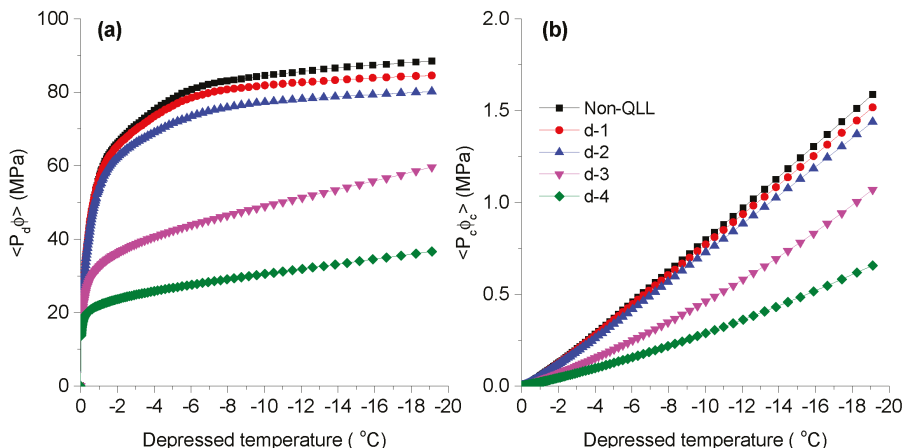


Figure 5. (a) Hydraulic pressures of confined freezing induced by the density change and (b) crystallization pressures induced by the curvature effect during freezing with different models of QLL thickness.

The crystallization pressures, unlike the hydraulic pressures that were primarily determined by the ice contents, showed different characteristics. Firstly, the crystallization pressures were far lower than the hydraulic pressures (less than 2 MPa; see Figure 5b). One shall understand that Equation (9) calculates the crystallization pressures that only work on locally-limited domains around ice crystals, which is different from the general expression without the working domains (e.g., $P_c \approx 1.2(T_0 - T_m)$ MPa [22,50]). Due to the very limited amount of the formed ice at each temperature decreasing step, the effective crystallization pressures were relatively small. Secondly, the crystallization pressures almost accumulated linearly with the temperature deceasing. This was intrinsically due to the algorithm of Equation (9), in which the weight factor $(T_0 - T_m)$ before $\Delta\phi_c$ always increased as the temperature deceased. However, the effect of QLL on the crystallization pressures remained similar to the hydraulic pressures, that is the thicker was the QLL, the lower were the pressures (Figure 5b).

Overall, the existence of QLL between ice crystals and pore walls tended to lower the effective hydraulic and crystallization pressures, and the former one was more sensitive to the amount and rate of ice accumulation in the confined freezing.

4.2. Links to Frost Deformations of Porous Materials

In order to bridge over the pressures that are generally exerted on local phases and the macro-deformations of porous materials that are integrally over the whole tested specimens, a poro-elastic approach [22,23,53,54] was employed. For a freely-deformable porous material without external restrictions, the linear deformation, ϵ , of the material under a subzero temperature can be given by,

$$\epsilon = \frac{< P_c \phi_c > + < P_d \phi >}{3K} + \alpha(T - T_0) \quad (10)$$

where α is the thermal expansion coefficient of the material. Here, $\alpha = 15.7 \times 10^{-6}$ (1/K) was estimated from the experimental data reported in [43].

Figure 6a shows the calculated freezing deformations of the concrete under freezing with the selected QLL thickness models. The material deformations were the direct consequences of the effective pore pressures (Figure 5). Clearly, the first freezing at the temperature shift down to -0.1°C will cause the instantaneous expansions up to 3.3×10^{-4} mm/mm for all cases, which was indeed due to the rapidly raised hydraulic pressures up to 15 MPa (Figure 5). Those significant expansions continued as the ice accumulated in big pores (Segment A in Figure 6a). Later, the deformations with different QLL models diverged and grew according to the combined actions of the effective pore pressures and the thermal shrinkages. For the cases of non-QLL and low-thickness QLLs (d-1 and d-2), the deformation rising extents and rates decreased progressively as the temperature decreased (Segment B in Figure 6a), which was indeed due to the delayed ice formation in the capillary and gel pores. At the same time, the material always shrank with the temperature decreasing (see the solid line in Figure 6a). When the rises in pore pressure induced by the ice crystallization in fine pores could not compensate for the thermal shrinkages, the material began to shrink. In this study, shrinkages started (although insignificantly; see Segment C in Figure 6a and the acquired shrinkages in Figure 6b) when the temperature was lowered to -8°C for the cases of non-QLL, d-1 and d-2. For the cases of d-3 and d-4, however, the material did not show shrinkages due to the fact that the freezing of the water confined in the capillary and gel pores was significantly delayed by the thick QLLs.

Figure 6a also displays the deformations of concrete upon freezing and thawing obtained from experimental measurements [43]. Four deformation segments can be singled out from the freezing deformation-temperature curve. A slight shrinkage occurred at $T > -1^\circ\text{C}$ (Segment S in Figure 6) owing to the supercooling of the confined water that may be attributed to either the actions of the dissolved ions [44] or the natural kinetic-associated freezing process that requires a meta-stable status beyond the thermodynamic equilibria [25]. Later, in the temperature range between -1°C and -2.6°C , freezing deformation rose rapidly and significantly (Segment A') due to the ice formation in the coarse pores. Then, the deformation rise became less and slower between -2.6°C and -7.5°C (Segment B'), followed by a constantly increased, but rather minor deforming stage (Segment C') below -7.5°C due to the continually-depressed ice formations. Roughly, the freezing deformations were close to the results of the non-QLL, d-1 and d-2 cases, predicted by the poroelastic analyses (Figure 6b), while the thawing data to those of d-3 and d-4 cases. This may inform that the poroelastic analysis can, to some extent, capture the physical regimes of confined freezing. Similar results were reported elsewhere [22,24]. However, large deviations between the experimental and predicted data can be observed at the early freezing stages. Specifically, the very first supercooling stage (Segment S) cannot be captured by the model because our predictions were strictly under thermodynamic equilibria and the pore water was only physically regulated by the curvature effect. The deviations from equilibrium cannot be avoided for a real freezing test, so the ice formation in any pore scale would always be delayed, which would cause biases between the predicted and measured deformations, as displayed in Figure 6. Indeed, the crystallization of the massive supercooled water in confined pores can cause a so-called thermal-shock effect that may bring additional damage to the porous material under freezing [55]. Another important reason accounting for the deformation deviations between the

experimental and modeled results may be the pore pressure relaxation that always occurs in the real freezing process of porous media [23,56], but was not considered here.

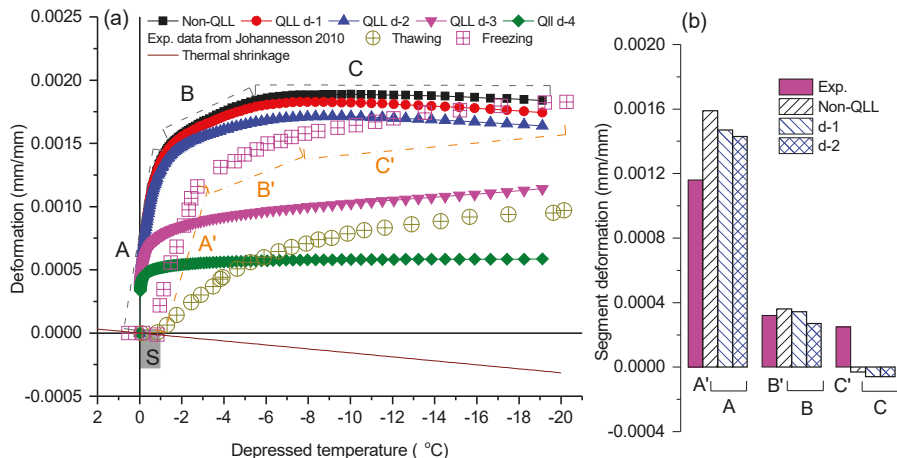


Figure 6. (a) Deformations of the concrete sample estimated by the poroelastic model with the different models of QLL thickness and the experimental results reported in [43]. In this figure, the experimental thawing data were corrected according to the set of $\epsilon = 0$ at $T = T_0$. Three segments of the modeled freezing deformations with different rising extents are marked as A, B, and C to represent the significant, moderate, and slight deformation rises by the delayed ice formation in different pores. The same freezing stages for the experiment data are marked as A', B', and C', respectively. The process of supercooling monitored by the experiments is marked as S. (b) The comparison of the deformations at each segment between the experimental data and the predicted results in the non- and low-thickness QLL cases (d-1 and d-2).

Despite the acceptable agreements between the experimental and predicted deformations, some important issues that are intimately related to the complex confined freezing, but have not been fully addressed in the present study deserve further discussion. Firstly, the thermodynamic and structurally-configurational properties of the water and ice confined in nanopores were assumed to be the same as those of the bulk phases. This assumption may be challenged by the disordered structure of ice and water by the actions of pore walls [18]. For instance, it was reported that water in nanopores freezes to cubic ice instead of hexagonal ice with lower free energy [15,16]. Secondly, the possible influences of high pressure on the structure and physical properties of the confined water, ice, and QLLs were not considered here, while the increasingly-reported evidence has supported that high pressures can substantially change the crystal structures of ice and its growth mechanisms [17,57]. Thirdly, the pore structure of cement-based materials is far more complex than the grade cylinders as assessed by the MIP method. Our previous studies indicated that the pores (and their surfaces) in cement-based materials are constructed in “chaos” (or fractal) patterns [26]. Theoretical analyses showed that fractal substrates can substantially impact the nucleation rate and crystal size [58–60]. For a material with such complex pores, the local curvature effect may further influence local ice structures and, consequentially, freezing kinetics and the stresses generated [61,62]. Last but not least, our predictions were carried out under the elastic regime, in which all phases deformed elastically and linearly with the pressures generated by different sources. Local pressures (e.g., crystallization pressures) were homogenized into some pattern (Equation (9)) to get the integral body stresses, which may be too simple to represent the real stress field in the material. Deepened understandings of the influences of those issues on the ice-QLL-substrate system and the engineering consequences deserve further rigorous investigations in the future.

5. Conclusions

- The intermediate phase, QLL, with a structure different from ice and water, exists to stabilize the ice exposed to different media or in contact with different substrates under freezing. The thickness of QLL generally decays with the temperature decreasing, which can be captured by the thermodynamic models with the long-and short-range interactions between the ice and the substrate.
- Four different models of QLL thickness were representatively employed to correct the GT equation and to address its effect on the ice content of a concrete sample, whose pore structure was determined by MIP. Under thermodynamic equilibria, the concrete with broad PSD at multiple scales showed the unevenly rising extents and rates of ice against the depressed temperature. The thickened QLL can delay the freezing temperature and depress the ice content of the water confined in the pores.
- When confined freezing occurs in a porous material, the hydraulic pressures due to the volume difference between ice and water build up depending on the pore structure and material properties. The crystallization pressures that are generated by the penetration of ice into thin pores almost increase linearly with the depressed temperature. Both pressures decrease with thickening of the QLL.
- The freezing deformations of porous materials depend on the effective pore pressures built by the confined freezing and the thermal shrinkages during freezing. The QLL corrections seem to mitigate the deviations between the predicted and measured freezing deformations. The underlined physical regimes are indeed associated with the QLL-associated ice content in freezing pores, and some related issues remain to be advanced in the future.

Author Contributions: Q.Z. and K.L. contributed equally to this work.

Funding: The research was funded by the National Natural Science Foundation of China (Nos. 51878602 and 51778332).

Acknowledgments: The authors acknowledge the anonymous reviewers to improve the quality of this study.

Conflicts of Interest: The authors declare no conflict of interest.

Appendix A

The free energy changes $\Delta G(T, t)$ of the representative water-filled pore before and after freezing, which depend on the temperature T and QLL thickness t , can be given by,

$$\Delta G(T, t) = \underbrace{\frac{T - T_0}{T_0} \Delta H_f V_c}_{\text{Freezing heat}} + \underbrace{\gamma_{lc} A_c}_{\text{New surface}} + \underbrace{\Delta \gamma A_p F(t)}_{\text{Disturbance in surface energy}} \quad (\text{A1})$$

Note that Equation (A1) is different from the generally used expression that only involves the local surface-energy changes by the intermediate phase ($\Delta G(T, t) = \gamma_{lc} + \Delta \gamma F(t)$) [3]. More discussions about Equation (A1) can be found elsewhere [3,4,27].

Since the intermediate QLL is generated to stabilize the ice-solid system, the total free energy is required to be minimal in equilibrium. The partial derivative of $\Delta G(T, t)$ with respect to t was then conducted in Equation (A1), which yields,

$$\frac{\partial \Delta G(T, t)}{\partial t} = 0 = -A_p \left[\frac{T - T_0}{T_0} \Delta H_f (1 - 2\kappa t) + 2\kappa \gamma_{lc} - \Delta \gamma \frac{\partial F(t)}{\partial t} \right] \quad (\text{A2})$$

When deducing Equation (A2), the relations, $\partial V_c / \partial t = -A_p (1 - 2\kappa t)$ and $\partial A_c / \partial t = -2\kappa A_p$ from Equation (2), were used. Considering further the limited contribution of the QLL (i.e., $2\kappa t \ll 1$) and the GT equation (Equation (1)), Equation (A2) reduces to $\partial F / \partial t = \Delta H_f (T - T_m) / \Delta \gamma T_0$. This relation reveals that the differential interfacial potential against thickness is primarily determined by

the changes in temperature ($T - T_m$). Estimating the thickness of QLL relies on how the interfacial potential $F(t)$ is chosen, although the required parameters may vary conditionally (e.g., $\Delta\gamma$).

References

1. Furukawa, Y. Snow and ice crystal growth. In *Handbook of Crystal Growth*, 2nd ed.; Elsevier Science: Amsterdam, The Netherlands, 2015; pp. 1061–1112.
2. Murata, K.; Asakawa, H.; Nagashima, K.; Furukawa, Y.; Sasaki, G. Thermodynamic origin of surface melting on ice crystals. *Proc. Natl. Acad. Sci. USA* **2016**, *113*, E6741–E6748. [[CrossRef](#)]
3. Dash, J.G.; Rempel, A.W.; Wetzlaufer, J.S. The physics of premelted ice and its geophysical consequences. *Rev. Mod. Phys.* **2006**, *78*, 695–741. [[CrossRef](#)]
4. Limmer, D.T. Closer look at the surface of ice. *Proc. Natl. Acad. Sci. USA* **2016**, *113*, 12347–12349. [[CrossRef](#)]
5. Mochizuki, K.; Molinero, V. Antifreeze glycoproteins bind reversibly to ice via hydrophobic groups. *J. Am. Chem. Soc.* **2018**, *140*, 4803–4811. [[CrossRef](#)] [[PubMed](#)]
6. Doppenschmidt, A.; Butt, H.J. Measuring the thickness of the liquid-like layer on ice surfaces with atomic force microscopy. *Langmuir* **2000**, *16*, 6709–6714. [[CrossRef](#)]
7. Limmer, D.T.; Chandler, D. Premelting, fluctuations, and coarse-graining of water-ice interfaces. *J. Chem. Phys.* **2014**, *141*, 18C505. [[CrossRef](#)]
8. Bluhm, H.; Ogletree, D.F.; Fadley, C.S.; Hussain, Z.; Salmeron, M. The premelting of ice studied with photoelectron spectroscopy. *J. Phys. Condens. Matter* **2002**, *14*, L227. [[CrossRef](#)]
9. Liljeblad, J.F.; Furo, I.; Tyrode, E.C. The premolten layer of ice next to a hydrophilic solid surface: Correlating adhesion with molecular properties. *Phys. Chem. Chem. Phys.* **2017**, *19*, 305–317. [[CrossRef](#)] [[PubMed](#)]
10. Conde, M.M.; Vega, C.; Patrykiejew, A. The thickness of a liquid layer on the free surface of ice as obtained from computer simulation. *J. Chem. Phys.* **2008**, *129*, 014702. [[CrossRef](#)]
11. Furukawa, Y.; Nada, H. Anisotropic surface melting of an ice crystal and its relationship to growth forms. *J. Phys. Chem. B* **1997**, *101*, 6167–6170. [[CrossRef](#)]
12. Dosch, H.; Lied, A.; Bilgram, J.H. Glancing-angle X-ray scattering studies of the premelting of ice surfaces. *Surf. Sci.* **1995**, *327*, 145–164. [[CrossRef](#)]
13. Carrasco, J.; Hodgson, A.; Michaelides, A. A molecular perspective of water at metal interfaces. *Nat. Mater.* **2012**, *11*, 667–674. [[CrossRef](#)]
14. Dash, J.G.; Fu, H.; Wetzlaufer, J.S. The premelting of ice and its environmental consequences. *Rep. Prog. Phys.* **1995**, *58*, 115–167. [[CrossRef](#)]
15. Han, Y.Y.; Shuai, J.; Lu, H.M.; Meng, X.K. Size- and dimensionality-dependent thermodynamic properties of ice nanocrystals. *J. Phys. Chem. B* **2012**, *116*, 1651–1654. [[CrossRef](#)] [[PubMed](#)]
16. Jelassi, J.; Castricum, H.L.; Bellissent-Funel, M.C.; Dore, J.; Webber, J.B.W.; Sridi-Dorbez, R. Studies of water and ice in hydrophilic and hydrophobic mesoporous silicas: Pore characterisation and phase transformations. *Phys. Chem. Chem. Phys.* **2010**, *12*, 2838–2849. [[CrossRef](#)] [[PubMed](#)]
17. Nada, H. Analysis of ice crystal growth shape under high pressure using molecular dynamics simulation. *Cryst. Growth Des.* **2011**, *11*, 3130–3136. [[CrossRef](#)]
18. Bjorneholm, O.; Hansen, M.H.; Hodgson, A.; Liu, L.-M.; Limmer, D.T.; Michaelides, A.; Pedevilla, P.; Rossmeisl, J.; Shen, H.; Tocci, G.; et al. Water at interfaces. *Chem. Rev.* **2016**, *116*, 7698–7726. [[CrossRef](#)]
19. Petrov, O.V.; Furo, I. NMR cryoporometry: Principles, applications and potential. *Prog. Nucl. Magn. Reson. Spectrosc.* **2009**, *54*, 97–122. [[CrossRef](#)]
20. Sun, Z.; Scherer, G.W. Pore size and shape in mortar by Themoporosimetry. *Cem. Concr. Res.* **2010**, *40*, 740–751. [[CrossRef](#)]
21. Mitchell, J.; Webber, J.B.W.; Strange, J.H. Nuclear magnetic resonance cryoporometry. *Phys. Rep.* **2008**, *461*, 1–36. [[CrossRef](#)]
22. Zeng, Q.; Fen-Chong, T.; Li, K. Freezing behavior of cement pastes saturated with NaCl solution. *Constr. Build. Mater.* **2014**, *59*, 99–110. [[CrossRef](#)]
23. Zeng, Q.; Fen-Chong, T.; Dangla, P.; Li, K. A study of freezing behavior of cementitious materials by poromechanical approach. *Int. J. Solid Struct.* **2011**, *48*, 3267–3273. [[CrossRef](#)]

24. Zeng, Q.; Li, K.; Fen-Chong, T. Elastic behavior of saturated porous materials under undrained freezing. *Acta Mech. Sin.* **2013**, *29*, 827–835. [[CrossRef](#)]
25. Zeng, Q.; Li, K.; Fen-Chong, T. Heterogeneous nucleation of ice from supercooled NaCl solution confined in porous cement paste. *J. Cryst. Growth* **2015**, *409*, 1–9. [[CrossRef](#)]
26. Zeng, Q.; Luo, M.; Pang, X.; Li, L.; Li, K. Surface fractal dimension: An indicator to characterize the microstructure of cement-based porous materials. *Appl. Surf. Sci.* **2013**, *282*, 302–307. [[CrossRef](#)]
27. Petrov, O.V.; Vargas-Florencia, D.; Furo, I. Surface melting of octamethylcyclotetrasiloxane confined in controlled pore glasses: Curvature effects observed by ^1H NMR. *J. Phys. Chem. B* **2007**, *111*, 1574–1581. [[CrossRef](#)]
28. Likos, C.N.; Mecke, K.R.; Wagner, H. Statistical morphology of random interfaces in microemulsions. *J. Chem. Phys.* **1995**, *102*, 9350–9361. [[CrossRef](#)]
29. Golecki, I.; Jaccard, C. Intrinsic surface disorder in ice near the melting point. *J. Phys. C Solid State Phys.* **1978**, *11*, 4229–4237. [[CrossRef](#)]
30. Wettslaufer, J.S.; Worster, M.G.; Wilen, L.A.; Dash, J.G. A theory of premelting dynamics for all power law forces. *Phys. Rev. Lett.* **1996**, *76*, 3602–3605. [[CrossRef](#)]
31. Fagerlund, G. Determination of pore-size distribution from freezing-point depression. *Mater. Struct.* **1973**, *6*, 215–225. [[CrossRef](#)]
32. Brun, M.; Lallement, A.; Quinson, J.F.; Eyraud, C. A new method for the simultaneous determination of the size and the shape of pores: The thermoporometry. *Thermochim. Acta* **1977**, *21*, 59–88. [[CrossRef](#)]
33. Goertz, M.P.; Zhu, X.Y.; Houston, J.E. Exploring the liquid-like layer on the ice surface. *Langmuir* **2009**, *25*, 6905–6908. [[CrossRef](#)]
34. Sadtchenko, V.; Ewing, G.E. Interfacial melting of thin ice films: An infrared study. *J. Chem. Phys.* **2002**, *116*, 4686–4697. [[CrossRef](#)]
35. Elbaum, M.; Lipson, S.G.; Dash, J.G. Optical study of surface melting on ice. *J. Cryst. Growth* **2002**, *129*, 491–505. [[CrossRef](#)]
36. Gilpin, R.R. Theoretical studies of particle engulfment. *J. Colloid Interface Sci.* **1980**, *74*, 44–63. [[CrossRef](#)]
37. Engemann, S.; Reichert, H.; Dosch, H.; Bilgram, J.; Honkimaki, V.; Snigirev, A. Interfacial melting of ice in contact with SiO_2 . *Phys. Rev. Lett.* **2004**, *92*, 205701. [[CrossRef](#)]
38. Jahnert, S.; Vacca Chavez, F.; Schaumann, G.E.; Schreiber, A.; Schonhoff, M.; Findenegg, G.H. Melting and freezing of water in cylindrical silica nanopores. *Phys. Chem. Chem. Phys.* **2008**, *10*, 6039–6051. [[CrossRef](#)] [[PubMed](#)]
39. Cahn, J.W.; Dash, J.G.; Fu, H. Theory of ice premelting in monosized powders. *J. Cryst. Growth* **1992**, *123*, 101–108. [[CrossRef](#)]
40. Washburn, E.W. Note on a method of determining the distribution of pore sizes in a porous material. *Proc. Natl. Acad. Sci. USA* **1921**, *7*, 115–116. [[CrossRef](#)]
41. Jiang, C.; Guo, W.; Chen, H.; Zhu, Y.; Jin, C. Effect of filler type and content on mechanical properties and microstructure of sand concrete made with superfine waste sand. *Constr. Build. Mater.* **2018**, *192*, 442–449. [[CrossRef](#)]
42. Muller, A.C.A.; Scrivener, K.L. A reassessment of mercury intrusion porosimetry by comparison with ^1H NMR relaxometry. *Cem. Concr. Res.* **2017**, *100*, 350–360. [[CrossRef](#)]
43. Johannesson, B. Dimensional and ice content changes of hardened concrete at different freezing and thawing temperatures. *Cem. Concr. Compos.* **2010**, *32*, 73–83. [[CrossRef](#)]
44. Wu, M.; Johannesson, B.; Geiker, M. A preliminary study of the influence of ions in the pore solution of hardened cement pastes on the porosity determination by low temperature calorimetry. *Thermochim. Acta* **2014**, *589*, 215–225. [[CrossRef](#)]
45. Wang, Z.; Zeng, Q.; Wu, Y.; Wang, L.; Yao, Y.; Li, K. Relative humidity and deterioration of concrete under freeze-thaw load. *Constr. Build. Mater.* **2014**, *62*, 18–27. [[CrossRef](#)]
46. Fabbri, F.; Fen-Chong, T. Indirect measurement of the ice content curve of partially frozen cement based materials. *Cold Reg. Sci. Technol.* **2013**, *90–91*, 14–21. [[CrossRef](#)]
47. Huang, S.; Liu, Q.; Liu, Y.; Ye, Z.; Cheng, A. Freezing strain model for estimating the unfrozen water content of saturated rock under low temperature. *Int. J. Geomech.* **2018**, *18*, 04017137. [[CrossRef](#)]

48. Bartels-Rausch, T.; Jacobi, H.W.; Kahan, T.F.; Thomas, J.L.; Thomson, E.S.; Abbatt, J.P.D.; Ammann, M.; Blackford, J.R.; Bluhm, H.; Boxe, C.; et al. A review of air–ice chemical and physical interactions (AICI): Liquids, quasi-liquids, and solids in snow. *Atmos. Chem. Phys.* **2014**, *14*, 1587–1633. [[CrossRef](#)]
49. Fen-Chong, T.; Fabbri, A.; Thiery, M.; Dangla, P. Poroelastic analysis of partial freezing in cohesive porous materials. *J. Appl. Mech.* **2013**, *80*, 020910. [[CrossRef](#)]
50. Scherer, G.W. Crystallization in pores. *Cem. Concr. Res.* **1999**, *29*, 1347–1358. [[CrossRef](#)]
51. Wang, Z.; Zeng, Q.; Wang, L.; Yao, Y.; Li, K. Effect of moisture content on freeze–thaw behavior of cement paste by electrical resistance measurements. *J. Mater. Sci.* **2014**, *49*, 4305–4314. [[CrossRef](#)]
52. Ghabezloo, S. Association of macroscopic laboratory testing and micromechanics modelling for the evaluation of the poroelastic parameters of a hardened cement paste. *Cem. Concr. Res.* **2010**, *40*, 1197–1210. [[CrossRef](#)]
53. Coussy, O. Poromechanics of freezing materials. *J. Mech. Phys. Solids* **2005**, *53*, 1689–1718. [[CrossRef](#)]
54. Liu, L.; Qin, S.; Wang, X. Poro-elastic—Plastic model for cement-based materials subjected to freeze-thaw cycles. *Constr. Build. Mater.* **2018**, *184*, 87–99. [[CrossRef](#)]
55. Demirdag, S. Effects of freezing–thawing and thermal shock cycles on physical and mechanical properties of filled and unfilled travertines. *Constr. Build. Mater.* **2013**, *47*, 1395–1401. [[CrossRef](#)]
56. Coussy, O.; Fen-Chong, T. Crystallization, pore relaxation and micro-cryosuction in cohesive porous materials. *CR Mec.* **2005**, *333*, 507–512. [[CrossRef](#)]
57. Suh, D.; Yasuoka, K. Heterogeneous cavitation and crystallisation with an impurity by molecular dynamics. *Mol. Simul.* **2018**, *44*, 530–533. [[CrossRef](#)]
58. Zeng, Q. A simple method for estimating the size of nuclei on fractal surfaces. *J. Cryst. Growth* **2017**, *475*, 49–54. [[CrossRef](#)]
59. Yan, D.; Zeng, Q.; Xu, S.; Zhang, Q.; Wang, J. Heterogeneous nucleation on concave rough surfaces: Thermodynamic analysis and implications for nucleation design. *J. Phys. Chem. C* **2016**, *120*, 10368–10380. [[CrossRef](#)]
60. Zeng, Q.; Xu, S. Thermodynamics and characteristics of heterogeneous nucleation on fractal surfaces. *J. Phys. Chem. C* **2015**, *119*, 27426–27433. [[CrossRef](#)]
61. Morishige, K. Influence of pore wall hydrophobicity on freezing and melting of confined water. *J. Phys. Chem. C* **2018**, *122*, 5013–5019. [[CrossRef](#)]
62. Kastelowitz, N.; Molinero, V. Ice–liquid oscillations in nanoconfined water. *ACS Nano* **2018**, *12*, 8234–8239. [[CrossRef](#)] [[PubMed](#)]



© 2019 by the authors. Licensee MDPI, Basel, Switzerland. This article is an open access article distributed under the terms and conditions of the Creative Commons Attribution (CC BY) license (<http://creativecommons.org/licenses/by/4.0/>).

Article

Negative Thermal Expansivity of Ice: Comparison of the Monatomic mW Model with the All-Atom TIP4P/2005 Water Model

Muhammad Mahfuzh Huda ¹, Takuma Yagasaki ², Masakazu Matsumoto ² and Hideki Tanaka ^{2,*}

¹ Graduate School of Natural Science and Technology, Okayama University, Tsushima-naka, Okayama 700-8530, Japan; hudamahfuzh@gmail.com

² Research Institute for Interdisciplinary Science, Okayama University, Tsushima-naka, Okayama 700-8530, Japan; t.yagasaki@gmail.com (T.Y.); vitroid@gmail.com (M.M.)

* Correspondence: htanakaa@okayama-u.ac.jp; Tel.: +81-86-251-7769

Received: 28 March 2019; Accepted: 12 May 2019; Published: 14 May 2019

Abstract: We calculate the thermal expansivity of ice I for the monatomic mW model using the quasi-harmonic approximation. It is found that the original mW model is unable to reproduce the negative thermal expansivity experimentally observed at low temperatures. A simple prescription is proposed to recover the negative thermal expansion by re-adjusting the so-called tetrahedrality parameter, λ . We investigate the relation between the λ value and the Grüneisen parameter to explain the origin of negative thermal expansion in the mW model and compare it with an all-atom water model that allows the examination of the effect of the rotational motions on the volume of ice.

Keywords: Negative thermal expansivity; mW model; Grüneisen parameter

1. Introduction

Liquid water freezes into ice I under ambient pressure. One of interesting characteristics of ice I is its negative thermal expansivity at low temperatures [1–5]. This was also recovered by theoretical study [6]. The thermal expansivity of a crystal can be related to the so-called Grüneisen parameter. For a mode with frequency ν , this parameter is defined as $\gamma = -(d \ln \nu / d \ln V)$ [7]. The quantity is positive for stretching modes. This is evident from the sharp increase in the potential energy with a decrease in the bond length caused by the Pauli exclusion principle. By contrast, the Grüneisen parameter can be negative for bending modes. The negative thermal expansivity is realized when the Grüneisen parameter of the bending modes is negative and the positive contribution from the stretching modes is small enough.

The Gibbs energy calculation with the quasi-harmonic approximation is a useful computational approach to examine the thermal properties of crystals [8]. This method allows for the calculation of the temperature dependence of the equilibrium volume of a crystal, from which one can obtain the thermal expansivity. It also enables one to calculate the components of the thermal expansivity, that is, the heat capacity and the Grüneisen parameters of individual intermolecular vibrational modes. The quality of the results depends strongly on the employed force field. Excellent results can be obtained from ab initio methods considering a high level electron correlation with a large basis set, but such calculations are quite time-consuming and may therefore not be suitable for the treatment of ice I, for which the system size and the number of examined configurations should be large enough to take the hydrogen-disorder into account [9]. In addition, properties of molecular solids, including ice, are sensitive to van der Waals interactions while empirical models to correct the van der Waals interactions for density functional theory (DFT) methods are not specialized for ice [10]. At this point, classical force fields modelled to reproduce properties of ice I work better than

ab initio force fields, except for the cleavage of chemical bonds. Of course, the ab initio calculation and the path integral method are useful for examining the isotope effects and for taking into account the anharmonic contributions [11–13]. Some discussions on the most effective method among these types of calculations has been conducted [14].

Here, we take advantage of the excellent reproducibility of classical force fields parameterized for liquid water and ice polymorphs. In passing, this kind of approach costs rather little, so that we can handle not only a larger number of molecules (say 1000) in the simulation cell but also many hydrogen-disordered structures, such as 100 different structures. The TIP4P/2005 model is one such classical force field [15]. A water molecule consists of one oxygen atom without charge, two positively charged hydrogen atoms, and one negatively charged site without mass. The oxygen atom interacts with oxygen atoms of other molecules via the Lennard-Jones (LJ) potential. This model reproduces the phase diagram of ice for a wide range of pressure except for the very high pressure region [16–19]. TIP4P/2005 is a re-parameterized TIP4P model [20]. It has been demonstrated that the thermal expansivity of ice I is negative at temperatures that are under 60 K when the original TIP4P model is employed [6]. A similar method was applied to ice II and III [21].

The monatomic water (mW) model is a different type of empirical model for water [22]. This is a single site water model, and the intermolecular interactions are described by the sum of the short-ranged pair and three-body interactions. The computational cost of the mW model is quite low because the number of interaction sites is reduced and because the long-range interactions are omitted. Nevertheless, this model reproduces various properties of ice I well, such as the melting point. It has been used frequently in molecular dynamics (MD) studies of nucleation and growth of not only ice I but also clathrate hydrates [23,24]. The mW model was developed on the basis of the Stillinger-Weber silicon model [25]. Although crystalline Si exhibits negative thermal expansivity, the Stillinger-Weber Si potential does not reproduce this anomaly [26].

The negative thermal expansivity of ice Ih has recently been measured in *a* and *c* lattice directions. Both measurements show an anisotropy in the thermal expansion between the *a*-axis and *c*-axis [3–5]. The temperature of the minimum thermal expansivity in those experiments shifts toward a low temperature, around 30 K. The negative thermal expansivity is observed for some crystals with open network structures, such as silicon, quartz, and silica zeolites. This fact suggests that the preference of a molecule for a regular tetrahedral arrangement, which is the origin of the low density of ice, is an important factor for the negative thermal expansivity [27]. In the mW model, the preference is implemented by a parameter in the three body interaction term. In this study, we calculate the thermal expansivity of ice I using the quasi-harmonic approximation and examine the effect of this tetrahedrality parameter on the thermal expansivity. We also calculate the thermal expansivity for the TIP4P/2005 model. The vibrational modes can be classified into the translation-dominant and rotation-dominant modes because it is an all-atom model. We demonstrate that the coupling between the two types of modes plays a vital role for the negative thermal expansivity of ice.

Our aim in this work is to explore how the mW model works in low temperatures by examining the thermal expansivity of ice. The original potential for the Si atom has been made, and the negative thermal expansion is recovered for amorphous Si only [28]. Therefore, it is of interest to examine if the mW model can reproduce the negative thermal expansivity and how to revise it to lead to its better reproducibility.

2. Method

2.1. Force Field Models and Structure of Ice

The potential energy of the mW model is the sum of the pairwise and three-body interactions [22]:

$$E = \varepsilon \sum_i \sum_{j>i} \phi_2(r_{ij}) + \sum_i \sum_{j\neq i} \sum_{k>j} \phi_3(r_{ij}, r_{ik}, \theta_{ijk}), \quad (1)$$

with

$$\phi_2(r) = A \left[B \left(\frac{\sigma}{r} \right)^4 - 1 \right] \exp \left(\frac{\sigma}{r - a\sigma} \right), \quad (2)$$

and

$$\phi_3(r, s, \theta) = \lambda [\cos \theta - \cos \theta_0]^2 \exp \left(\frac{\gamma \sigma}{r - a\sigma} \right) \exp \left(\frac{\gamma \sigma}{s - a\sigma} \right). \quad (3)$$

The parameters are given in Table 1. The interaction is short-ranged: a molecule interacts with a different molecule only when the distance between them is shorter than $a\sigma = 0.43065$ nm. The three-body term is zero when the O-O-O angle is the tetrahedral angle of $\theta_0 = 109.47^\circ$, and otherwise it is positive. Therefore, the preference for tetrahedral arrangements increases with the increase of the coefficient of the three body term, λ . In the mW model, this tetrahedrality parameter is set to 23.15 to reproduce various properties of ice I and liquid water [22,24,29].

Table 1. Parameters of the mW model [22].

A	7.049556277
B	0.6022245584
γ	1.2
a	1.8
λ	23.15
θ_0	109.47°
σ	0.23925 nm
ε	25.895 kJ mol ⁻¹

The TIP4P/2005 model is an all-atom rigid model for water [15]. The intermolecular interactions are described by pairwise additive Coulomb and LJ interactions. A negatively charged site without mass, M, is located on the bisector of the H-O-H angle with an O-M distance of 0.01546 nm. The O-H distance and the H-O-H angle are 0.09572 nm and 104.52° , respectively. The partial charge on each hydrogen atom is 0.5564 e. The LJ parameters of the oxygen atom are $\sigma_O = 0.31589$ nm and $\varepsilon_O = 0.774912$ kJ mol⁻¹.

The structure of ice in this study is ice Ic, consisting of 1000 water molecules. A hundred hydrogen-disordered ice structures without net polarization are generated for the TIP4P/2005 model by the GenIce tool [30]. For ices with the mW model, oxygen atoms are simply placed on the corresponding lattice sites. The calculations are performed for numerous densities. The shape of the cell is kept cubic throughout the expansion or compression. Periodic boundary conditions are applied to ensure that the molecules are in the bulk phase without any surface effect.

2.2. Quasi-Harmonic Approximation

The Helmholtz energy of ice can be expressed as:

$$A(T, V) = U_q(V) + F(T, V) - TS_c, \quad (4)$$

where $U_q(V)$ is the potential energy at 0 K, $F(T, V)$ is the vibrational free energy, and S_c is the configurational entropy. The vibrational free energy consists of the harmonic and anharmonic contributions. The anharmonic part can be ignored at low temperatures at which the potential energy surface is regarded to be parabolic in any direction. The harmonic vibrational free energy is given by:

$$F_h(T, V) = k_B T \sum_i \ln \left[2 \sinh \left(\frac{h \nu_i}{2 k_B T} \right) \right], \quad (5)$$

where h is the Planck constant, k_B is the Boltzmann constant, and ν_i is the frequency of the i -th normal mode. The steepest descent method is employed to obtain the crystalline configuration at $T = 0$ K and its potential energy, $U_q(V)$. Then, we calculate the mass-weighted Hessian matrix and diagonalize it to obtain the normal mode frequencies. The equilibrium volume, $\langle V \rangle$, at a given pressure, p , and at a temperature, T , is the volume that minimizes the following thermodynamic potential:

$$\Psi(V; T, p) = A(T, V) + pV. \quad (6)$$

The pressure is set to 0.1 MPa in all of the calculations. The Gibbs free energy is given by:

$$G(T, p) = \Psi(\langle V \rangle; T, p). \quad (7)$$

3. Results

As will be shown below, the thermal expansivity is connected with the frequencies of the intermolecular vibrations via the Grüneisen parameter and the heat capacity. Therefore, some vibrational modes play a significant role in the appearance of its anomaly under cryogenic conditions. The distribution, known as the density of states (DOS), reveals the vibrational characteristics of ice. The calculated DOS resembles that of neutron scattering experiments, as shown in Figure 1 [9,31]. The DOS of the TIP4P/2005 model has two peaks. The modes in the lower frequency region of up to 400 cm^{-1} originate mostly from the translational motions, while the modes between 500 and 1000 cm^{-1} are associated mostly with the rotational (librational) motions. The frequency range of mW ice is limited to 250 cm^{-1} because all of the modes arise from the translational motions. The calculated DOS for TIP4P/2005 ice reproduces the overall feature of the experimental DOS. There are two distinct peaks in the low frequency region in both experimental and TIP4P/2005 ice. The DOSs in the rotation-dominant region agree roughly with each other. The mW model also has two distinct peaks in the low frequency region. The peak position of the higher one is fairly different from either of the other two. However, the position of the lower peak agrees with that of the TIP4P/2005 ice model and of the experimental one. Since the modes in this low frequency region, which corresponds to the O-O-O bending, play a central role in giving rise to a negative thermal expansivity [6], the mW model or its variants could reproduce the negative thermal expansivity.

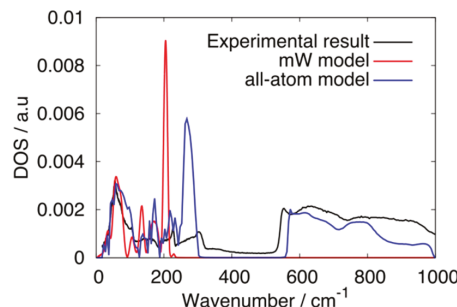


Figure 1. Densities of state of ice Ic calculated with the mW model ($\lambda = 23.15$) and that of the all-atom model. The experimental neutron scattering data for ice Ih is also shown [31].

Although the mW model was developed for ice I, we attempt to use this model for other ice phases. The thermodynamic potential, $A + pV$, is plotted against the molar volume for several ice phases in Figure 2. The equilibrium molar volume, $\langle V \rangle$, is the volume at which the thermodynamic potential is minimized. The equilibrium molar volume is reasonably obtained for ice Ic, Ih, II, and III. The curves of ices II and III reside totally inside the parabola of ice I, meaning that they cannot be the most stable phase at atmospheric pressure. When we elevate the pressure to 300 MPa, ice II and III can

be stable relative to ice Ih with the mW model. We fail to obtain a smooth curve of the thermodynamic potential for ice VI. Probably, the deviation from the perfect tetrahedral coordination is too large to describe this ice structure through the mW model. The octahedral coordination of ice VII is also out of the applicable range of the force field model. The octahedral coordination does not mean that there are eight strong bonds for a molecule. It is impossible to distinguish four hydrogen bonding molecules out of the eight neighbors in the mW model because of the absence of the hydrogen atoms. Another limitation is that the mW model cannot describe the difference between hydrogen-disordered ice and its hydrogen-ordered counterpart. Thus, there is no way to distinguish, for example, ice Ih from ice XI.

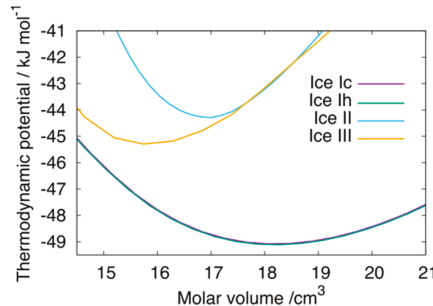


Figure 2. Thermodynamics potential, $A + pV$, for several ice structures at $T = 20$ K, obtained with the mW model. The curve for ice Ic overlaps completely with that of ice Ih.

The thermodynamic potential of Ic is the same as that of Ih for the mW model in the framework of the harmonic approximation, although Ih is slightly more stable than Ic experimentally. Because the interaction range is limited to the nearest four neighbors and they form an ideal tetrahedral arrangement both in ice Ih and Ic, no difference between them is expected for U_q at a fixed density. No practical difference in the vibrational free energy is found. The free energy from the anharmonic vibrations may give rise to the difference at high temperatures. Hereafter, we will not concern ourselves with the stability difference and will examine only ice Ic.

The equilibrium molar volume for ice Ic is plotted in Figure 3 as a function of temperature. It is evident that the thermal expansivity at low temperatures cannot be reproduced using the original mW model ($\lambda = 23.15$). In addition, the molar volume of $18.19 \text{ cm}^3 \text{ mol}^{-1}$ is much smaller than the experimental value [3]. Figure 3 shows the volumes calculated with different λ values. We find that the negative thermal expansivity is successfully reproduced when the λ value is small enough, though only qualitatively.

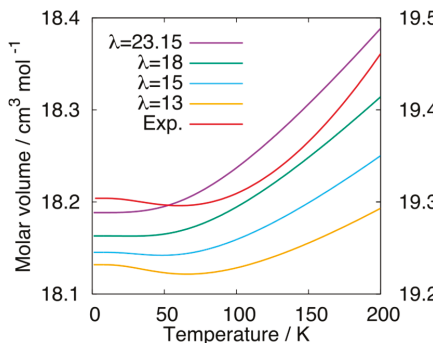


Figure 3. Molar volume of ice Ic as a function of temperature for the mW model, calculated with several λ values. The molar volume of ice Ih from the experimental data is also shown (red, right axis) [3].

The equilibrium volume depends substantially on the tetrahedrality parameter, λ . A smaller λ makes the hydrogen bond network more flexible and leads to a more compact packing, while the tetrahedral coordination remains. As shown in Figure 4, the peaks in the DOS shift to a lower frequency as a result of the increase in flexibility due to the decrease in λ from 23.15 to 13. Figure 5 plots the thermal expansivity against the temperature. The critical λ value to recover the negative thermal expansivity lies around 18.

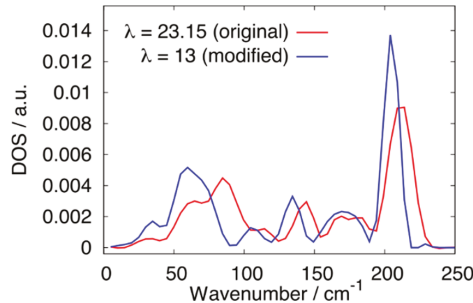


Figure 4. DOSs for ice Ic of the mW model with the original and modified λ values.

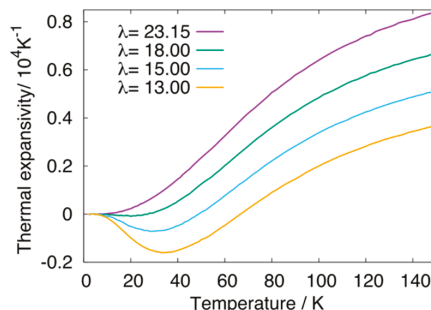


Figure 5. Thermal expansivities of ice Ic calculated using the mW model with $\lambda = 23.15$ (purple line), 18.00 (green line), 15.00 (cyan line), and 13.00 (yellow line).

4. Discussion

We calculate the temperature dependence of the molar volume for both the TIP4P/2005 model and the mW model. The purple curve in Figure 6 is the molar volume of ice Ic plotted against the temperature calculated with the all-atom TIP4P/2005 model. The value of $20.05 \text{ cm}^3 \text{ mol}^{-1}$ is close to the experimental value for ice Ih, $19.3 \text{ cm}^3 \text{ mol}^{-1}$ [3]. Figure 7 shows the thermal expansivity. The thermal expansivity of the TIP4P/2005 model is negative below 60 K, which is in agreement with the experimental result. We examine the effect of the coupling between the rotational and translational modes on the volume and its temperature dependence. The Hessian matrix, \mathbf{K} , can be expressed as:

$$\mathbf{K} = \begin{pmatrix} \mathbf{K}_{tt} & \mathbf{K}_{tr} \\ \mathbf{K}_{rt} & \mathbf{K}_{rr} \end{pmatrix}, \quad (8)$$

where t and r denote the translational and rotational components, respectively. We obtain a matrix \mathbf{K}_b by removing the rotational-translational coupling elements, \mathbf{K}_{tr} and \mathbf{K}_{rt} .

$$\mathbf{K}_b = \begin{pmatrix} \mathbf{K}_{tt} & 0 \\ 0 & \mathbf{K}_{rr} \end{pmatrix}, \quad (9)$$

The thermodynamic properties without the rotational-translational coupling are calculated from the mode frequencies obtained by the diagonalization of the matrix \mathbf{K}_b . Figure 6 shows that the volume of ice only slightly increases due to the removal of the coupling. However, the negative thermal expansivity disappears completely, as shown in Figure 7. It is also possible to eliminate the contributions from the rotational modes, as well as those from the rotational-translational coupling, by removing \mathbf{K}_{rr} in Equation (9). The volume calculated only from the translational motion is $19.38 \text{ cm}^3 \text{ mol}^{-1}$, much smaller than the original value of the TIP4P/2005 model, $20.05 \text{ cm}^3 \text{ mol}^{-1}$. Notwithstanding this, both the mW model and the TIP4P family reproduce the volume of liquid water fairly well [16], although there is a large discrepancy in the volume of ice I. The underestimation of the volume for the mW model may originate from the absence of the rotational modes. The shift to a higher frequency side upon compression in the TIP4P/2005 model is observed for the modes associated with the rotational motions, which is not shown but is a normal behavior against pressurization. This causes a decrease in the volume.

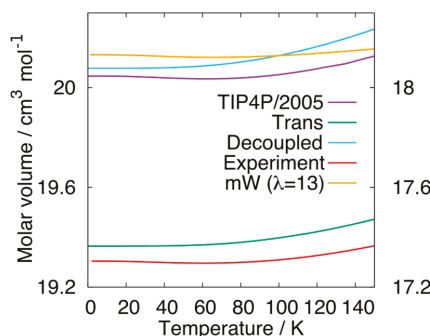


Figure 6. Molar volume of ice Ic plotted against the temperature for the TIP4P/2005 model (purple), that calculated without the rotational-translational coupling (cyan), and that calculated only with the translational modes (green). The red curve is the volume of ice Ih from the experimental data. The volume of the mW model with $\lambda = 13$ is also shown (yellow, right axis).

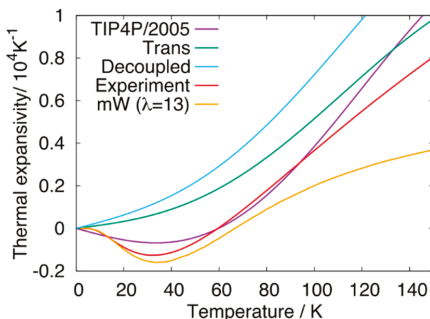


Figure 7. Thermal expansivity of ice Ic plotted against the temperature for the TIP4P/2005 model (purple), that calculated without the rotational-translational coupling (cyan), and that calculated only with the translational modes (green). The red curve is the thermal expansivity from the experimental data [3]. The thermal expansivity of the mW model with $\lambda = 13$ is also shown (yellow).

The thermal expansivity, α , can be expressed as:

$$\alpha = \frac{\gamma C_v k_T}{3V}, \quad (10)$$

where γ is the Grüneisen parameter, C_v is the heat capacity, and κ_T is the isothermal compressibility. The Grüneisen parameter is expressed as:

$$\gamma = \sum_i \gamma_i C_i / \sum_i C_i , \quad (11)$$

where γ_i and C_i are the Grüneisen parameter and heat capacity for the i -th mode, respectively. The mode Grüneisen parameter of the i -th mode is defined as:

$$\gamma_i = -\left(\frac{\partial \ln \nu_i}{\partial \ln V}\right). \quad (12)$$

The heat capacity of a mode is given by:

$$C_i = k_B \left(\frac{h\nu_i}{k_B T} \right)^2 \left[\exp\left(\frac{h\nu_i}{k_B T}\right) - 1 \right]^{-2}. \quad (13)$$

Figure 8 shows the frequency dependence of the heat capacities of the vibrational modes defined as:

$$c(\nu) = \int_{\nu}^{\nu + \Delta\nu} \sum_i \delta(\nu' - \nu) C_i d\nu', \quad (14)$$

for the mW model with $\lambda = 13$ at three different temperatures. The heat capacity is almost zero for modes with frequencies higher than 80 cm^{-1} at $T = 20 \text{ K}$, reflecting the fact that only very low-frequency modes can be thermally excited at such a low temperature.

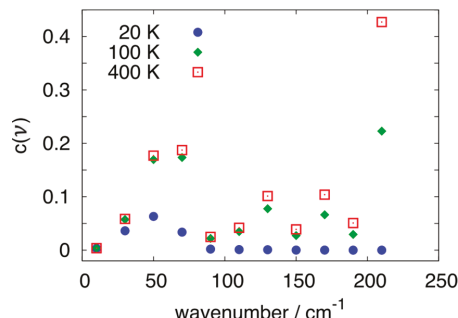


Figure 8. Frequency dependence of the heat capacity of modes at temperatures 20 K (blue circle), 100 K (green diamond), and 400 K (red open square) for the mW model with $\lambda = 13$.

The mode Grüneisen parameter is calculated as follows. First, the mass-weighted Hessian matrix at the equilibrium volume, \mathbf{K}_0 , is diagonalized as:

$$\Lambda_0 = \mathbf{U}_0^\dagger \mathbf{K}_0 \mathbf{U}_0, \quad (15)$$

where Λ_0 is the diagonalized matrix and \mathbf{U}_0 is the unitary matrix that diagonalizes \mathbf{K}_0 . Next, the volume of the system is scaled isotropically by a factor of 1.0015, and the mass-weighted Hessian for the expanded system, \mathbf{K}_e , is calculated. Similarly, the original system is scaled by 0.9985, and the mass-weighted Hessian for the shrunken system, \mathbf{K}_s , is calculated. The mode frequencies of the expanded and the shrunken systems are calculated with the unitary matrix for the original volume:

$$\Lambda_e = \mathbf{U}_0^\dagger \mathbf{K}_e \mathbf{U}_0, \quad (16)$$

and

$$\Lambda_s = \mathbf{U}_0^\dagger \mathbf{K}_s \mathbf{U}_0. \quad (17)$$

The differential value, γ_i , is numerically calculated from Λ_e and Λ_s . Figure 9 shows the frequency dependence of the product $\gamma_i C_i$ for the mW model with $\lambda = 13$. The γ_i value is negative for the O-O-O bending modes around 50 cm^{-1} . When the temperature is low enough, only this part contributes to the γ defined in Equation (11). At higher temperatures, the positive contributions from the high frequency O-O stretching modes become dominant because of the increase in C_i . Therefore, the negative thermal expansivity is observed only at low temperatures. A similar result was reported for the TIP4P model [6].

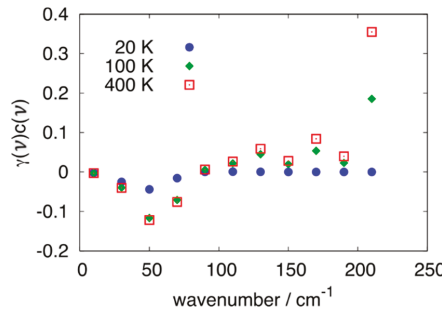


Figure 9. Frequency dependence of $\gamma_i C_i$ at temperatures 20 K (blue circle), 100 K (green diamond), and 400 K (red open square) for the mW model with $\lambda = 13$.

As shown in Figure 5, the negative thermal expansivity is found for the mW model when the λ parameter is small enough. Figure 10 presents the frequency dependence of γ_i . The mode Grüneisen parameters are positive even in the region around 50 cm^{-1} for the original λ value of 23.15. This is probably because the modes around 50 cm^{-1} with the original λ value have a lower O-O-O bending character. However, a decrease in the λ value can loosen the geometrical restriction of the arrangement on the three neighboring molecules and give rise to rather lower frequency modes, which may have the bending character.

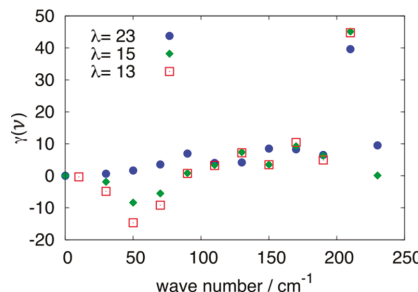


Figure 10. Frequency dependence of the mode Grüneisen parameter for the original λ (blue circle), $\lambda = 15$ (green diamond), and $\lambda = 13$ (red open square).

5. Conclusions

We have calculated the chemical potential and volumetric properties of ice polymorphs with the original mW potential, applying the quasi-harmonic approximation. It is found that only several low-pressure ices (Ih, Ic, II, and III) are stable or metastable with the original mW model. The original mW model does not reproduce the negative thermal expansivity at low temperatures for ice I. A revision is proposed so as to recover the negative thermal expansivity. It is achieved by reducing one of the

parameters of the force field model, λ , which was introduced for three molecules to favor the angle of the ideal tetrahedral arrangement, 109.47° . The origin of the negative thermal expansivity is examined for the revised mW model in terms of the anomalous mode Grüneisen parameters. In particular, the dependence of the mode Grüneisen parameters on the λ value is closely scrutinized. The magnitude of the negative mode Grüneisen parameters generally increases with decreasing λ value.

The calculated thermodynamic properties for mW ice are compared with those of a more realistic model, TIP4P/2005. The origin of the difference in the thermal expansivity is investigated by the chemical potential, whose vibrational free energy part is calculated from the block diagonal matrix in which all off-diagonal elements associated with translational-rotational degrees of freedom are removed. This decoupling of the translational and rotational motions eliminates the anomaly in the thermal expansivity and seems to be related to the observation that the negative thermal expansivity is not recovered with the original mW potential. The rotational degree of freedom may help to absorb the bare collisional motion between two adjacent oxygens through tight hydrogen bonding. The decrease in the λ value in mW, which loosens the geometrical restriction of the arrangement on the three neighboring molecules, seems to have a similar effect.

Author Contributions: M.M.H. performed the simulations and calculations, prepared the data, and wrote the paper; T.Y. co-wrote the paper; M.M. prepared the ice structures and revised the paper; H.T. conducted the project, wrote the programs for normal mode analysis, co-wrote and revised the paper.

Funding: This research was funded by JSPS KAKENHI grant number 17K19106 and MEXT as “Priority Issue on Post-Kcomputer” (Development of new fundamental technologies for high-efficiency energy creation, conversion/storage and use).

Conflicts of Interest: The authors declare no conflict of interest.

References

- Dantl, G. Wärmeausdehnung von H_2O - und D_2O -Einkristallen. *Zeitschrift für Physik* **1962**, *166*, 115–118. [[CrossRef](#)]
- Röttger, K.; Endriss, A.; Ihringer, J.; Doyle, S.; Kuhs, W.F. Lattice constants and thermal expansion of H_2O and D_2O ice Ih between 10 and 265 K. Addendum. *Acta Crystallogr. B* **2012**, *68*, 91. [[CrossRef](#)]
- Fortes, A.D. Accurate and precise lattice parameters of H_2O and D_2O ice Ih between 1.6 and 270 K from high-resolution time-of-flight neutron powder diffraction data. *Acta Cryst.* **2018**, *B74*, 196–216.
- Buckingham, D.T.W.; Neumeier, J.J.; Masunaga, S.H.; Yu, Y.K. Thermal Expansion of Single-Crystal H_2O and D_2O Ice Ih. *Phys. Rev. Lett.* **2018**, *121*, 185505. [[CrossRef](#)]
- Fortes, A.D. Structural manifestation of partial proton ordering and defect mobility in ice Ih. *Phys. Chem. Chem. Phys.* **2019**, *21*, 8264–8474. [[CrossRef](#)]
- Tanaka, H. Thermodynamic stability and negative thermal expansion of hexagonal and cubic ices. *J. Chem. Phys.* **1998**, *108*, 4887–4893. [[CrossRef](#)]
- Grüneisen, E. Theorie des festen Zustandes einatomiger Elemente. *Annalen der Physik* **1912**, *344*, 257–306. [[CrossRef](#)]
- Nakamura, T.; Matsumoto, M.; Yagasaki, T.; Tanaka, H. Thermodynamic Stability of Ice II and Its Hydrogen-Disordered Counterpart: Role of Zero-Point Energy. *J. Phys. Chem. B* **2016**, *120*, 1843–1848. [[CrossRef](#)]
- Petrenko, V.F.; Whitworth, R.W. *Physics of Ice*; Oxford University Press: Oxford, UK, 1999.
- Grimme, S. Semiempirical GGA-type density functional constructed with a long-range dispersion correction. *J. Comput. Chem.* **2006**, *27*, 1787–1799. [[CrossRef](#)]
- Pamuk, B.; Soler, J.M.; Ramírez, R.; Herrero, C.P.; Stephens, P.W.; Allen, P.B.; Fernández-Serra, M.-V. Anomalous Nuclear Quantum Effects in Ice. *Phys. Rev. Lett.* **2012**, *108*, 193003. [[CrossRef](#)] [[PubMed](#)]
- Salim, M.A.; Willow, S.Y.; Hirata, S. Ice Ih anomalies: Thermal contraction, anomalous volume isotope effect, and pressure-induced amorphization. *J. Chem. Phys.* **2016**, *144*, 204503. [[CrossRef](#)]
- Gupta, M.K.; Mittal, R.; Singh, B.; Mishra, S.K.; Adroja, D.T.; Fortes, A.D.; Chaplot, S.L. Phonons and anomalous thermal expansion behavior of H_2O and D_2O ice Ih. *Phys. Rev. B* **2018**, *98*, 104301. [[CrossRef](#)]

14. McKinley, J.L.; Beran, G.J.O. Identifying pragmatic quasi-harmonic electronic structure approaches for modeling molecular crystal thermal expansion. *Faraday Discuss.* **2018**, *211*, 181–207. [[CrossRef](#)]
15. Abascal, J.L.F.; Vega, C. A general purpose model for the condensed phases of water: TIP4P/2005. *J. Chem. Phys.* **2005**, *123*, 234505. [[CrossRef](#)]
16. Sanz, E.; Vega, C.; Abascal, J.L.F.; MacDowell, L.G. Phase Diagram of Water from Computer Simulation. *Phys. Rev. Lett.* **2004**, *92*, 255701. [[CrossRef](#)] [[PubMed](#)]
17. Aragones, J.L.; Vega, C. Plastic crystal phases of simple water models. *J. Chem. Phys.* **2009**, *130*, 244504. [[CrossRef](#)] [[PubMed](#)]
18. Hirata, M.; Yagasaki, T.; Matsumoto, M.; Tanaka, H. Phase Diagram of TIP4P/2005 Water at High Pressure. *Langmuir* **2017**, *33*, 11561–11569. [[CrossRef](#)] [[PubMed](#)]
19. Yagasaki, T.; Matsumoto, M.; Tanaka, H. Phase Diagrams of TIP4P/2005, SPC/E, and TIP5P Water at High Pressure. *J. Phys. Chem. B* **2018**, *122*, 7718–7725. [[CrossRef](#)] [[PubMed](#)]
20. Jorgensen, W.L.; Chandrasekhar, J.; Madura, J.D.; Impey, R.W.; Klein, M.L. Comparison of simple potential functions for simulating liquid water. *J. Chem. Phys.* **1983**, *79*, 926–935. [[CrossRef](#)]
21. Ramírez, R.; Neuerburg, N.; Fernández-Serra, M.-V.; Herrero, C.P. Quasi-harmonic approximation of thermodynamic properties of ice Ih, II, and III. *J. Chem. Phys.* **2012**, *137*, 044502–044513. [[CrossRef](#)]
22. Molinero, V.; Moore, E.B. Water modeled as an intermediate element between carbon and silicon. *J. Phys. Chem. B* **2009**, *113*, 4008–4016. [[CrossRef](#)]
23. Jacobson, L.C.; Hujo, W.; Molinero, V. Nucleation pathways of clathrate hydrates: Effect of guest size and solubility. *J. Phys. Chem. B* **2010**, *114*, 13796–13807. [[CrossRef](#)]
24. Moore, E.B.; Molinero, V. Ice crystallization in water’s “no-man’s land”. *J. Chem. Phys.* **2010**, *132*, 244504. [[CrossRef](#)]
25. Stillinger, F.H.; Weber, T.A. Computer simulation of local order in condensed phases of silicon. *Phys. Rev. B* **1985**, *31*, 5262–5271. [[CrossRef](#)]
26. Laradji, M.; Landau, D.P.; Dünweg, B. Structural properties of $\text{Si}_{1-x}\text{Ge}_x$ alloys: A Monte Carlo simulation with the Stillinger-Weber potential. *Phys. Rev. B Condens. Matter* **1995**, *51*, 4894–4902. [[CrossRef](#)]
27. Takenaka, K. Negative thermal expansion materials: Technological key for control of thermal expansion. *Sci. Technol. Adv. Mater.* **2012**, *13*, 013001. [[CrossRef](#)]
28. Fabian, J.; Allen, P.B. Thermal expansion and Grüneisen parameters of amorphous silicon: A realistic model calculation. *Phys. Rev. Lett.* **1997**, *79*, 1885. [[CrossRef](#)]
29. Moore, E.B.; Molinero, V. Structural transformation in supercooled water controls the crystallization rate of ice. *Nature* **2011**, *479*, 506–508. [[CrossRef](#)]
30. Matsumoto, M.; Yagasaki, T.; Tanaka, H. GenIce: Hydrogen-Disordered Ice Generator. *J. Comput. Chem.* **2018**, *39*, 61–64. [[CrossRef](#)]
31. Li, J. Inelastic neutron scattering studies of hydrogen bonding in ices. *J. Chem. Phys.* **1996**, *105*, 6733–6755. [[CrossRef](#)]



© 2019 by the authors. Licensee MDPI, Basel, Switzerland. This article is an open access article distributed under the terms and conditions of the Creative Commons Attribution (CC BY) license (<http://creativecommons.org/licenses/by/4.0/>).

Article

Decomposition Characterizations of Methane Hydrate Confined inside Nanoscale Pores of Silica Gel below 273.15 K

Lihua Wan ^{*}, Xuebing Zhou, Peili Chen, Xiaoya Zang, Deqing Liang and Jinan Guan

Key Laboratory of Gas Hydrate, Guangzhou Institute of Energy Conversion, Chinese Academy of Sciences, Guangzhou 510640, China; zhoubx@ms.giec.ac.cn (X.Z.); chenpl@ms.giec.ac.cn (P.C.); zangxy@ms.giec.ac.cn (X.Z.); liangdq@ms.giec.ac.cn (D.L.); guanja@ms.giec.ac.cn (J.G.)

* Correspondence: wanlh@ms.giec.ac.cn; Tel.: +86-20-8705-7669

Received: 7 March 2019; Accepted: 8 April 2019; Published: 10 April 2019

Abstract: The formation and decomposition of gas hydrates in nanoscale sediments can simulate the accumulation and mining process of hydrates. This paper investigates the Raman spectra of water confined inside the nanoscale pores of silica gel, the decomposition characterizations of methane hydrate that formed from the pore water, and the intrinsic relationship between them. The results show that pore water has stronger hydrogen bonds between the pore water molecules at both 293 K and 223 K. The structure of pore water is conducive to the nucleation of gas hydrate. Below 273.15 K, the decomposition of methane hydrate formed from pore water was investigated at atmospheric pressure and at a constant volume vessel. We show that the decomposition of methane hydrate is accompanied by a reformation of the hydrate phase: The lower the decomposition temperature, the more times the reformation behavior occurs. The higher pre-decomposition pressure that the silica gel is under before decomposition is more favorable to reformation. Thus, reformation is the main factor in methane hydrate decomposition in nanoscale pores below 273.15 K and is attributed to the structure of pore water. Our results provide experimental data for exploring the control mechanism of hydrate accumulation and mining.

Keywords: gas hydrate; decomposition; reformation; pre-decomposition pressure; nanoscale pores

1. Introduction

Gas hydrates are naturally occurring ice-like crystalline compounds in which the hydrogen-bonded water molecules forming the hydrate lattice interact with the guest molecules with van der Waals forces. The occurrence of gas hydrates is controlled by forming temperature, forming pressure and the availability of appropriate gases and water. Gas hydrates are present in sedimentary deposits in permafrost regions and beneath the sea in outer continental margins. They were first discovered in the permafrost regions of Russia [1] and Canada's Mackenzie Delta [2] and subsequently in sediments of the Caspian Sea and Black Sea [3]. China has an abundance of gas hydrate resources in the South China Sea, the Pearl River Delta, and the Qinghai permafrost regions [4]. Natural gas hydrate is a kind of clean energy, and energy concentrated in natural gas hydrates may be an energy source for much of the 21st century [5].

Natural sediments bearing gas hydrates including coarse-grained and fine-grained sediments such as sands, silts, and clays have a wide distribution of pore size and particle size. Pore size and particle size affect the formation and dissociation behavior of gas hydrates in such sediments. Much work has been carried out on hydrate formation and dissociation with powerful numerical tools and experimental simulation [6–16]. The formation and decomposition of gas hydrates can also cause the pore structure and flow properties to change [14]. X-ray radiography and 3D computed tomography

(CT) have been used to measure xenon hydrate dissociation kinetics in a porous medium (sand) through depressurization at the quasi-isothermal condition. It was found that hydrate surface area controls gas hydrate dissociation kinetics in porous media [15]. The characteristics of methane hydrate formation and dissociation in porous medium with different particle sizes using depressurization have been discussed [16]. Meso-level simulation of gas hydrate dissociation in low-permeability marine sediments was reported [17]. The interactions between gas, water, and hydrates by defining the pores and the fluid flow in the pores using the discrete element model have been described. The microscale effects on methane hydrate dissociation in the micro porous media channels including the microscale effects on the multiphase flow behavior as well as the mass and heat transfer between phases have been discussed [18–21]. Researchers have long tried to ascertain the equilibrium behavior of gas hydrate formation in porous media with different pore size distributions from the macro scale to the micro scale [22–30]. In addition, marine sediments hosting gas hydrates play an important role in controlling the hydrate stability zone (HSZ) thickness on the seafloor [31–35].

The formation and decomposition of gas hydrates in nanoscale argillaceous silt, nanoscale calcium carbonate, and clay can simulate the accumulation and mining process of hydrates. By studying the mass transfer of these processes, we can explore the control mechanism of hydrate accumulation and mining. Experimental results have shown the relationship between nanoscale pores bearing gas hydrates and dissociation behavior [36–38]. The dissociation conditions of methane hydrates in confined small pores were measured. Significant downward shifts of the dissociation temperature were observed in porous glass [36]. The melting temperature depression and the shifted phase boundaries were monitored [37]. The methane hydrate heat of dissociation into pore water and gas in 7-nm-radius silica gel pores, obtained calorimetrically, was 45.92 kJ/mol [38]. Studies [36–38] have discussed the effect of pore size distributions of fine-grained sediments on the dissociation temperature, phase boundaries of gas hydrates, and the heat of dissociation.

Since the thermodynamics and kinetics of hydrate decomposition in nanoscale pores are very complex, much further investigation is needed. The main purpose of this paper is to investigate the effect of the decomposition temperature and the pre-decomposition pressure on the micro and macro decomposition characterizations of methane hydrate below 273.15 K, which formed from the water confined inside nanoscale pores of the silica gel.

The properties of water inside the nanoscale pores clearly have a significant impact on the formation and dissociation of gas hydrate below 273.15 K. Temperature and the characteristics of the porous media play important roles in the behavior of the water. In fact, in porous media, sometimes some water does not freeze when cooled below 273.15 K [39,40]. The amount of unfrozen water decreases with the lowering of the temperature. The relationship between the reduction in temperature and the amount of unfrozen water was obtained by using the nuclear magnetic resonance (NMR) technique [39]. In addition, liquid water also exists in equilibrium with bulk ice and bulk gas hydrate in hydrophilic porous media [40]. X-ray diffraction measurements were performed to study the freezing and melting behavior of water confined within SBA-15 with a pore radius of 3.9 nm [41]. It was found that the freezing temperature increased continuously with increasing pore filling, and the melting of the frozen pore water took place at 256 K, independent of the level of pore filling. The influence of pore wall hydrophobicity on freezing and melting behavior of the confined water is very small [42].

These results show that nanopores inhibit the formation of ice. However, the influence of the microstructure of nanoporous water on the formation and decomposition of hydrate is still unclear. In addition, the content of unfrozen water has significant impact on physico-chemical and mechanical properties of sediments [43]. Thus, it is necessary to investigate the effect of micro properties of the water confined inside nanoscale pores on the dissociation of methane hydrate. The Raman structure of nanoporous water remains unclear. This paper investigates the Raman spectral structure of water confined inside the nanoscale pores of silica gel, the decomposition characterizations of methane hydrate that formed from the pore water, and their intrinsic relationship.

2. Experimental

2.1. Materials and Experimental Apparatus

Methane hydrate was synthesized from water confined inside silica gel pores. The silica gel used was a synthetic silica gel with a pore diameter range of 15–20 nm, supplied by Qingdao Shuoyuan Co., Ltd., Qingdao, China. The pore size, pore volume, and specific surface area of the silica gel were determined using the ASAP2010 surface and pore size analyzer (Micromeritics, Atlanta, GA, USA). The average pore volume was 1.19 mL/g. The specific surface area was 300–500 m²/g. Methane gas was purchased from Foshan Nanhai Gas Co., Ltd., Foshan, China with a purity of 99.99%. The system diagram of the methane hydrate sample synthesis and decomposition device is shown in Figure 1. The experimental apparatus mainly consisted of a reactor, a thermostatically controlled air bath, a gas injection system, some measurement units, and a data acquisition system. The principal component of the apparatus was a reactor—a pressure vessel immersed in an air bath. The vessel was made of stainless steel (1Cr18Ni9Ti), it had an internal volume of 25 mL and could be operated up to 20 MPa. One resistance thermometer and one pressure transducer were inserted in the vessel (Figure 1) to measure the temperature and pressure profile inside the vessel. A Pt100 thermometer with a range of 223–373 ± 0.1 K was used, and the pressure transducer was model SS2 (Boxborough, MA, USA) with a range of 0–20 MPa ± 0.25%. This hydrate forming system was used to prepare the hydrate samples for microscopic measurements as well as decomposition measurements.

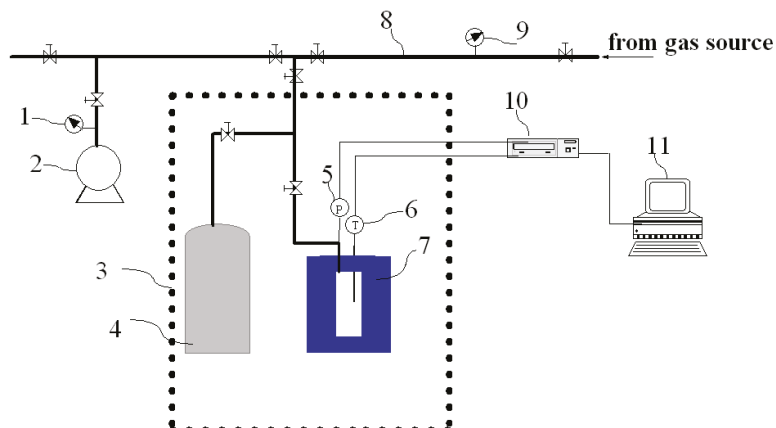


Figure 1. Experimental apparatus. 1, vacuum pressure gauge; 2, vacuum pump; 3, air bath; 4, buffer tank; 5, pressure sensor; 6, platinum resistance temperature sensor; 7, stainless steel reactor; 8, pipeline; 9, pressure gauge; 10, data acquisition instrument; 11, computer.

To obtain microstructural features of water confined inside the pores of silica gel, a micro-laser Raman spectrometer (Horiba, LabRam HR, Paris, France) was used to measure the Raman spectra of water confined inside the pores of silica gel. The spectrometer was equipped with a single monochromator of 600 grooves/mm grating and a multichannel air-cooled charge-coupled device (CCD) detector. An Ar+ laser operating at 532 nm with a maximum power of 50 mW was used. Before the sample was measured, the Raman spectrometer was calibrated with single crystal silicon (520 cm⁻¹). A cooling stage (Linkam BCS) was used to provide a temperature control system for samples. The working parameters of the micro-laser Raman spectrometer are shown in Table 1.

Table 1. Working parameters of the laser Raman spectrometer.

Working Parameters	Setting Conditions
Laser source	532 nm
Laser power	80 mW
Objective lens magnification	×1–100
Grating scale	600 Grooves/mm
Raman shift range	500–4000 cm ^{−1}
Integration time	1–10 s

2.2. Experimental Procedures

2.2.1. Pore Water Confined Inside the Silica Gel Pores

In the experiment, to obtain pore water confined inside the pores of silica gel, the silica gel was first dried at 377.15 K for 24 h, then cooled to room temperature. In the laboratory room, the relative humidity of the air was about 30%. The amount of distilled water equal to the pore volume of the silica gel was thoroughly mixed with the silica gel sample. Then, the sample was placed in a centrifuge at 3500 rpm for 30 min. The sample was sealed and allowed to stand for 5 days to ensure that the distilled water was absorbed in the pores of the silica gel. Samples of pore water with different moisture contents (33%, 67%, and 100%) were prepared.

2.2.2. Raman Spectra of Pore Water

The micro-laser Raman spectrometer was used to obtain the Raman spectra of pore water confined inside the pores of silica gel. Samples of pore water were placed in the sample stages. They were controlled at 293 K and 223 K by the cooling stage for 8 h, and then the Raman structure scanning began. Samples with different moisture contents (33%, 67%, and 100%) were tested.

2.2.3. Hydrate Formation

A 6 g sample of silica gel with 100% water content was added into the reaction vessel, and a vacuum was applied. The reaction vessel was washed by methane gas several times to ensure that there was no air in the reaction vessel. The air bath was set to a temperature of 273.15 K. After the temperature in the vessel and the temperature of the buffer tank were stabilized, the inside of the reaction vessel was pressurized to 11.9 MPa. The pore water confined inside the pores of silica gel was synthesized methane hydrate with methane gas. After about 3 days, the pressure in the reaction vessel was stabilized at about 9.5 MPa, and the synthesis of methane hydrate was complete.

2.2.4. Micro Decomposition of Hydrate

The decomposition of methane hydrate sample confined inside silica gel pores at different temperatures and under atmospheric pressure was tested by Raman spectrometry. Hydrate samples were removed from the reactor and finely ground in liquid nitrogen; finally, they were stored in liquid nitrogen. During the Raman measurement, hydrate samples were shifted to the sample stages precooled at about 193 K. The Raman structure test of the methane hydrate sample was performed at 193 K before the decomposition of the sample started. During the decomposition, the methane hydrate sample was controlled at 263 K, 253 K, and 245 K by the cooling stage. Scanning Raman spectroscopy for one pass took about 4 min. During the decomposition, the Raman spectrometer scanned the sample Raman spectroscopy, and then the next Raman structure scanning began. When the hydrate characteristic Raman peak disappeared, the Raman spectroscopy scanning experiment was complete.

2.2.5. Macro Decomposition of Hydrate

We conducted experiments of decomposition of methane hydrate at a constant volume vessel after dropping the pre-decomposition pressures (9.11 MPa, 2.41 MPa) to atmospheric pressure before

decomposition to investigate the effect of the pre-decomposition pressure of methane hydrate on its decomposition characteristics.

After the methane hydrate sample was synthesized, the pressure of the methane hydrate in the reaction vessel was adjusted by releasing part of the gas, and the pressure was brought to a desired pressure value. Finally, the methane hydrate sample was in a metastable or steady region. After 5 h, the temperature and pre-decomposition pressure in the reaction vessel were stabilized. The gas in the reaction vessel was released so that the instantaneous pressure in the vessel was atmospheric pressure, and the gas valve was immediately closed. Consequently, the methane hydrate sample began to decompose in the reaction vessel.

3. Results and Discussion

3.1. Raman Spectra of Pore Water

In general, the Raman spectra of O-H vibrations in liquid water under ambient condition have been assigned as a bending vibration peak located at $\sim 1640\text{ cm}^{-1}$ and a stretching vibration peak at $2800\text{--}3800\text{ cm}^{-1}$. The Raman O-H stretching bands can be classified as four or five Gaussian peaks with different donor (D) and acceptor (A) hydrogen bonds. The corresponding structures (local hydrogen bond network structure of water molecules) are DAA (single donor–double acceptor), DDAA (double donor–double acceptor), DA (single donor–single acceptor), DDA (double donor–single acceptor), and free O-H structure [44,45]. Of these, DDAA and DA are sensitive to temperature change [44]; within a certain temperature range, as the temperature decreases, DA is partially converted into DDAA [44].

Raman O-H stretching bands of pore water samples and free water are shown in Figure 2. The Raman shifts corresponding to the stretching vibration peaks of the pore water with a water content of 100% are shown in Table 2. For convenience of comparison, the values from the literature [44,45] are also listed in Table 2. In the Raman spectrum of pore water confined inside silica gel pores with a water content of 100% at 293 K, the DDAA and DA are 3087 cm^{-1} and 3288 cm^{-1} , shifting towards lower wave numbers compared with the DDAA and DA structures of free water at 293 K. The bending vibration peak of free water at 293 K appears near 1640 cm^{-1} . The O-H bending vibration peak of pore water is located at 1587 cm^{-1} , shifting to a lower wave number compared with free water at 293 K. Accordingly, it can be seen that the attraction between the pore water molecules confined inside the nanoscale pores increases, which weakens the effect of the O-H chemical bond. Strong hydrogen bonds between water molecules change the physico-chemical properties of the water confined inside the pores of silica gel.

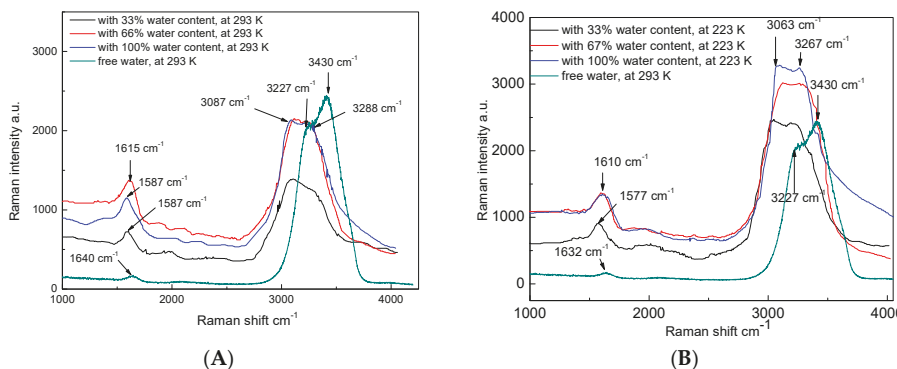


Figure 2. Raman spectra of pore water.

Table 2. Raman shift of DDAA (double donor–double acceptor) and DA (single donor–single acceptor) in pore water with 100% pore filling.

Temperature (K)	DDAA	DA	Reference
293	3220	3430	Water [44]
276	3223	3434	Water [45]
293	3231	3441	Water [45]
298	3227	3430	Water [This work]
293	3087	3288	Pore water [This work]
223	3063	3267	Pore water [This work]

At 293 K, DDAA and DA of pore water account for more than 90% of the Raman stretching spectrum. Compared with free water at 293 K, the Gaussian peak of DDAA in the pore water is clearly enhanced, while that of DA in the pore water is weakened; from this relationship, we see that DA is partially converted into DDAA in the pore water. Compared with DA, the formation of DDAA hydrogen bonding results in lower density, lower entropy, and higher enthalpy [44]. Therefore, pore water has a lower density, lower entropy, and higher enthalpy than free water under ambient conditions. With water contents of 33% and 67%, the Raman spectra of pore water exhibit Raman spectral characteristics similar to those with water content of 100%. At 293 K, the Raman spectral characteristics of pore water are independent of the levels of pore filling.

In pore water with water content of 100% at 223 K, DDAA and DA account for more than 90% of the Raman stretching spectrum. The Raman spectra of pore water maintain a structure similar to those of pore water at 293 K, but the Gaussian peaks shift to lower wave numbers. This result indicates that the pore water at 223 K is still liquid water, and the attraction between the pore water molecules is increased. Solid ice is not found. With water contents of 33% and 67%, the Raman spectra of pore water exhibit Raman spectral characteristics similar to those in the pores with water content of 100% at 223 K. It is thus shown that pore water exists in a unique structure independent of the levels of pore filling.

The Raman spectra of pore water are somewhat similar to those of super-cooled water, albeit with Gaussian peaks shifted to lower wave numbers compared with super-cooled water. Consequently, pore water has stronger hydrogen bonds between the pore water molecules and longer O–H chemical bonds than that of the pore water molecules. In the absence of impurities, the homogeneous nucleation of small ice nuclei requires the surmounting of a free-energy barrier. However, stronger hydrogen bonds between the pore water molecules enlarge the energy barrier. In fact, the pore water at 223 K may still be liquid. Therefore, nanopores can be potentially used as an inhibitor of ice formation. Both neutron diffraction and NMR relaxation measurements have shown similar depressed freezing and melting points of water/ice in mesoporous SBA-15 silica with ordered structures of cylindrical mesopores with a pore diameter 8.6 nm [46].

In liquid water, a water molecule interacts with neighbouring water molecules through various local hydrogen bonds. In pore water, DDAA and DA are the predominant hydrogen bonding networks and the hydrogen bonding networks of DDAA of the pore water are enlarged. In the structure I of gas hydrate, each water molecule is tetrahedrally surrounded by four neighbours through hydrogen bonds. This raises the probability that the water molecule will be trapped in a tetrahedral hydrogen bond network structure composed of water molecules. Therefore, the unique structure of pore water is very conducive to the nucleation of gas hydrate. Nanopores can also be potentially used as a promoter of gas hydrate formation.

3.2. Micro Decomposition of Hydrate

Figure 3 shows the Raman spectrum of methane hydrate during the decomposition process at 263 K and under atmospheric pressure. We can see the characteristic peak of the C–H Raman vibration spectrum of a methane molecule at 2905 cm^{-1} and 2915 cm^{-1} , respectively [47,48], which reflects the different vibration of C–H of the methane molecule in cage $5^{12}6^2$ and cage 5^{12} . It shows that

the structure of the CH₄ hydrates formed in porous silica gels is the same as that of the bulk CH₄ hydrate (structure I) without structure transition. From ¹³C NMR results in the literature, it can also be concluded that the structure of CH₄ hydrates formed in porous silica gels (6.0, 15.0, and 30.0 nm) is the same as that of the bulk CH₄ hydrate (structure I) without structure transition [26].

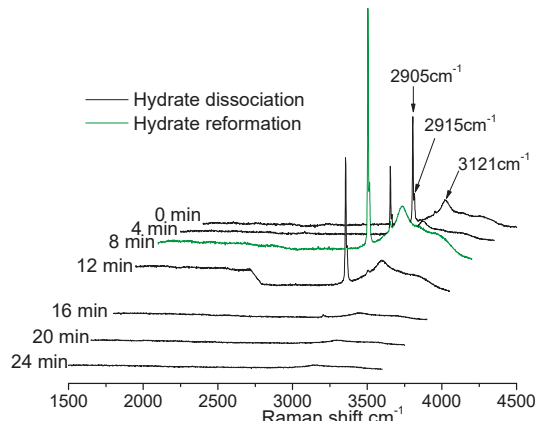


Figure 3. Methane hydrate decomposition at 263 K and atmospheric pressure.

The characteristic Raman peak of the O–H bond of the large-sized methane hydrate appears at about 3076 cm⁻¹ [48]. The characteristic Raman peak of the O–H bond of the methane hydrate formed inside the silica nanoscale pores appears at 3121 cm⁻¹, shifting to a higher wave number in contrast to the large-sized methane hydrate. This reflects the change in the lattice parameters of the methane hydrate formed inside the nanoscale pores. From this, it can be judged that the synthesized sample is a structure I methane hydrate crystal.

After 4 min of decomposition, in contrast to the initial moment (0 min), the Raman intensities of the C–H bond at 2905 cm⁻¹ and 2915 cm⁻¹ decrease and the Raman peak of the O–H bond of the water molecule is synchronously weakened. This indicates that the methane hydrate sample is decomposing. After 8 min, the intensities of the C–H spectrum increase at both 2905 cm⁻¹ and 2915 cm⁻¹, and the Raman peak of the O–H bond of the water molecule increases synchronously, indicating that methane hydrate is reforming. At 8 min, the peak intensity is higher than that at 0 min. At the same time, the peak intensity of the O–H bond is higher than that at 0 min, illustrating that the total amount of methane hydrate is higher than the initial amount. It is inferred that the new methane hydrate phase is derived not only from the reformation reaction of the water originating from the decomposition but also from the reformation of the water residual from the sample synthesis reaction. It is assumed that the residual water is completely converted into hydrate during the reformation, and the conversion rate of pore water in the synthesis of the sample is estimated to be about 53.9%. After 12 min, the peak intensities of the C–H spectrum at 2905 cm⁻¹ and 2915 cm⁻¹ decrease and the Raman peak of the O–H bond of the water molecule decreases synchronously, compared with the results after 8 min. This indicates that the methane hydrate is continuing to decompose. Then, the Raman peaks of the C–H and O–H bonds continue to decrease until they disappear, demonstrating that the methane hydrate decomposes until the methane hydrate crystal disappears. Throughout the process, methane hydrate undergoes decomposition–reformation–continuing decomposition until the crystal disappears without ice peaks without self-preservation [49–51].

Figure 4 shows the Raman spectra of methane hydrate during decomposition at 253 K and atmospheric pressure. After 4 min, the Raman peak intensities of the O–H and C–H bonds are simultaneously weakened relative to 0 min, indicating that the methane hydrate sample is decomposing. After 8 min, the Raman peaks of the O–H and C–H bonds increase synchronously,

indicating that methane hydrate is reforming, and the peak intensity is higher than the 0 min peak intensity. The newly formed methane hydrate is derived not only from the reformation reaction of the water formed by the decomposition but also from the reformation of the water that is residual from the sample formation. Then, the Raman peaks of the C–H and O–H bonds are weakened synchronously until the Raman peaks disappear after 32 min, indicating the decomposition process of the methane hydrate at this stage. After 36 min, the Raman peaks of the C–H and O–H bonds are enhanced, indicating that the hydrate is reforming. Only a very small amount of methane hydrate forms, possibly due to insufficient pressure in the pores of the silica gel. Thereafter, the methane hydrate decomposes until the methane hydrate crystal disappears. Throughout, methane hydrate undergoes a process of decomposition–reformation–continuing decomposition–reformation–decomposition. Until the Raman peak of the C–H bond disappears, the O–H bond Raman peak remains strong, indicating that even if the methane hydrate crystal disappears, a large amount of hydrate cage structure remains [52,53]. There is no ice peak in the whole process and there is no self-preservation effect.

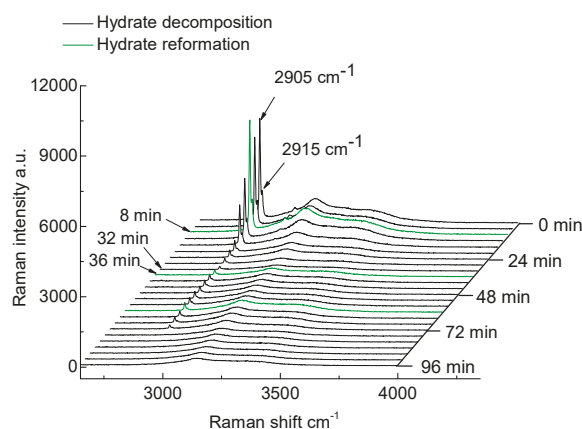


Figure 4. Methane hydrate decomposition at 253 K and atmospheric pressure.

Figure 5 shows the Raman spectra of the decomposition of methane hydrate at 245 K and under atmospheric pressure. During the whole decomposition process, multiple reformation processes occur. This decomposition takes longer than at 253 K or 263 K under atmospheric pressure. It can be seen that the lower is the temperature, the more favourable it is for reformation. There is no ice peak in the whole process. At the end of the entire decomposition process, a large amount of hydrated cage structure remains.

Temperature has an important influence on the hydrogen bond structure of the local network of water molecules after the decomposition. Figure 6 shows the Raman peak of the O–H bond of water molecules at the end of the decomposition. Methane hydrate decomposes into methane gas and a broken cage structure. The methane gas slowly resolves from the nanoscale pores. The lower is the decomposition temperature, the more intact is the cage structure that remains.

There is insufficient time for methane gas to overflow from the pores of silica gel during the decomposition of methane hydrate (see Section 3.3). Thereby, methane gas generated from decomposition enhances the pressure in the pores of silica gel. The structure of pore water is very conducive to the nucleation of gas hydrate and is not conducive to the nucleation of ice (see Section 3.1). When the pressure exceeds the equilibrium pressure of the phase, the formation reaction begins, resulting in the phenomenon of reformation of the hydrate phase. The lower is the temperature, the lower will be the phase equilibrium pressure, and the more times the reformation phenomenon occurs, the longer the process of decomposition will take. The final product during the decomposition of methane hydrate is a broken hydrated cage structure. The low temperature is favourable for the

existence of the hydrated cage structure below 273.15 K. Thus, reformation is the main factor in methane hydrate decomposition in the nanoscale pores of silica gel below 273.15 K at atmospheric pressure, and the controlling factor causing reformation is the temperature.

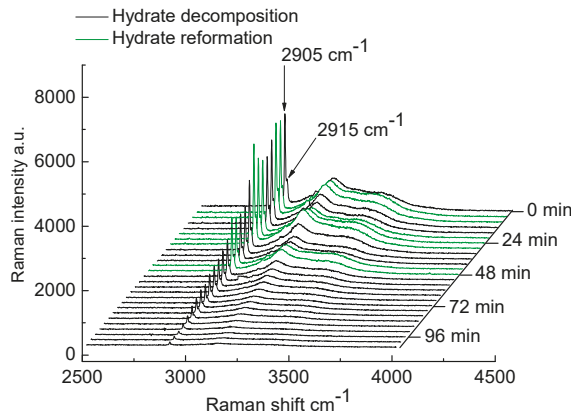


Figure 5. Methane hydrate decomposition at 245 K and atmospheric pressure.

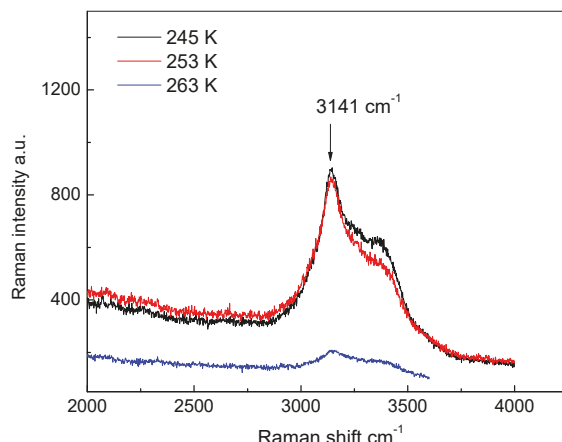


Figure 6. Raman peak of the O–H bond of water molecules after the end of decomposition.

Figure 7 shows the favourable cavity occupancy curve of methane hydrate during the decomposition process at 263 K, 253 K, and 245 K, and under atmospheric pressure. The calculation method is based on [54–56]. Figure 7 indicates that there is a weaker sensitivity on the large cavity occupancy, and a relatively stronger sensitivity on the small cavity occupancy and total cavity occupancy. The results are in reasonable agreement with calculations and experimental data [56,57]. The hydrate total cavity occupancy and small cavity occupancy increase after multiple decompositions and reformation.

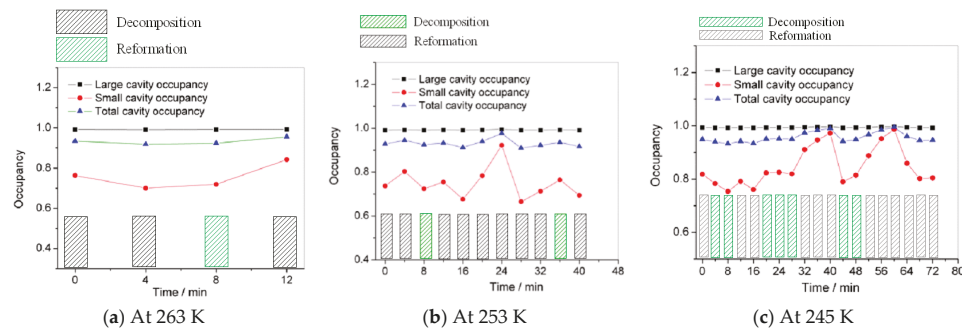


Figure 7. Methane hydrate occupancy curve.

3.3. Macro Decomposition of Hydrate

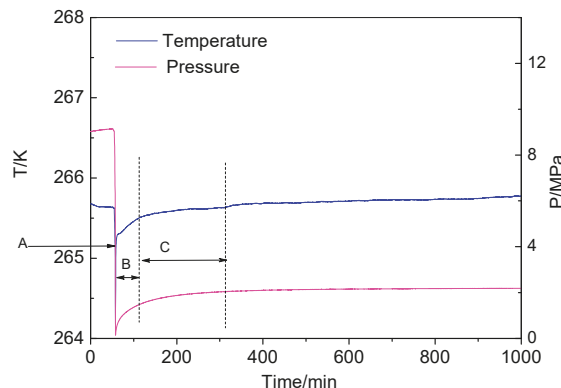
We investigated the effect of the pre-decomposition pressure on decomposition characteristics of methane hydrate at a constant volume vessel. The decomposition conditions and results are shown in Table 3 and Figures 8 and 9.

3.3.1. Decomposition from High Pre-Decomposition Pressure

After methane hydrate was synthesized, the temperature of the vessel was ~ 265.64 K and the pre-decomposition pressure in the vessel was ~ 9.11 MPa. The pre-decomposition pressure in the vessel was instantly reduced to atmospheric pressure. The methane hydrate sample in the pores of silica gel decomposed in the vessel. The decomposition temperature and the pre-decomposition pressure in the vessel during the process are shown in Figure 8. We see that the methane hydrate decomposition process can be roughly divided into the three stages of rapid desorption of gas from the surface of silica gel (stage A), hydrate decomposition (stage B), and internal slow desorption of adsorbed gas from the pores (stage C). When the pressure is released to atmospheric pressure, it is the beginning of stage A. The temperature inside the vessel is greatly reduced due to the throttling effect [58]. The desorption effect of methane gas from the surface of the nanoscale pores causes the pressure inside the vessel to increase rapidly and is accompanied by a rapid rise in temperature caused by the rapid desorption from the surface of the silica gel (stage A). This stage is the process of expansion of free gas. When the temperature curve starts to rise slowly, it is the end of stage A and the beginning of stage B. The decomposition reaction is usually endothermic, as heat is required to break the chemical bonds in the methane hydrate undergoing decomposition. Therefore, at the decomposition stage of methane hydrate, the temperature in the vessel is lower than the initial temperature before decomposition, and the decomposed methane gas is released from the pores of silica gel so that the pressure in the vessel increases. When the temperature curve shows an inflection point, it is the end of stage B and the beginning of stage C. It takes ~ 56 min from start to finish of hydrate decomposition (stage B). Because the water in the pores of silica gel cannot form ice (see Section 3.1), in stage B, methane hydrate in the decomposition process has no self-preservation phenomenon. After the decomposition of methane hydrate is complete, methane gas in the pores of silica gel is released. When the pressure almost no longer increases and the pressure curve shows an inflection point, it is the end of stage C. This desorption process of methane gas from the pores of silica gel takes ~ 149 min. Free methane gas is produced more rapidly in stage A. Adsorbed methane gas is produced considerably more slowly but lasts for a longer period in the final stage. Similar results have been reported for desorption of gas from shale [59].

Table 3. Description of decompositions.

Items	Decomposition Temperature K	Pre-Decomposition Pressure MPa	Stage B Time Consumption min	Stage C Time Consumption min	Total Time Consumption min
Run 1	265.64	9.11	56	149	205
Run 2	265.76	2.41	5	210	215

**Figure 8.** Decomposition from high pre-decomposition pressure.

It can be seen that the desorption process of methane gas (stage C) takes a longer time relative to the decomposition stage (stage B). Figure 8 indicates that there is high pressure in the pores of silica gel over a relatively long period of time. After the desorption (stage C) is complete, the pressure in the vessel is ~2.0 MPa and the pressure in the pores of silica gel is ~2.0 MPa. From Figure 8, we can assume that in the initial stage of desorption (early stage C), the gas pressure in the pores of silica gel exceeds 2.6 MPa; at the initial stage of decomposition (early stage B), the pressure in the pores of silica gel exceeds 3.6 MPa. Therefore, in the initial stage B, the pressure and temperature in the vessel are conducive to the formation of methane hydrate; thus, the decomposition of methane hydrate is accompanied by the reformation of methane hydrate in this initial stage. After reformation, the pressure in the pores decreases, and the methane hydrate in the pores begins to decompose again. The methane gas formed by the decomposition is slowly released so that the methane hydrate in the pores decomposes again after a period of time. The methane gas formed by the decomposition is slowly released. After a period of decomposition, the pressure in the pores rises again, satisfying the condition of formation, and the methane hydrate reforms. Stage B takes ~56 min, and it can be seen that the decomposition of methane hydrate is accompanied by multiple reformations in this stage.

3.3.2. Decomposition from Low Pre-Decomposition Pressure

After the temperature and the pressure were stabilized, part of the gas was released and the pressure in the vessel was lowered to ~2.75 MPa. The temperature of the air bath was adjusted so that the temperature in the vessel was ~265.76 K. After 5 h, the pre-decomposition pressure in the vessel was ~2.41 MPa. All the gas in the vessel was instantly released, and the pre-decomposition pressure in the vessel was instantly reduced to atmospheric pressure. The methane hydrate in the pores of silica gel decomposed in the vessel.

The decomposition temperature and pressure in the decomposition process are shown in Figure 9. Similarly, the methane hydrate decomposition process can be roughly divided into the three stages of rapid desorption of gas from the surface of the silica gel (stage A), hydrate decomposition (stage B), and internal slow desorption of gas from the pores of silica gel (stage C).

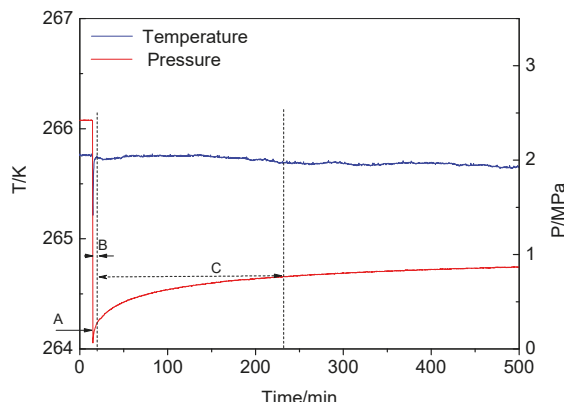


Figure 9. Decomposition from low pre-decomposition pressure.

Since the initial pre-decomposition pressure in the vessel is only 2.41 MPa, the desorption effect from the surface is not strong compared with the desorption effect of stage A in which the methane hydrate drops pressure from 9.11 MPa to atmospheric pressure. Hydrate decomposition takes ~ 5 min from the beginning to the end of the process (stage B). Thus, in stage B, methane hydrate decomposes very rapidly. After the decomposition of methane hydrate, the desorption process of methane gas from the pores of silica gel (stage C) takes ~ 210 min, which is quite a long time compared with stage B. After desorption (stage C) is complete, the pressure in the vessel is ~ 1.0 MPa, and it can be inferred from Figure 8 that the pressure in the pores of silica gel is ~ 1.0 MPa. It is preliminarily estimated that in the initial stage C, the gas pressure in the pores of silica gel exceeds 1.24 MPa, and the pressure in the pores of silica gel in the initial stage B exceeds 1.32 MPa. Therefore, in the initial stage B, there is no condition for hydrate reformation. Since the water in the pores of silica gel cannot form ice (see Section 3.1), there is no self-preservation effect at stage B. Residual water maintains a unique structure.

Therefore, the main factors of methane hydrate decomposition in the nanoscale pores of silica gel below 273.15 K at a constant volume vessel are reformation, and the controlling factor causing reformation is the pre-decomposition pressure of the silica gel before depressurization.

3.4. Mechanism of Hydrate Decomposition

The nano-silica gel particle constituting the silica gel skeleton has a silicon oxytetrahedral structure, and the Si atoms on the surface form a silanol group with the structural water contained in the colloid. In this study, the adsorption of silica gel pores on water molecules was used to obtain pore water confined inside silica gel pores. After the hydrate is formed in the pores of the silica gel, a residual water film remains on the surface of the hydrate (Figure 10). Jung et al. [60] reported similar observations for the methane hydrate reformation in capillary tubes. Hydrate formation in capillary tubes reveals complex formation/dissociation processes.

We can also use the van der Waals–Platteeuw model [54] to explain the methane hydrate reformation phenomenon during the decomposition. According to this model, the dissociation condition of methane hydrates confined in pores shifts because of changes in the water activity, compared with that of the bulk hydrate at a given pressure [28,36,61]. The decrease in dissociation temperature is inversely proportional to the pore size. The hydrate decomposition process is equivalent to the process of increasing the effective pore size (Figure 10), due to the partial methane hydrate crystal transferring into water. Conversely, the hydrate formation process is equivalent to the process of reducing the effective pore size, due to the partial pore water transferring into methane hydrate crystal. Therefore, during the decomposition, the dissociation condition of methane hydrates confined inside the pores of silica gel shifts down (Figure 11). When the temperature

and pressure are in the hydrate phase equilibrium stable region, hydrate reforms. At this time, the effective pore size starts to reduce. Then, the dissociation condition of methane hydrates confined inside the pores shifts up. When the temperature and pressure are under the hydrate phase equilibrium stable region, the hydrate dissociates. Throughout the process, methane hydrate undergoes decomposition–reformation–continuing decomposition until the crystal disappears.

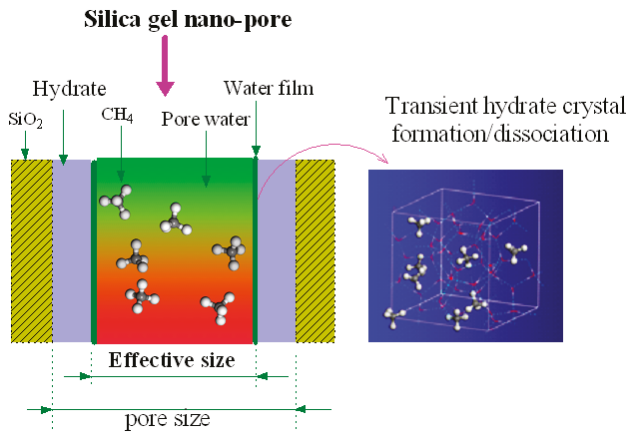


Figure 10. Schematic representation of the methane hydrate formation/dissociation process in nano-silica gel pores.

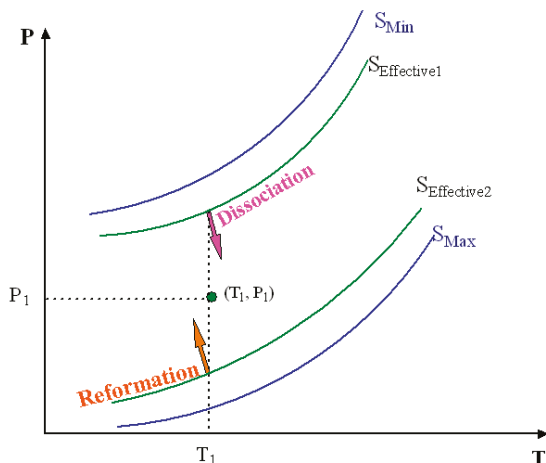


Figure 11. Schematic diagram of methane hydrate dissociation boundary shift in the decomposition process (S_{Min} , S_{Max} , and $S_{\text{Effective}}$ are the min, max, and effective pore size, respectively).

4. Conclusions

This paper investigated the structural characteristics of water confined inside the pores of silica gel with pore diameter range of 15–20 nm and the decomposition characteristics of methane hydrate formed from water confined inside silica pores under atmospheric pressure and at a constant volume vessel.

The micro-laser Raman spectrometer was used to test the Raman spectra of water confined inside the pores of silica gel at 293 K and 223 K. At a temperature of 293 K, the water confined inside the pores of the silica gel is liquid, and its Raman structure is very similar to that of super-cooled water,

compared with which the bending vibration peak and the stretching vibration peak in the water molecules in the pores of silica gel shift towards lower wave numbers. The results show that pore water has stronger hydrogen bonds between the pore water molecules. At 223 K, water in the pores of silica gel is still liquid, and no solid ice forms. The structure of pore water is conducive to the nucleation of gas hydrate and is not conducive to the nucleation of ice. Nanopores can be potentially used as a promoter of gas hydrate formation.

The decomposition of methane hydrate confined inside the pores of silica gel and at atmospheric pressure was tested by Raman spectrometry at 263 K, 253 K, and 245 K. The results show that the decomposition of methane hydrate is accompanied by multiple reformations of the hydrate phase. Throughout the process, methane hydrate undergoes decomposition–reformation–continuing decomposition until the crystal disappears without ice peaks. The lower is the decomposition temperature, the lower is the phase equilibrium pressure, and the more times reformation occurs. The final product is in the form of a broken hydrated cage structure. The lower decomposition temperature is favourable to the existence of the hydrated cage structure.

The effect of the pre-decomposition pressure before the decomposition of methane hydrate on its decomposition characteristics was investigated. The results show that the methane hydrate decomposition process can be roughly divided into the three stages of rapid desorption of gas from the surface (stage A), hydrate decomposition (stage B), and internal slow desorption of gas from the pores (stage C). When the silica gel before decomposition is under high pre-decomposition pressure, the decomposed methane gas remains in the pores for a relatively long time, causing the pressure in the pores to be higher than the phase equilibrium pressure, and a reformation process occurs. The decomposition of methane hydrate is accompanied by multiple reformations. When the pre-decomposition pressure in the silica gel before decomposition is lower, almost no reformation phenomenon is observed.

Thus, the main factor of methane hydrate decomposition in the pores of nanoscale silica gel below 273.15 K is reformation, and the controlling factors causing reformation are the decomposition temperature and the pre-decomposition pressure of the silica gel before depressurization. These experimental characteristics of the decomposition dynamics of methane hydrate confined inside nanoscale pores are attributed to the structure of pore water, which is conducive to the nucleation of gas hydrate and slow desorption of methane gas from the pores of the silica gel. The results of this paper provide experimental data for exploring the control mechanism of hydrate accumulation and mining.

Author Contributions: Data curation, P.C.; Investigation, X.Z. (Xuebing Zhou), X.Z. (Xiaoya Zang), J.G.; Project administration, L.W., D.L.; Writing—original draft, L.W.

Funding: The authors are grateful for financial support from the National Natural Science Foundation of China (NSFC) (51576197, 51106163, 51706230, 51676197), the National Key Research and Development Plan of China (No. 2016YFC0304002), and the Joint Funds of the NSFC from the Government of Guangdong Province (U0933004).

Conflicts of Interest: The authors declare no competing financial interest.

References

1. Makogon, Y.F.; Trebin, F.A.; Trofimuk, A.A.; Tsarev, V.P.; Cherskiy, N.V. Detection of a Pool of Natural Gas in a Solid (Hydrated Gas) State. *Doklady Akademii Nauk SSSR* **1971**, *196*, 203–206.
2. Bily, C.; Dick, J.W.L. Naturally Occurring Gas hydrates in the Mackenzie Delta, NWT. *Bull. Can. Pet. Geol.* **1974**, *22*, 320–352.
3. Yefremova, A.G.; Zhizchenko, B.P. Occurrence of Crystal Hydrates of Gases in the Sediments of Modern Marine Basins. *Doklady Akademii Nauk SSSR* **1974**, *214*, 1179–1181.
4. Wu, N.Y.; Zhang, H.Q.; Yang, S.X.; Liang, J.Q.; Wang, H.B. Preliminary Discussion on Natural Gas Hydrate (NGH) Reservoir System of Shenhua Area, North Slope of South China Sea. *Nat. Gas Ind.* **2007**, *27*, 1.
5. Makogon, Y.F.; Holditch, S.A.; Makogon, T.Y. Natural-gas Hydrates—A Potential Energy Source for the 21st Century. *J. Pet. Sci. Eng.* **2007**, *56*, 14–31. [[CrossRef](#)]

6. Sultan, N.; Cochonat, P.; Foucher, P.J. Effect of Gas Hydrates Melting on Seafloor Slope Instability. *Mar. Geol.* **2004**, *213*, 379–401. [[CrossRef](#)]
7. Park, T.; Kyung, D.; Lee, W. Effect of Organic Matter on CO₂ Hydrate Phase Equilibrium in Phyllosilicate Suspensions. *Environ. Sci. Technol.* **2014**, *48*, 6597–6603. [[CrossRef](#)] [[PubMed](#)]
8. Xu, W.Y.; Germanovich, L.N. Excess Pore Pressure Resulting from Methane Hydrate Dissociation in Marine Sediments: A Theoretical Approach. *J. Geophys. Res. Solid Earth* **2006**, *111*, 1978–2012. [[CrossRef](#)]
9. Kwon, T.H.; Cho, G.C.; Santamarina, J.C. Gas Hydrate Dissociation in Sediments: Pressure-temperature Evolution. *Geochem. Geophys. Geosyst.* **2008**, *9*, Q03019. [[CrossRef](#)]
10. Jain, K.; Juanes, R. Preferential Mode of Gas Invasion in Sediments: Grain-scale Mechanistic Model of Coupled Multiphase Fluid Flow and Sediment Mechanics. *J. Geophys. Res.* **2009**, *114*, B08101. [[CrossRef](#)]
11. Holtzman, R.; Juanes, R. Thermodynamic and Hydrodynamic Constraints on Overpressure Caused by Hydrate Dissociation: A Pore-Scale Model. *Geophys. Res. Lett.* **2011**, *38*, L14308. [[CrossRef](#)]
12. Jang, J.; Santamarina, J.C. Recoverable Gas from Hydrate-bearing Sediments: Pore Network Model Simulation and Macroscale Analyses. *J. Geophys. Res. Solid Earth* **2011**, *116*, 1978–2012. [[CrossRef](#)]
13. Tsimpanogannis, I.N.; Ioannis, N.; Lichtner, P.C. Gas Saturation Resulting from Methane Hydrate Dissociation in a Porous Medium: Comparison between Analytical and Pore-network Results. *J. Phys. Chem. C* **2013**, *117*, 11104–11116. [[CrossRef](#)]
14. Wang, D.G.; Wang, C.C.; Li, C.F.; Liu, C.L.; Lu, H.L.; Wu, N.Y.; Hu, G.W.; Liu, L.L.; Meng, Q.G. Effect of Gas Hydrate Formation and Decomposition on Flow Properties of Fine-grained Quartz Sand Sediments Using X-ray CT Based Pore Network Model Simulation. *Fuel* **2018**, *226*, 516–526. [[CrossRef](#)]
15. Chen, X.Y.; Espinoza, N.D. Surface Area Controls Gas Hydrate Dissociation Kinetics in Porous Media. *Fuel* **2018**, *234*, 358–363. [[CrossRef](#)]
16. Zhan, L.; Wang, Y.; Li, X.S. Experimental Study on Characteristics of Methane Hydrate Formation and Dissociation in Porous Medium with Different Particle Sizes Using Depressurization. *Fuel* **2018**, *230*, 37–44. [[CrossRef](#)]
17. Zhang, J.H.; Zhao, C.; Xiong, Z.S. Meso-level Simulation of Gas Hydrate Dissociation in Low-permeability Sediments. *Theor. Appl. Mech. Lett.* **2014**, *4*, 062002. [[CrossRef](#)]
18. Wang, X.; Dong, B.; Li, W.Z.; Yu, M.H.; Song, Y.C. Microscale Effects on Methane Hydrate Dissociation at Low Temperature in the Micro Porous Media Channels by Depressurization. *Int. J. Heat. Mass. Trans.* **2018**, *122*, 1182–1197. [[CrossRef](#)]
19. Wang, P.F.; Yang, M.J.; Chen, B.B.; Zhao, Y.C.; Zhao, J.F.; Song, Y.C. Methane Hydrate Reformation in Porous Media with Methane Migration. *Chem. Eng. Sci.* **2017**, *168*, 344–351. [[CrossRef](#)]
20. Uchida, T.; Takeya, S.; Chuvalin, E.M.; Ohmura, R.; Nagao, J.; Yakushev, V.S.; Istomin, V.A.; Minagawa, H.; Ebinuma, T.; Narita, H. Decomposition of Methane Hydrates in Sand, Sandstone, Clays, and Glass beads. *J. Geophys. Res. Solid Earth* **2004**, *109*, B05206. [[CrossRef](#)]
21. Uchida, T.; Ebinuma, T.; Takeya, S.; Nagao, J.; Narita, H. Effects of Pore Sizes on Dissociation Temperatures and Pressures of Methane, Carbon Dioxide, and Propane Hydrates in Porous Media. *J. Phys. Chem. B* **2002**, *106*, 820–826. [[CrossRef](#)]
22. Clarke, M.A.; Pooladi-Darvish, M.; Bishnoi, P.R. A Method to Predict Equilibrium Conditions of Gas Hydrate Formation in Porous Media. *Ind. Eng. Chem. Res.* **1999**, *38*, 2485–2490. [[CrossRef](#)]
23. Seshadri, K.; Wilder, J.W.; Smith, D.H. Measurements of Equilibrium Pressures and Temperatures for Propane Hydrate in Silica Gels with Different Pore-size Distributions. *J. Phys. Chem. B* **2001**, *105*, 2627–2631. [[CrossRef](#)]
24. Wilder, J.W.; Seshadri, K.; Smith, D.H. Resolving Apparent Contradictions in Equilibrium Measurements for Clathrate Hydrates in Porous Media. *J. Phys. Chem. B* **2001**, *105*, 9970–9972. [[CrossRef](#)]
25. Klauda, J.B.; Sandler, S.I. Modeling Gas Hydrate Phase Equilibria in Laboratory and Natural Porous Media. *Ind. Eng. Chem. Res.* **2001**, *40*, 4197–4208. [[CrossRef](#)]
26. Seo, Y.; Lee, H.; Uchida, T. Methane and Carbon Dioxide Hydrate Phase Behavior in Small Porous Silica Gels: Three-Phase Equilibrium Determination and Thermodynamic Modeling. *Langmuir* **2002**, *18*, 9164–9170. [[CrossRef](#)]
27. Seo, Y.; Lee, H. Hydrate Phase Equilibria of the Ternary CH₄ + NaCl + Water, CO₂ + NaCl + Water and CH₄ + CO₂ + Water Mixtures in Silica Gel Pores. *J. Phys. Chem. B* **2003**, *107*, 889–894. [[CrossRef](#)]

28. Anderson, R.; Llamedo, M.; Tohidi, B.; Burgass, R.W. Experimental Measurement of Methane and Carbon Dioxide Clathrate Equilibria in Mesoporous Silica. *J. Phys. Chem. B* **2003**, *107*, 3507–3514. [[CrossRef](#)]
29. Seo, Y.; Lee, S.; Cha, I.; Lee, J.D.; Lee, H. Phase Equilibria and Thermodynamic Modeling of Ethane and Propane Hydrates in Porous Silica Gels. *J. Phys. Chem. B* **2009**, *113*, 5487–5492. [[CrossRef](#)]
30. Lee, S.; Seo, Y. Experimental Measurement and Thermodynamic Modeling of the Mixed $\text{CH}_4 + \text{C}_3\text{H}_8$ Clathrate Equilibria in Silica Gel Pores: Effects of Pore Size and Salinity. *Langmuir* **2010**, *26*, 9742–9748. [[CrossRef](#)]
31. Liu, X.; Flemings, P.B. Capillary Effects on Hydrate Stability in Marine Sediments. *J. Geophys. Res.* **2011**, *116*, B07102. [[CrossRef](#)]
32. Anderson, R.; Tohidi, B.; Webber, J.B.W. Gas Hydrate Growth and Dissociation in Narrow Pore Networks: Capillary Inhibition and Hysteresis Phenomena. *Geol. Soc. Spec. Publ.* **2009**, *319*, 145–159. [[CrossRef](#)]
33. Bangs, N.L.B.; Musgrave, R.J.; Tréhu, A.M. Upward Shifts in the Southern Hydrate Ridge Gas Hydrate Stability Zone Following Postglacial Warming, Offshore Oregon. *J. Geophys. Res.* **2005**, *110*, B03102. [[CrossRef](#)]
34. Liu, X.; Flemings, P.B. Passing Gas through the Hydrate Stability Zone at Southern Hydrate Ridge, Offshore Oregon. *Earth Planet. Sci. Lett.* **2006**, *241*, 211–226. [[CrossRef](#)]
35. Daigle, H.; Dugan, B. Pore Size Controls on the Base of the Methane Hydrate Stability Zone in the Kumano Basin, Offshore Japan. *Geophys. Res. Lett.* **2014**, *41*, 8021–8028. [[CrossRef](#)]
36. Uchida, T.; Ebinuma, T.; Ishizaki, T. Dissociation Condition Measurements of Methane Hydrate in Confined Small Pores of Porous Glass. *J. Phys. Chem. B* **1999**, *103*, 3659–3662. [[CrossRef](#)]
37. Park, T.; Lee, J.Y.; Kwon, T.-H. Effect of Pore Size Distribution on Dissociation Temperature Depression and Phase Boundary Shift of Gas Hydrate in Various Fine-Grained Sediments. *Energy Fuels* **2018**, *32*, 5321–5330. [[CrossRef](#)]
38. Handa, Y.P.; Stupin, D. Thermodynamic Properties and Dissociation Characteristics of Methane and Propane Hydrates in 70-Å-Radius Silica Gel Pores. *J. Phys. Chem.* **1992**, *96*, 8599–8603. [[CrossRef](#)]
39. Watanabe, K.; Mizoguchi, M. Amount of Unfrozen Water in Frozen Porous Media Saturated with Solution. *Cold Reg. Sci. Technol.* **2002**, *34*, 103–110. [[CrossRef](#)]
40. Istomin, V.; Chuvalin, E.; Bukhanov, B.; Uchida, T. Pore Water Content in Equilibrium with Ice or Gas Hydrate in Sediments. *Cold Reg. Sci. Technol.* **2017**, *137*, 60–67. [[CrossRef](#)]
41. Morishige, K.; Iwasaki, H. X-ray Study of Freezing and Melting of Water Confined within SBA-15. *Langmuir* **2003**, *19*, 2808–2811. [[CrossRef](#)]
42. Morishige, K. Influence of Pore Wall Hydrophobicity on Freezing and Melting of Confined Water. *J. Phys. Chem. C* **2018**, *122*, 5013–5019. [[CrossRef](#)]
43. Handa, Y.P.; Zakrzewski, M.; Fairbridge, C. Effect of Restricted Geometries on the Structure and Thermodynamic Properties of Ice. *J. Phys. Chem.* **1992**, *96*, 8594–8599. [[CrossRef](#)]
44. Sun, Q. Local Statistical Interpretation for Water Structure. *Chem. Phys. Lett.* **2013**, *568–569*, 90–94. [[CrossRef](#)]
45. Baschenko, S.M.; Marchenko, L.S. On Raman Spectra of Water, Its Structure and Dependence on Temperature. *Semicond. Phys. Quan. Elec. Optoelec.* **2011**, *14*, 77–79. [[CrossRef](#)]
46. Webber, J.B.W.; Dore, J.C.; Strange, J.H.; Anderson, R.; Tohidi, B. Plastic Ice in Confined Geometry: The Evidence from Neutron Diffraction and NMR Relaxation. *J. Phys. Condens. Matter* **2007**, *19*, 415117. [[CrossRef](#)]
47. Sun, A.K.; Burruss, R.C.; Sloan, E.D. Measurement of Clathrate Hydrates via Raman Spectroscopy. *J. Phys. Chem. B* **1997**, *101*, 7371–7377. [[CrossRef](#)]
48. Liu, C.L.; Meng, Q.G.; He, X.L.; Li, C.F.; Ye, Y.G.; Zhang, G.X.; Liang, J.Q. Characterization of Natural Gas Hydrate Recovered from Pearl River Mouth Basin in South China Sea. *Mar. Petrol. Geol.* **2015**, *61*, 14–21. [[CrossRef](#)]
49. Kuhs, W.F.; Genov, G.; Staykova, D.K.; Hansen, T. Ice Perfection and Onset of Anomalous Preservation of Gas Hydrates. *Phys. Chem. Chem. Phys.* **2004**, *6*, 4917–4920. [[CrossRef](#)]
50. Takeya, S.; Shimada, W.; Kamata, Y.; Ebinuma, T.; Uchida, T.; Nagao, J.; Narita, H. In Situ X-ray Diffraction Measurements of the Self-preservation Effect of CH_4 Hydrate. *J. Phys. Chem. A* **2001**, *105*, 9756–9759. [[CrossRef](#)]
51. Stern, L.A.; Circone, S.; Kirby, S.H.; Durham, W.B. Temperature, Pressure, and Compositional Effects on Anomalous or “Self” Preservation of Gas Hydrates. *Can. J. Phys.* **2003**, *81*, 271–283. [[CrossRef](#)]

52. English, N.J.; Phelan, G.M. Molecular Dynamics Study of Thermal-driven Methane Hydrate Dissociation. *J. Chem. Phys.* **2009**, *131*, 074704. [[CrossRef](#)] [[PubMed](#)]
53. Das, S.; Baghel, V.S.; Roy, S.; Kumar, R. Molecular Dynamics Study of Model SI Clathrate Hydrates: Effect of Guest Size and Guest–Water Interaction on Decomposition Kinetics. *Phys. Chem. Chem. Phys.* **2015**, *17*, 9509–9518. [[CrossRef](#)] [[PubMed](#)]
54. Van der Waals, J.H.; Platteeuw, J.C. Clathrate Solutions. *Adv. Chem. Phys.* **1959**, *2*, 1–57.
55. Susilo, R.; Ripmeester, J.A.; Englezos, P. Characterization of Gas Hydrates with PXRD, DSC, NMR, and Raman Spectroscopy. *Chem. Eng. Sci.* **2007**, *62*, 3930–3939. [[CrossRef](#)]
56. Subramanian, S.; Sloan, E.D. Trends in Vibrational Frequencies of Guests Trapped in Clathrate Hydrate Cages. *J. Phys. Chem. B* **2002**, *106*, 4348–4355. [[CrossRef](#)]
57. Tsimpanogiannis, I.N.; Diamantonis, N.I.; Economou, I.G.; Papadimitriou, N.I.; Stubos, A.K. Influence of Combining Rules on the Cavity Occupancy of Clathrate Hydrates Using van der Waals–Platteeuw-Theory-Based Modelling. *Chem. Eng. Res. Des.* **2014**, *92*, 2992–3007. [[CrossRef](#)]
58. Goussard, J.O.; Roulet, B. Free Expansion for Real Gases. *Am. J. Phys.* **1993**, *61*, 845–848. [[CrossRef](#)]
59. Wang, J.J.; Dong, M.Z.; Yang, Z.H.; Gong, H.J.; Li, Y.J. Investigation of Methane Desorption and its Effect on the Gas Production Process from Shale: Experimental and Mathematical Study. *Energy Fuels* **2017**, *31*, 205–216. [[CrossRef](#)]
60. Jung, J.W.; Santamarina, J.C. Hydrate Formation and Growth in Pores. *J. Cryst. Growth* **2012**, *345*, 61–68. [[CrossRef](#)]
61. Aladko, E.Y.; Dyadin, Y.A.; Fenelonov, V.B.; Larionov, E.G.; Mel'gunov, M.S.; Manakov, A.Y.; Nesterov, A.N.; Zhurko, F.V. Dissociation Conditions of Methane Hydrate in Mesoporous Silica Gels in Wide Ranges of Pressure and Water Content. *J. Phys. Chem. B* **2004**, *108*, 16540–16547. [[CrossRef](#)]



© 2019 by the authors. Licensee MDPI, Basel, Switzerland. This article is an open access article distributed under the terms and conditions of the Creative Commons Attribution (CC BY) license (<http://creativecommons.org/licenses/by/4.0/>).

Article

Collective Transformation of Water between Hyperactive Antifreeze Proteins: *RiAFPs*

Kenji Mochizuki ^{1,2,*} and Masakazu Matsumoto ³

¹ Institute for Fiber Engineering, Shinshu University, Ueda 386-8567, Japan

² Department of Chemistry and Materials, Faculty of Textile Science and Technology, Ueda 386-8567, Japan

³ Research Institute for Interdisciplinary Science, Okayama University, Okayama 700-8530, Japan; vitroid@gmail.com

* Correspondence: mochizuki@shinshu-u.ac.jp; Tel.: +81-268-21-5300

Received: 7 March 2019; Accepted: 27 March 2019; Published: 1 April 2019

Abstract: We demonstrate, by molecular dynamics simulations, that water confined between a pair of insect hyperactive antifreeze proteins from the longhorn beetle *Rhagium inquisitor* is discontinuously expelled as the two proteins approach each other at a certain distance. The extensive striped hydrophobic-hydrophilic pattern on the surface, comprising arrays of threonine residues, enables water to form three independent ice channels through the assistance of hydroxyl groups, even at 300 K. The transformation is reminiscent of a freezing–melting transition rather than a drying transition and governs the stable protein–protein separation in the evaluation of the potential of mean force. The collectivity of water penetration or expulsion and the hysteresis in the time scale of ten nanoseconds predict a potential first-order phase transition at the limit of infinite size and provide a new framework for the water-mediated interaction between solutes.

Keywords: antifreeze protein; potential of mean force; molecular dynamics; freezing

1. Introduction

Water confined in nanopores exhibits anomalous behaviors dissimilar to those of bulk water, e.g., the transition to low-dimensional ices [1,2] and solid–liquid critical points [3,4]. The dewetting (drying) transition is one such intriguing behavior; when two large-scale strongly hydrophobic solutes approach each other at a critical distance, water molecules are expelled from the intersolute region, leading to hydrophobic collapse [5–9]. Hydrophobicity is believed to play a key role in the self-assembly of macromolecules [10–14], and hydrophobic dewetting is observed in the formation of protein complexes [15–20]. On the other hand, most protein–protein interfaces are enriched in polar residues rather than nonpolar ones [21] and water molecules are involved in the association of hydrophilic surfaces [22–24]. As a small portion of hydrophilic moieties prevents the occurrence of the dewetting transition [25,26], the thermodynamic properties of interfacial water are significantly sensitive to the local geometry and chemical patterning of solutes [27,28]. The precise control of surface heterogeneity would provide design principles for the alignment and separation of macromolecules in aqueous solutions [29].

Hydrophobicity is characteristic of the ice-binding surface (IBS) of antifreeze proteins (AFPs) [30–32]. AFPs have evolved in a variety of organisms, e.g., fish, insects, bacteria, and plants that survive in sub-zero-temperature environments [30]. Although AFPs have a remarkable diversity in structure, they possess the same function of adsorption to ice [33]. This adsorption to ice results in thermal hysteresis (TH), a gap between the depressed freezing- and promoted melting-temperatures of ice, through the Gibbs–Thomson (Kelvin) effect [34,35]. Insect AFPs are categorized as “hyperactive” in TH and are more than 10 times effective compared with moderately active AFPs, on the basis of concentration [36]. In particular, *RiAFP* from the longhorn beetle *Rhagium inquisitor*, which can

supercool to below -25°C [37], exhibits the most potent TH activity among the currently known AFPs [38].

*Ri*AFP has an exceptionally flat and wide IBS comprising four parallel arrays of threonine (T or Thr) residues, which is referred to as the T-X-T-X-T-X-T motif, with X being a nonconserved amino acid. Although the flat IBS with T-X-T motif is also observed in the other hyperactive insect AFPs from *Tenebrio molitor* (*Tm*AFP) [39] and *Choristoneura fumiferana* (*Cf*AFP) [40], the 420 \AA^2 IBS in *Ri*AFP is significantly larger than that of *Tm*AFP (150 \AA^2) and *Cf*AFP (190 \AA^2) [41]. On the IBS of *Ri*AFP, the side chains of the Thr residues exhibit the same orientation, and water molecules are buried between the arrays of Thr [41]. Hence, the IBS of *Ri*AFP has an extensive striped pattern comprising CH_3 , OH groups, and crystallographic water.

In the present study, we performed molecular dynamics (MD) simulations for a pair of *Ri*AFPs dissolved in water and examined the phase behavior of water in the interprotein region. Our analyses for hysteresis between the association and dissociation processes and the discontinuous change in confined water molecules reveal a collective structural transformation of the confined water, dissimilar to the drying transition [5–9]. Furthermore, we computed the potential of mean force (PMF) as a function of the interprotein distance and found that three independent ice channels are formed in the deepest PMF minimum.

2. Methods

2.1. Molecular Dynamics Simulation

MD simulations were conducted using the GROMACS 2018.3 package [42]. The equations of motion were integrated with the leap-frog algorithm using a time step of 2 fs. The temperature T for production runs was controlled using the Nose–Hoover thermostat [43,44] with damping constants of 1.0 ps, whereas the Berendsen algorithm [45] was used for equilibration. The pressure p is isotropically controlled using the Berendsen algorithm [45] with damping constants of 2.0 ps. All the bonds were constrained using the LINCS algorithm. Periodic boundary conditions were applied in all three directions.

*Ri*AFP was modelled with full atomistic detail using CHARMM27 (CHARMM22 plus CMAP correction) [46,47]. Water was modelled with TIP4P/2005 [48]. Intermolecular interactions were truncated at 0.85 nm. The Lennard-Jones parameters of cross-interactions were obtained using the Lorentz–Berthelot combining rules. Long-range Coulombic interactions were evaluated using the particle-mesh Ewald algorithm (Fourier spacing of 0.10 nm), and dispersion corrections were implemented for the energy and pressure evaluations.

The crystallographic structure of the *Ri*AFP dimer was taken from the protein data bank (PDB code 4DT5) [41]. In the dimer, the IBS of two chains of the protein face each other. These two chains of the protein have different sizes and consist of 143 and 138 residues, respectively. We cut five residues at the end of the longer protein to make it identical to the shorter one, and we capped the proteins with N-terminal acetyl and C-terminal methyl (CH_3) groups. It should be noted that the five cut residues were not involved in the IBS. The PDB file also included crystallographic water molecules between two chains of the protein. The *Ri*AFP dimer with these adhered water molecules was immersed into a rectangular box of bulk water. The total number of water molecules was 10,800 and twelve chloride ions were added to neutralize the system charge. We arranged the IBS of the protein to be parallel to the yz -plane, as shown in Figure 1. The system was firstly relaxed using the steepest-descent method. To relax the solvent structure, we performed a 100 ps MD simulation in the canonical (*NVT*) ensemble at 300 K with freezing the proteins. Then, a 100 ps MD simulation in the isobaric isothermal (*NpT*) ensemble at 300 K and 10 MPa was followed by a 100 ps *NpT*-MD simulation at 300 K and 0.1 MPa to equilibrate the volume. During these *NpT*-MD simulations, the positions of all the alpha carbon (CA) atoms were harmonically restrained at their original positions with a force constant of

1000 kJ·mol⁻¹·nm⁻². The resulting configuration with box dimensions of 9.93 × 5.96 × 5.96 nm³ was used as the initial configuration for the subsequent NVT-MD simulations.

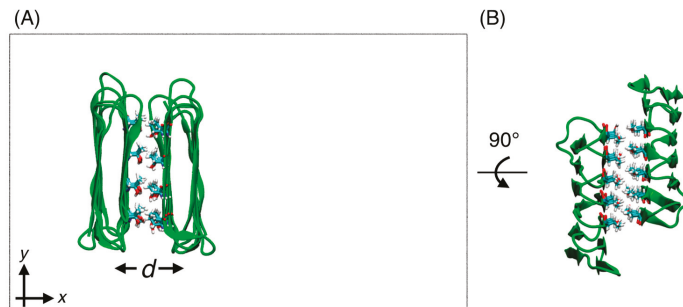


Figure 1. A dimer of RiAFP (*Rhagium inquisitor* antifreeze proteins) dissolved in water in the configurations: (A) end-on with the simulation box dimension (black lines) and (B) with 90° rotation. The Thr residues involved in the protein–protein contact are represented by sticks. Water molecules and ions are not shown. The two-way arrow indicates the distance d between the centers of mass of the RiAFPs parallel to the x-axis. d for this conformation is 1.50 nm.

2.2. Potential of Mean Force

To compute the PMF between two chains of RiAFPs, a set of NVT-MD simulations were performed. To keep the mutual orientation parallel, the x , y , and z positions of all the CA atoms in one protein, as shown on the left in Figure 1, and the y and z positions of the CA atoms in the other protein were harmonically restrained at their original positions with a force constant of 1000 kJ·mol⁻¹·nm⁻². The controlled interprotein distance d is parallel to the x -axis and is between the centers of mass of two chains of the protein. The RiAFP dimer taken from the PDB shows $d = 1.50$ nm. To observe the dissociation process, d was increased in stages up to 2.50 nm, in increments of 0.02 nm. Then, d was decreased from 2.00 to 1.50 nm for the association process. At a given d , an NVT-MD simulation was performed for 10 ns at 300 K. Data analysis was performed based on the last 4 ns of the simulation runs. We recorded the force acting on each protein every 10 ps and obtained the average force $F(d)$ over time and over two chains of the protein [49]. The PMF between two chains of RiAFPs $w(d)$ was computed by an integration

$$w(d) = - \int_{d_0}^d F(r) dr + w_0,$$

where d_0 is a reference separation and w_0 is an arbitrary constant. The average PMF values between $d = 2.30$ and 2.40 nm was set to zero.

2.3. Water Molecules Confined Between Two Chains of RiAFPs

The interprotein region is defined as a rectangular box spanning the CA atoms of Thr on the IBS; x ranges from the CA of Thr41 of the left protein to the CA of Thr109 of the right protein; y ranges from the CA of Thr109 of the right protein to the CA of Thr47 of the left protein; z ranges from the CA of Thr41 to the CA of Thr109 of the right protein. The position of the oxygen atom of a water molecule was used to judge whether the molecule was included in the above box.

3. Results and Discussion

3.1. Hysteresis Between Association and Dissociation of RiAFP Dimer Without Rotation

We firstly investigated how the number of water molecules (N_w) between two RiAFPs changes during the association and dissociation processes. The IBSs of the two proteins face each other

and the interprotein distance perpendicular to the surface (d) varies while preserving a parallel orientation. At $d = 1.50$ nm, the CH_3 groups of the two proteins are in contact distance. However, the crystallographic water molecules remain adhered on the protein surface even after an MD run of 10 ns, giving an average N_w , $\langle N_w \rangle$, of 25, as shown in Figure 2A. The penetration of additional water molecules was not observed up to $d = 1.60$ nm. $\langle N_w \rangle$ increases gradually from $d = 1.62$ to 1.72 nm; at $d = 1.74$ nm, we observed a distinct increase in $\langle N_w \rangle$ from 38 to 52. The time evolution of N_w at $d = 1.74$ nm demonstrates that the penetration of water molecules takes ~5 ns, as shown in Figure 2B. At $d > 1.74$ nm, $\langle N_w \rangle$ monotonically increases with the interprotein distance. We also computed $\langle N_w \rangle$ during the backward association process, as shown by the blue line in Figure 2A. Except for the distances between 1.68 and 1.72 nm, $\langle N_w \rangle$ during the association process is almost identical to the values in the dissociation process, indicating that $\langle N_w \rangle$ is independent of the history. In contrast, at $d = 1.68$, 1.70, and 1.72 nm, $\langle N_w \rangle$ differs for the inverse processes. For example, 48 water molecules remain in the interprotein region as the two proteins approach $d = 1.70$ nm, whereas only 33 molecules are included in the same volume as the two proteins separate. Furthermore, at $d = 1.66$ nm during the association process, several water molecules are simultaneously expelled from the interprotein region, which takes ~6 ns, as shown in Figure 2C. Although d was further decreased to 1.50 nm, complete drying did not occur. The observed discontinuous change in $\langle N_w \rangle$ and hysteresis implies a collective structural transformation, which may lead a first-order phase transition at the infinite limit of surface size, in both the association and dissociation processes.

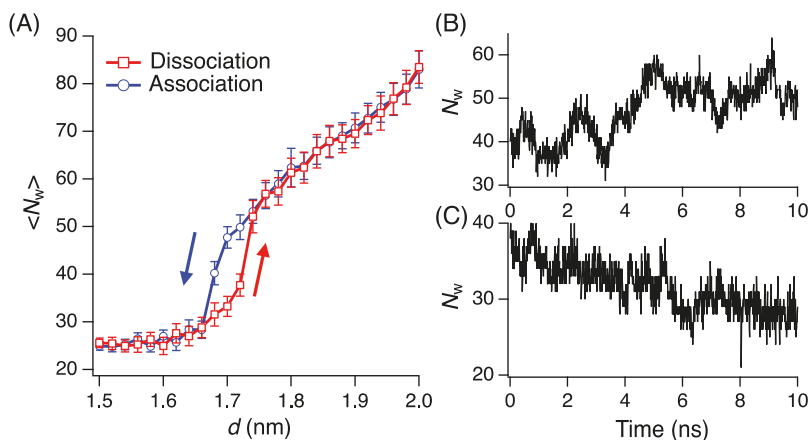


Figure 2. Number of water molecules N_w between two proteins; (A) the average, $\langle N_w \rangle$, as a function of the intersolute distance d during the association (blue) and dissociation (red) processes, and the time evolution of N_w at (B) $d = 1.74$ nm during the dissociation, and (C) $d = 1.66$ nm during the association.

3.2. Potential of Mean Force

The PMF, $w(r)$, for a pair of *Ri*AFPs was computed as a function of the separation d , as shown in Figure 3A. For each of the association and dissociation processes, we firstly estimated two PMFs in the regions before and after the distinct jump of $\langle N_w \rangle$. Then, we assumed that the two PMFs were connected at $d = 1.70$ nm, which is the middle of hysteresis. The PMFs at $1.70 < d < 2.00$ nm well agree for these inverse processes. On the other hand, the depth of the PMF minimum at around $d = 1.52$ nm depends on the history. Although $\langle N_w \rangle$ s in the two processes were almost identical at $d < 1.66$ nm, as shown in Figure 2A, the water structure in the interprotein region during the dissociation was more ordered than the association. More specifically, the water hexamers in the interprotein region were more disrupted by defects during the association than those during the dissociation. If much longer simulations were performed at each d during the association, the water structure and the resulting free

energy would be identical to that observed for the dissociation. We claim that the PMFs computed for the association and dissociation were qualitatively the same. In the following analyses, we use the conformations sampled during the dissociation.

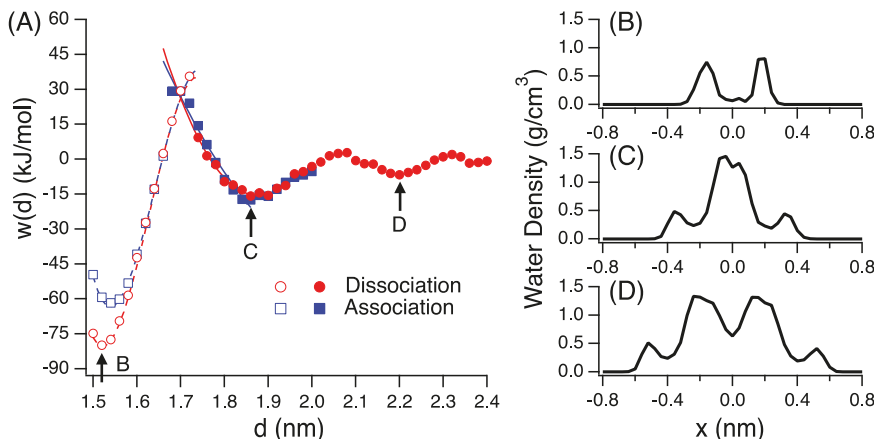


Figure 3. (A) Potential of mean force $w(d)$ between *Ri*AFPs as a function of the separation d during the dissociation (blue) and association (red) processes. The dashed and solid lines represent third- and fourth-order polynomial fits, respectively. (B) Density profile of water confined between the two proteins at $d = 1.52$ nm, (C) 1.86 nm, and (D) 2.20 nm. In panels B–D, the center of the two proteins is set to $x = 0$. The typical error bars in the potential of mean force (PMF) are of the order of 5 kJ/mol.

The deepest minimum in the PMF was at $d = 1.52$ nm. Figure 3B depicts the density profile of water molecules in the interprotein region at this minimum. Two strong peaks arise from the water molecules localized between arrays of Thr residues. The second-deepest minimum was located at $d = 1.86$ nm. The water density profile shows three symmetric intervening water layers at this separation, as shown in Figure 3C. Two side peaks from the water molecules on the IBSs broaden at this separation, indicating that these molecules were less localized than those at the deepest minimum. The remaining large peak at the center arises from one water layer spread over the interprotein region. These results indicate that the free energy barrier separating these minima at $d = 1.52$ and 1.86 nm were associated with the penetration or expulsion of a single water layer in the confined space. The activation free energy from the second minimum to the first one was approximately 45 kJ/mol, corresponding to $18 k_B T$, with k_B being the Boltzmann constant. This significantly high barrier to form a dimer may pertain to the experimental observation that *Ri*AFPs exist as monomers in solution [41].

A further increase in d leads to the penetration of one more water layer between two chains of the protein and the formation of a shallow PMF minimum at $d = 2.20$ nm, with four symmetric water layers, as shown in Figure 3D. The separation between the first and second minima and between the second and third minima was 0.34 nm, consistent with the size of water molecules computed from the radial distribution function [48]. Therefore, as observed for the water between hydrophobic plates [49,50], the distinct number of water layers stabilizes the protein–protein separation, leading to the minima in PMF. Furthermore, the penetration or expulsion of one water layer results in the free energy barriers between these minima.

3.3. Three Ice Channels

To characterize the collective transformation, we observed the molecular structures comprising of the caught water molecules and hydroxyl (OH) groups of Thr in the interprotein region. At distances between 1.50 and 1.60 nm, we found that three independent ice channels were formed, as shown in

Figure 4A. A hexamer consists of three water molecules and three OH groups, and the neighboring three or four hexamers make one channel. The arrays of CH₃ groups assist these channels to be independent, by separating the interprotein space. The chair-form hexagonal ring is one of the most stable conformations for water molecules in terms of potential energy and is observed in hexagonal ice (ice Ih). Indeed, we found that the average potential energy of -76.4 kJ/mol for the confined water molecules at $d = 1.52 \text{ nm}$ was significantly lower than -66.2 kJ/mol at $d = 1.86 \text{ nm}$. According to the hexagonal conformations and the stabilized potential energy, the water structure at small d_s can be considered as an “ice” phase. As d becomes greater than 1.60 nm , additional water molecules begin to penetrate the interprotein region and disturb the ordered ice structures. Figure 4B shows the snapshot at $d = 1.70 \text{ nm}$ during the dissociation, just before the distinct $\langle N_w \rangle$ jump happens. The penetrated molecules connect the middle and bottom channels, shown by the red lines in Figure 4B. However, some hexagonal rings, indicated by orange arrows, are retained. Furthermore, the top channel is still isolated and has an ordered structure, although the distance between the OH group of one protein and the water molecules on the other protein is extended. Figure 3A shows that this structure is still in the same PMF minimum as the three ice channels. Hence, the conformation with d between 1.60 and 1.70 nm can be considered as a defective ice phase. When d is further increased, the network in the interprotein region percolates and the structure looks disordered, analogous to liquid water, as shown in Figure 4C. These conformational analyses, along with the PMF, suggest that the collective water transformation observed in the RiAFP dimerization is similar to the freezing–melting transitions of water.

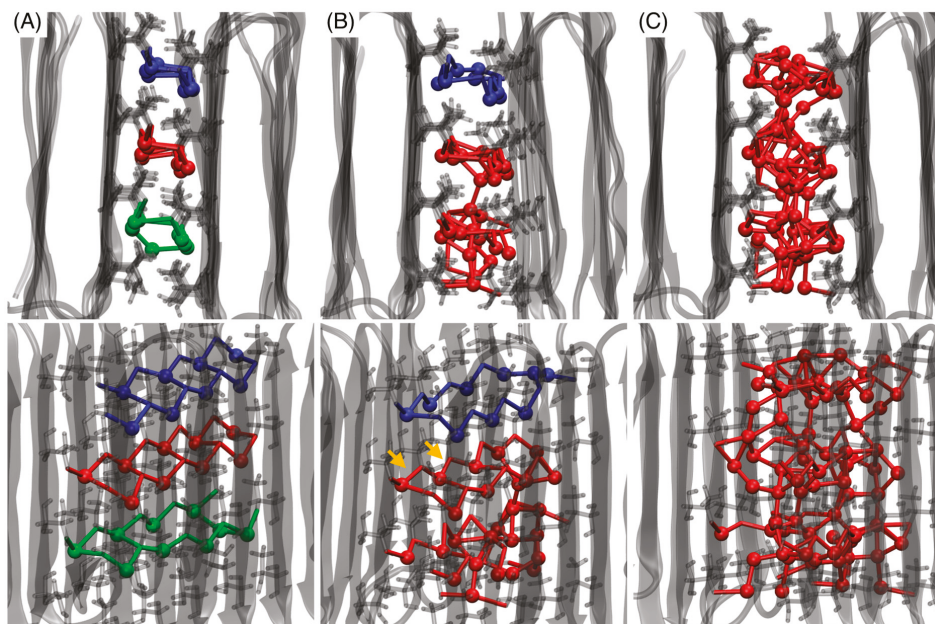


Figure 4. Characteristic instantaneous structures comprising water molecules and OH groups in the interprotein region, observed at (A) $d = 1.52$, (B) 1.70 , and (C) 1.86 nm during the dissociation. These d_s correspond to the first minimum, first barrier, and second minimum in the PMF. At each d , two views from different angles are shown. The water molecule and the OH groups are connected by lines if their oxygen–oxygen distance is shorter than 0.34 nm , which is the first minimum of the oxygen–oxygen radial distribution function for bulk water [48]. Water molecules are represented by balls. The transparent gray shapes show proteins in cartoon representation and the sticks represent Thr residues on the ice-binding surfaces (IBSs). The orange arrows in panel B indicate the remaining hexamers.

3.4. Ice Channels between Unrestrained Proteins

To confirm the formation of ice channels in a realistic condition, we performed an NVT-MD simulation of unrestrained *Ri*AFPs for 10 ns. The initial configuration was the dimer with $d = 1.52$ nm, obtained in the trajectory for restrained *Ri*AFPs, as shown in Figure 4A. Figure 5 shows that the parallel dimer configuration was preserved over 10 ns although the dimer itself migrates. The three independent ice channels were also preserved over 10 ns, which can be seen as hexagonal rings in Figure 5B. We found that among 26 water molecules between two chains of *Ri*AFP in the initial configuration, 20 water molecules were arrested at the same position in the interprotein region at the final time step. Hence, these confined water molecules migrate together with the proteins. These results indicate that the parallel dimer structure of *Ri*AFP with ice channels was stable, at least in the order of tens of nanoseconds, even under the realistic condition.

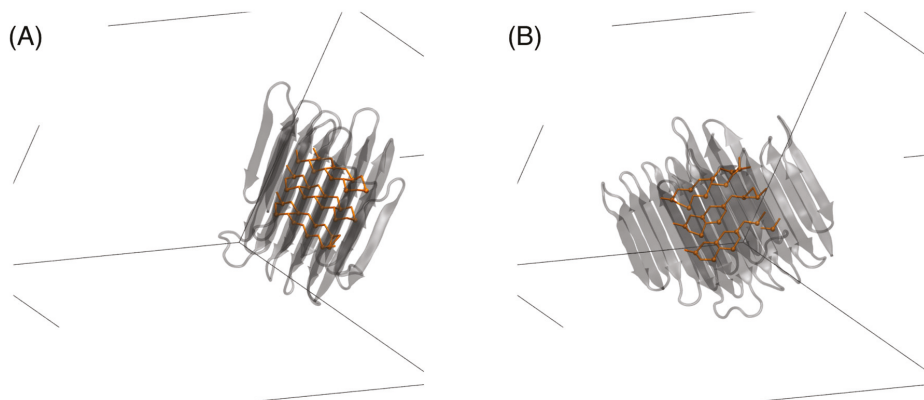


Figure 5. Instantaneous structures of *Ri*AFPs and water molecules between them, obtained at (A) the initial and (B) final steps of the 10 ns molecular dynamics (MD) simulation, for unrestrained proteins from the same viewpoints. A water molecule and an OH group of a Thr residue are connected by an orange line if their oxygen–oxygen distance is shorter than 0.34 nm. Gray lines represent the simulation box.

4. Conclusions

In summary, our MD simulations present that the approach of *Ri*AFPs induces the spontaneous formation of ordered hydrogen bond networks in the interprotein region, named ice channels, even at room temperature. The collective structural transformation into chair-form hexamers, comprising water and OH groups, resembles the crystallization of liquid water, and not the drying transition observed between large hydrophobic solutes. The discontinuous penetration or expulsion of confined water and the hysteresis between the association and dissociation of these proteins imply a potential first-order phase transition at the limit of infinite size.

This unique transition certainly arises from the extensive striped hydrophobic–hydrophilic pattern on the *Ri*AFP surface, called the T-X-T motif. This T-X-T motif is also present in the other insect hyperactive AFPs. Similar to *Ri*AFP, these AFPs form multimers with their T-X-T motifs facing each other in the crystallographic structure [39,40,51,52]. Hence, the collective transformation to ice channels may be a common feature in their dimerizations. Furthermore, AFPs with the T-X-T motif are known to be hyperactive in the TH measurement [30], and they bind to ice through an anchored clathrate [53]. The water molecules between arrays of Thr on the IBS and the OH groups of Thr are involved in the anchored clathrate. Hence, the molecular basis to facilitate the ice channels between two *Ri*AFPs and the anchored clathrate between *Ri*AFP and ice surface can be considered to be the same. On the other hand, the formation of an ice-like ordered structure is not necessary for the discontinuous water

penetration or expulsion, because, in the case of graphene plates, the PMF and the amount of confined water change smoothly, regardless of the formation of defective bilayer ice [49]. Although a concrete understanding of the surface chemistry and geometry required to induce the collective transformation of confined water requires further studies, our finding provides a new framework for water-mediated solute–solute interactions, which may play a role in the self-organization of soluble molecules.

Author Contributions: Analysis and revision, M.M. Conceptualization, analysis and writing, K.M.

Funding: We acknowledge support from the Japan Society for the Promotion of Science (KAKENHI 18K19060, 15H05474 and 16K05658).

Acknowledgments: K.M. thanks Koji Umezawa for insightful discussions. Most calculations were performed at the Research Center for Computational Science in Okazaki, Japan.

Conflicts of Interest: The authors declare no conflict of interest.

References

- Koga, K.; Gao, G.T.; Tanaka, H.; Zeng, X.C. Formation of ordered ice nanotubes inside carbon nanotubes. *Nature* **2001**, *412*, 802–805. [[CrossRef](#)] [[PubMed](#)]
- Koga, K.; Zeng, X.C.; Tanaka, H. Freezing of confined water: A bilayer ice phase in hydrophobic nanopores. *Phys. Rev. Lett.* **1997**, *79*, 5262–5265. [[CrossRef](#)]
- Mochizuki, K.; Koga, K. Solid-liquid critical behavior of water in nanopores. *Proc. Natl. Acad. Sci. USA* **2015**, *112*, 8221–8226. [[CrossRef](#)]
- Han, S.; Choi, M.Y.; Kumar, P.; Eugene Stanley, H. Phase transitions in confined water nanofilms. *Nat. Phys.* **2010**, *6*, 685–689. [[CrossRef](#)]
- Berne, B.J.; Weeks, J.D.; Zhou, R. Dewetting and hydrophobic interaction in physical and biological systems. *Annu. Rev. Phys. Chem.* **2009**, *60*, 85–103. [[CrossRef](#)] [[PubMed](#)]
- Wallqvist, A.; Berne, B.J. Computer simulation of hydrophobic hydration forces on stacked plates at short range. *J. Phys. Chem.* **1995**, *99*, 2893–2899. [[CrossRef](#)]
- Lum, K.; Chandler, D.; Weeks, J.D. Hydrophobicity at small and large length scales. *J. Phys. Chem. B* **1999**, *103*, 4570–4577. [[CrossRef](#)]
- Lum, K.; Luzar, A. Pathway to surface-induced phase transition of a confined fluid. *Phys. Rev. E* **1997**, *56*, R6283–R6286. [[CrossRef](#)]
- Huang, X.; Margulis, C.J.; Berne, B.J. Dewetting-induced collapse of hydrophobic particles. *Proc. Natl. Acad. Sci. USA* **2003**, *100*, 11953–11958. [[CrossRef](#)]
- Zhou, R.; Huang, X.; Margulis, C.J.; Berne, B.J. Hydrophobic collapse in multidomain protein folding. *Science* **2004**, *305*, 1605–1609. [[CrossRef](#)] [[PubMed](#)]
- Ball, P. Water as an active constituent in cell biology. *Chem. Rev.* **2008**, *108*, 74–108. [[CrossRef](#)] [[PubMed](#)]
- Mochizuki, K.; Pattenade, S.R.; Ben-Amotz, D. Influence of Cononsolvency on the Aggregation of Tertiary Butyl Alcohol in Methanol-Water Mixtures. *J. Am. Chem. Soc.* **2016**, *138*, 9045–9048. [[CrossRef](#)] [[PubMed](#)]
- Mochizuki, K.; Sumi, T.; Koga, K. Driving forces for the pressure-induced aggregation of poly(N-isopropylacrylamide) in water. *Phys. Chem. Chem. Phys.* **2016**, *18*, 4697–4703. [[CrossRef](#)] [[PubMed](#)]
- Mochizuki, K.; Ben-Amotz, D. Hydration-Shell Transformation of Thermosensitive Aqueous Polymers. *J. Phys. Chem. Lett.* **2017**, *8*, 1360–1364. [[CrossRef](#)] [[PubMed](#)]
- Dyson, H.J.; Wright, P.E.; Scheraga, H.A. The role of hydrophobic interactions in initiation and propagation of protein folding. *Proc. Natl. Acad. Sci. USA* **2006**, *103*, 13057–13061. [[CrossRef](#)] [[PubMed](#)]
- Liu, P.; Huang, X.; Zhou, R.; Berne, B.J. Observation of a dewetting transition in the collapse of the melittin tetramer. *Nature* **2005**, *437*, 159–162. [[CrossRef](#)]
- Chandler, D. Interfaces and the driving force of hydrophobic assembly. *Nature* **2005**, *437*, 640–647. [[CrossRef](#)]
- Ahmad, M.; Gu, W.; Helms, V. Mechanism of fast peptide recognition by SH₃ domains. *Angew. Chem. Int. Ed. Engl.* **2008**, *47*, 7626–7630. [[CrossRef](#)]
- Hua, L.; Huang, X.; Liu, P.; Zhou, R.; Berne, B.J. Nanoscale dewetting transition in protein complex folding. *J. Phys. Chem. B* **2007**, *111*, 9069–9077. [[CrossRef](#)]
- Young, T.; Hua, L.; Huang, X.; Abel, R.; Friesner, R.; Berne, B.J. Dewetting transitions in protein cavities. *Proteins* **2010**, *78*, 1856–1869. [[CrossRef](#)]

21. Ansari, S.; Helms, V. Statistical analysis of predominantly transient protein-protein interfaces. *Proteins* **2005**, *61*, 344–355. [[CrossRef](#)] [[PubMed](#)]
22. Ahmad, M.; Gu, W.; Geyer, T.; Helms, V. Adhesive water networks facilitate binding of protein interfaces. *Nat. Commun.* **2011**, *2*, 261. [[CrossRef](#)] [[PubMed](#)]
23. Ulucan, O.; Jaitly, T.; Helms, V. Energetics of Hydrophilic protein-protein association and the role of water. *J. Chem. Theory Comput.* **2014**, *10*, 3512–3524. [[CrossRef](#)] [[PubMed](#)]
24. Galamba, N.; Pipolo, S. On the binding free energy and molecular origin of sickle cell hemoglobin aggregation. *J. Phys. Chem. B* **2018**, *122*, 7475–7483. [[CrossRef](#)] [[PubMed](#)]
25. Hua, L.; Zangi, R.; Berne, B.J. Hydrophobic interactions and dewetting between plates with hydrophobic and hydrophilic domains. *J. Phys. Chem. C* **2009**, *113*, 5244–5253. [[CrossRef](#)]
26. Giovambattista, N.; Debenedetti, P.G.; Rossky, P.J. Hydration behavior under confinement by nanoscale surfaces with patterned hydrophobicity and hydrophilicity. *J. Phys. Chem. C* **2006**, *111*, 1323–1332. [[CrossRef](#)]
27. Xi, E.; Venkateshwaran, V.; Li, L.; Rego, N.; Patel, A.J.; Garde, S. Hydrophobicity of proteins and nanostructured solutes is governed by topographical and chemical context. *Proc. Natl. Acad. Sci. USA* **2017**, *114*, 13345–13350. [[CrossRef](#)]
28. Acharya, H.; Vembanur, S.; Jamadagni, S.N.; Garde, S. Mapping hydrophobicity at the nanoscale: Applications to heterogeneous surfaces and proteins. *Faraday Discuss.* **2010**, *146*, 353. [[CrossRef](#)]
29. Monroe, J.I.; Shell, M.S. Computational discovery of chemically patterned surfaces that effect unique hydration water dynamics. *Proc. Natl. Acad. Sci. USA* **2018**, *115*, 8093–8098. [[CrossRef](#)]
30. Bar Dolev, M.; Dolev, M.B.; Braslavsky, I.; Davies, P.L. Ice-Binding Proteins and Their Function. *Annu. Rev. Biochem.* **2016**, *85*, 515–542. [[CrossRef](#)]
31. Mochizuki, K.; Molinero, V. Antifreeze glycoproteins bind reversibly to ice via hydrophobic groups. *J. Am. Chem. Soc.* **2018**, *140*, 4803–4811. [[CrossRef](#)] [[PubMed](#)]
32. Nada, H.; Furukawa, Y. growth inhibition mechanism of an ice–water interface by a mutant of winter flounder antifreeze protein: a molecular dynamics study. *J. Phys. Chem. B* **2008**, *112*, 7111–7119. [[CrossRef](#)] [[PubMed](#)]
33. Davies, P.L. Ice-binding proteins: A remarkable diversity of structures for stopping and starting ice growth. *Trends Biochem. Sci.* **2014**, *39*, 548–555. [[CrossRef](#)] [[PubMed](#)]
34. Knight, C.A. Adding to the antifreeze agenda. *Nature* **2000**, *406*, 249–251. [[CrossRef](#)]
35. Celik, Y.; Graham, L.A.; Mok, Y.-F.; Bar, M.; Davies, P.L.; Braslavsky, I. Superheating of ice crystals in antifreeze protein solutions. *Proc. Natl. Acad. Sci. USA* **2010**, *107*, 5423–5428. [[CrossRef](#)]
36. Scotter, A.J.; Marshall, C.B.; Graham, L.A.; Gilbert, J.A.; Garnham, C.P.; Davies, P.L. The basis for hyperactivity of antifreeze proteins. *Cryobiology* **2006**, *53*, 229–239. [[CrossRef](#)]
37. Zachariassen, K.E.; Li, N.G.; Laugsand, A.E.; Kristiansen, E.; Pedersen, S.A. Is the strategy for cold hardiness in insects determined by their water balance? A study on two closely related families of beetles: Cerambycidae and Chrysomelidae. *J. Comp. Physiol. B* **2008**, *178*, 977–984. [[CrossRef](#)]
38. Kristiansen, E.; Ramløv, H.; Højrup, P.; Pedersen, S.A.; Hagen, L.; Zachariassen, K.E. Structural characteristics of a novel antifreeze protein from the longhorn beetle Rhagium inquisitor. *Insect Biochem. Mol. Biol.* **2011**, *41*, 109–117. [[CrossRef](#)]
39. Liou, Y.-C.; Tocilj, A.; Davies, P.L.; Jia, Z. Mimicry of ice structure by surface hydroxyls and water of a β -helix antifreeze protein. *Nature* **2000**, *406*, 322–324. [[CrossRef](#)]
40. Leinala, E.K.; Davies, P.L.; Doucet, D.; Tyshenko, M.G.; Walker, V.K.; Jia, Z. A beta-helical antifreeze protein isoform with increased activity. Structural and functional insights. *J. Biol. Chem.* **2002**, *277*, 33349–33352. [[CrossRef](#)]
41. Hakim, A.; Nguyen, J.B.; Basu, K.; Zhu, D.F.; Thakral, D.; Davies, P.L.; Isaacs, F.J.; Modis, Y.; Meng, W. Crystal structure of an insect antifreeze protein and its implications for ice binding. *J. Biol. Chem.* **2013**, *288*, 12295–12304. [[CrossRef](#)] [[PubMed](#)]
42. Berendsen, H.J.C.; van der Spoel, D.; van Drunen, R. GROMACS: A message-passing parallel molecular dynamics implementation. *Comput. Phys. Commun.* **1995**, *91*, 43–56. [[CrossRef](#)]
43. Hoover, W.G. Canonical dynamics: Equilibrium phase-space distributions. *Phys. Rev. A Gen. Phys.* **1985**, *31*, 1695–1697. [[CrossRef](#)] [[PubMed](#)]
44. Nosé, S. A molecular dynamics method for simulations in the canonical ensemble. *Mol. Phys.* **1984**, *52*, 255–268. [[CrossRef](#)]

45. Berendsen, H.J.C.; Postma, J.P.M.; van Gunsteren, W.F.; DiNola, A.; Haak, J.R. Molecular dynamics with coupling to an external bath. *J. Chem. Phys.* **1984**, *81*, 3684–3690. [[CrossRef](#)]
46. MacKerell, A.D.; Bashford, D.; Bellott, M.; Dunbrack, R.L.; Evanseck, J.D.; Field, M.J.; Fischer, S.; Gao, J.; Guo, H.; Ha, S.; et al. All-atom empirical potential for molecular modeling and dynamics studies of proteins. *J. Phys. Chem. B* **1998**, *102*, 3586–3616. [[CrossRef](#)] [[PubMed](#)]
47. MacKerell, A.D.; Wiorkiewicz-Kuczera, J.; Karplus, M. An all-atom empirical energy function for the simulation of nucleic acids. *J. Am. Chem. Soc.* **1995**, *117*, 11946–11975. [[CrossRef](#)]
48. Abascal, J.L.F.; Vega, C. A general purpose model for the condensed phases of water: TIP4P/2005. *J. Chem. Phys.* **2005**, *123*, 234505. [[CrossRef](#)]
49. Engstler, J.; Giovambattista, N. Temperature Effects on Water-Mediated Interactions at the Nanoscale. *J. Phys. Chem. B* **2018**, *122*, 8908–8920. [[CrossRef](#)]
50. Choudhury, N.; Pettitt, B.M. On the mechanism of hydrophobic association of nanoscopic solutes. *J. Am. Chem. Soc.* **2005**, *127*, 3556–3567. [[CrossRef](#)] [[PubMed](#)]
51. Pentelute, B.L.; Gates, Z.P.; Tereshko, V.; Dashnau, J.L.; Vanderkooi, J.M.; Kossiakoff, A.A.; Kent, S.B.H. X-ray structure of snow flea antifreeze protein determined by racemic crystallization of synthetic protein enantiomers. *J. Am. Chem. Soc.* **2008**, *130*, 9695–9701. [[CrossRef](#)] [[PubMed](#)]
52. Leinala, E.K.; Davies, P.L.; Jia, Z. Crystal structure of β -helical antifreeze protein points to a general ice binding model. *Structure* **2002**, *10*, 619–627. [[CrossRef](#)]
53. Hudait, A.; Odendahl, N.; Qiu, Y.; Paesani, F.; Molinero, V. Ice-nucleating and antifreeze proteins recognize ice through a diversity of anchored clathrate and ice-like motifs. *J. Am. Chem. Soc.* **2018**, *140*, 4905–4912. [[CrossRef](#)] [[PubMed](#)]



© 2019 by the authors. Licensee MDPI, Basel, Switzerland. This article is an open access article distributed under the terms and conditions of the Creative Commons Attribution (CC BY) license (<http://creativecommons.org/licenses/by/4.0/>).

Article

Tetrahydrofuran (THF)-Mediated Structure of THF·(H₂O)_{n=1–10}: A Computational Study on the Formation of the THF Hydrate

Jinxiang Liu ^{1,2,*}, Yujie Yan ³, Youguo Yan ⁴ and Jun Zhang ^{4,*}

¹ School of Physics and Technology, University of Jinan, Jinan 250022, China

² School of Petroleum Engineering, China University of Petroleum, Qingdao, Shandong 266580, China

³ Shandong Academy of Environmental Science, Jinan 250013, China; yanyujiehappy@163.com

⁴ School of Materials Science and Engineering, China University of Petroleum, Qingdao 266580, China; yyg@upc.edu.cn

* Correspondence: sps_liujx@ujn.edu.cn (J.L.); sps_zhang@hotmail.com (J.Z.)

Received: 28 December 2018; Accepted: 29 January 2019; Published: 31 January 2019

Abstract: Tetrahydrofuran (THF) is well known as a former and a promoter of clathrate hydrates, but the molecular mechanism for the formation of these compounds is not yet well understood. We performed ab initio calculations and ab initio molecular dynamics simulations to investigate the formation, structure, and stability of THF·(H₂O)_{n=1–10} and its significance to the formation of the THF hydrate. Weak hydrogen bonds were found between THF and water molecules, and THF could promote water molecules from the planar pentagonal or hexagonal ring. As a promoter, THF could increase the binding ability of the CH₄, CO₂, or H₂ molecule onto a water face, but could also enhance the adsorption of other THF molecules, causing an enrichment effect.

Keywords: clathrate hydrate; tetrahydrofuran; formation; ab initio calculation

1. Introduction

Clathrate hydrates are ice-like crystalline compounds in which gas molecules are engaged in a host framework of water molecules, and they are widely found in permafrost and ocean floor sediments [1–3]. Up to now, three common types of methane hydrate structures have been identified [4,5]: The cubic structure I (sI), the cubic structure II (sII), and the hexagonal structure H (sH). The sI hydrate contains 2 small 5¹² cages and 6 5¹²6² cages per unit cell, and the sII hydrate has 16 5¹² cages and 8 5¹²6⁴ cages in one unit cell. The unit cell of the sH hydrate has three 5¹² cages, two 4³5⁶6³ cages, and one 5¹²6⁸ cage. Over the past few decades, clathrate hydrates have been considerably studied for scientific interest and various potential industrial applications [6–9]. However, high pressure and low temperature are required in the formation of clathrate hydrates, which thus limits the development of hydrate-based technology [10–12].

Thankfully, tetrahydrofuran (THF) molecules can form the sII hydrate at about room temperature and pressure [13], which can serve as a proxy for developing hydrate technology. Because of their large molecular size, THF molecules only occupy the large 5¹²6⁴ cages, leaving the small 5¹² cages vacant. More importantly, THF has been recognized as one of the most popular promoter molecules [14–18], which greatly reduces the formation pressure and/or increases the formation temperature of the mixed hydrate containing THF and a second guest component. Florusse et al. [19] have reported that hydrogen clusters can be stabilized and stored at a reduced pressure within the clathrate hydrate lattice by adding THF, where the small cages are occupied by hydrogen clusters and the large cages are singly occupied by THF. Recently, experiments [20] have shown that THF can remarkably stabilize clathrate hydrates with multigas guests (CH₄, C₂H₆, and C₃H₈) in moderate conditions, and its

concentration can also affect the distribution and preferential occupation of specific guest species in the cages. However, the molecular mechanism of formation of these compounds is not yet well understood [21,22].

Based on computer simulation methods [23], several hypotheses have been proposed to illustrate the microprocess of hydrate nucleation and growth, including a labile cluster hypothesis [24,25], a local structuring hypothesis [26], a blob mechanism [27], and a cage adsorption hypothesis [28]. Further, Wu and coworkers [29] have carried out a molecular dynamics study of the growth of the THF-CH₄ binary hydrate, and found that the growth rate is dominated by the adsorption of CH₄ to the growing interface and the migration and rearrangement of THF at the interface. Alavi and coworkers [30] have studied the hydrogen bonding of THF in binary sII hydrates via molecular dynamics simulations, and suggested that the number and nature of the second guests can affect the probability of hydrogen bonding of THF. Liu et al. [31] have studied the formation of the 5¹²6⁴ cage in the THF hydrate by sampling thermodynamically stable structures on the potential surface. Nevertheless, there have been only a limited number of computer simulation studies that have examined the microscopic mechanism of the initial formation process of the THF hydrate, i.e., the formation of the cage precursors, and our knowledge is still far from being complete.

In this work, we studied the interactions between THF and water molecules in spontaneously forming binary clusters of THF-(H₂O)_{n=1–10} by performing ab initio calculations. The results showed that the hydrogen bonds between THF and water were relatively weak, with a maximum number of two water molecules hydrogen bonded with THF, but THF could facilitate the rearrangement of water molecules to form a pentagonal or hexagonal planar ring, which was responsible for the formation of a clathrate cage. Further, THF could significantly enhance the attraction of water faces to a second-guest component, which is helpful in understanding the promotion effects of THF on clathrate hydrates of various gas molecules.

2. Computational Details

To obtain the initial configurations, we first added 1 THF and 100 water molecules into a simulation box with a size of 14.60 × 14.60 × 14.60 Å³ and performed ab initio molecular dynamics simulations in the canonical ensemble. The equations of motion were integrated with a time step of 0.5 fs, and the system was coupled with a Nosé–Hoover chain thermostat [32] to a bath at 300 K. After an equilibration period of 3.0 ps, THF and its nearest neighboring water molecules, up to 10, were in turn extracted from the periodic boxes and were fully optimized in a vacuum at zero temperature. The frequency analysis confirmed that the optimized structures were minima on the potential energy surface. All simulations and geometry optimizations were carried out by the DMol³ program [33]. The Perdew–Burke–Ernzerhof (PBE) gradient-corrected exchange-correlation functional [34] and the triple numerical plus polarization (TNP) basis set [35] were applied. The effects of the functionals and the basis sets were considered, and the compared results are given in Figure S10, Table S2, and Table S3 (in the Supplementary Materials). The semi-empirical Tkatchenko–Scheffler scheme [36] was used to improve the description of noncovalent forces.

The stability of the system was evaluated by the stabilization energy per molecule (E_{sta}) involving the zero-point vibrational energy correction, which was defined by

$$E_{sta} = \frac{(E_{THF} + n \cdot E_{water}) - E_{total}}{n + 1}, \quad (1)$$

where E_{THF} , E_{water} , and E_{total} represent the energy of the THF molecule, the water molecule, and the whole system, respectively. The binding strength of the gas molecule to the cluster was characterized by the interaction energy (E_{int}), defined as

$$E_{int} = (E_{residue} + E_{gas}) - E_{total}, \quad (2)$$

where E_{gas} represents the energy of the CH_4 , CO_2 , or H_2 molecule, and E_{residue} represents the energy of the whole system without the gas molecule.

3. Results and Discussion

3.1. THF-Mediated Formation of the Water Face

For a binary THF and water cluster ($n = 1\text{--}10$), five uncorrelated configurations were extracted from the equilibrated simulation trajectory (see Figure S1), and the optimized structures are given in Figure S2. The stabilization energies of all optimized $\text{THF}\cdot(\text{H}_2\text{O})_{n=1\text{--}10}$ clusters are shown in Figure 1, and the lowest-energy structures are shown in Figure 2. To observe whether hydrogen bonds could form between THF and water molecules, we analyzed the distance between H atoms of THF and their nearest O atoms of water molecules (Table S1), but the hydrogen bond did not occur. Instead, a hydrogen bond formed between the O atom of THF and the H atoms of water molecules, with a bond length ($\text{O}\cdots\text{H}$) of about $\sim 1.694 \text{ \AA}$. Obviously, THF could form two hydrogen bonds at most, with two water molecules above and/or below the plane of the THF ring.

For the lowest-energy structures of $\text{THF}\cdot(\text{H}_2\text{O})_{n=1\text{--}10}$ clusters, the stabilization energy increased almost linearly with the number of water molecules. In detail, the formation of double hydrogen bonds involving two water molecules was energetically more favorable than the formation of a single hydrogen bond involving one water molecule, featuring a stabilization energy of 0.216 eV and 0.177 eV, respectively. For the $\text{THF}\cdot(\text{H}_2\text{O})_3$ cluster, two water molecules formed two hydrogen bonds with THF, while the third water molecule formed one hydrogen bond with another water molecule. In the $\text{THF}\cdot(\text{H}_2\text{O})_4$ cluster, three water molecules below the THF ring had a trend of forming a ternary ring, but such a process was inhibited because of the stereo-hindrance and hydrophobic effects of the THF ring. By sequential addition of one more water molecule, the water–water interactions were greatly enhanced, and a planar ternary ring of water molecules formed on one side of the THF ring for the $\text{THF}\cdot(\text{H}_2\text{O})_5$ cluster. This suggested that a quasiplanar cyclic structure of the water molecules would be energetically favorable, agreeing well with the theoretical results of Shields et al. [37], and thus this structure would considerably occur during the formation of the clathrate cage. Further, the ternary face of water molecules was nearly parallel to the THF ring because of the hydrophobic interactions between THF and water. For the $\text{THF}\cdot(\text{H}_2\text{O})_6$ cluster, there were two cyclic hydrogen bonded networks, that is, a pentagonal ring involving THF and four water molecules and a ternary ring involving three water molecules. Interestingly, the THF–water hydrogen bonds were nearly vertical to the plane composed of water molecules in the pentagonal ring, while three water molecules in the ternary ring were coplanar. The dihedral angle between two water faces was about 123.8° , which was in the range of the value of the neighbor faces in the clathrate hydrate ($119.9^\circ\text{--}133.3^\circ$), suggesting that the water molecules cooperatively organized into a stable structure.

In the case of $\text{THF}\cdot(\text{H}_2\text{O})_7$, a single planar pentagonal ring of water face emerged and was roughly parallel to the THF ring, despite the formation of a THF–water hydrogen bond. This observation of THF–water cooperating toward ordering was similar to previous studies by Walsh et al. [22] that showed that methane molecules adsorbed on opposite sides of a pentagonal face of water molecules in the hydrate nucleation, which in turn allowed the adsorption of more water molecules. However, our observations showed that this initial structure formed through THF mediating the arrangement of water molecules instead of the formation of a pentagonal water face followed by adsorbing THF. For one more adsorbed water molecule, it preferentially inserted into the pentagonal water ring, leading to the formation of the hexagonal water face. The stabilization energy increased from 0.377 eV to 0.407 eV, implying that this process was energetically feasible.

By sequentially increasing the number of water molecules, we found that the cyclic rings composed of five or six water molecules were most likely to occur, while the larger cyclic rings were thermodynamically unstable. As a result, a cage-like structure gradually formed, just like $\text{THF}\cdot(\text{H}_2\text{O})_{10}$. In contrast, we investigated the $\text{CH}_4\cdot(\text{H}_2\text{O})_{10}$, $\text{CO}_2\cdot(\text{H}_2\text{O})_{10}$, and $\text{H}_2\cdot(\text{H}_2\text{O})_{10}$ clusters by

the same procedure, and the optimized structures are shown in Figures S5, S7, and S9. The stabilization energy was 0.389 eV, 0.383 eV, and 0.350 eV for the most stable structures of $\text{CH}_4\cdot(\text{H}_2\text{O})_{10}$, $\text{CO}_2\cdot(\text{H}_2\text{O})_{10}$, and $\text{H}_2\cdot(\text{H}_2\text{O})_{10}$ clusters, respectively. These values were much smaller than those of $\text{THF}\cdot(\text{H}_2\text{O})_{10}$ (0.448 eV), implying that THF was more thermodynamically feasible in rearranging water molecules to form a cage precursor. Further, we note that CH_4 , CO_2 , and H_2 were likely to promote the spontaneous formation of pentagonal water faces, but THF could induce the formation of both pentagonal and hexagonal faces, which explained how THF occupied the $5^{12}6^4$ cage in the sII hydrate.

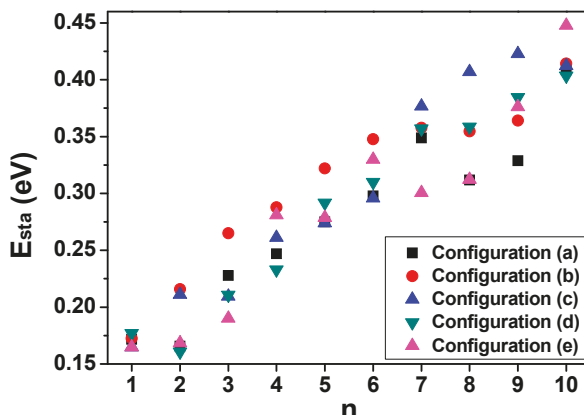


Figure 1. The stabilization energy (E_{sta} , with zero-point energy corrections) of binary $\text{THF}\cdot(\text{H}_2\text{O})_{n=1-10}$ clusters calculated at the Perdew–Burke–Ernzerhof (PBE) gradient-corrected exchange-correlation functional (PBE-D)/triple numerical plus polarization (TNP) level. The optimized geometries of $\text{THF}\cdot(\text{H}_2\text{O})_{n=1-10}$ clusters are given in Figure S2. THF: Tetrahydrofuran.

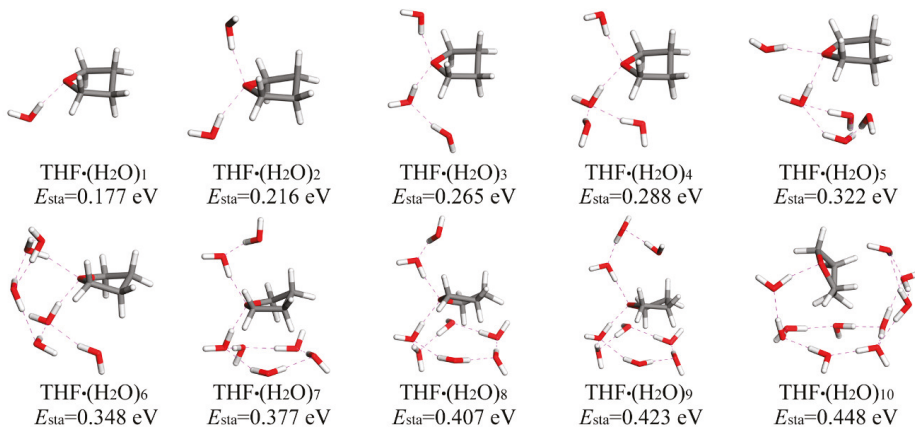


Figure 2. The most stable structures of binary $\text{THF}\cdot(\text{H}_2\text{O})_{n=1-10}$ clusters and their stabilization energies optimized at the PBE-D/TNP level. The hydrogen bonds are shown with violet dashed lines.

3.2. THF Enhanced the Binding Strength of a Gas Molecule

The above analysis suggests that THF could promote the formation and growth of water faces, and in the following part we will show that THF could also enhance the adsorption of a second gas molecule. First, we constructed a system consisting of THF and a pentagonal water ring and considered its attraction to CH_4 , CO_2 , H_2 , and other THF molecules. Figure 3 shows that there were two low-energy structures for $\text{THF}\cdot(\text{H}_2\text{O})_5$, where the THF ring was roughly vertical or parallel

to the pentagonal ring of water molecules, and the stabilization energy was 0.379 eV and 0.382 eV, respectively. This thus suggested that $\text{THF}\cdot(\text{H}_2\text{O})_5$ was likely to form a two-layer structure through a hydrogen bond between the O atom of THF and the H atom of a water molecule, in accordance with the aforementioned results.

The stabilization energy of the pentagonal water face plus a gas molecule (CH_4 , CO_2 , and H_2), the interaction energy, and the distance between them without and with adding an additional THF molecule are given in Table 1. The optimized structures of the pentagonal water face plus THF and a gas molecule are shown in Figure 3. It can be seen that CH_4 favored adsorbing on one side of the pentagonal water face and had a distance of 3.004 Å to the centroid of the pentagonal ring. The stabilization energy of this $(\text{CH}_4)_1\cdot(\text{H}_2\text{O})_5$ cluster was 0.325 eV, and the interaction energy between CH_4 and the pentagonal ring was 0.358 eV. Upon the addition of THF on the opposite side of the pentagonal water face, CH_4 became a little farther away from the pentagonal ring (3.100 Å), but the stability of the system was greatly enhanced ($E_{\text{sta}} = 0.346$ eV), and the attraction of the pentagonal ring to the CH_4 was also strengthened ($E_{\text{int}} = 0.362$ eV), thus improving the interactions between the pentagonal water faces and CH_4 molecules. Similarly, by adding THF, the distance between the pentagonal ring and CO_2 was elongated by 0.085 Å, and the stabilization energy was increased by 0.039 eV, which was almost equal to CH_4 (0.085 Å and 0.021 eV). However, the interaction energy between the pentagonal ring and CO_2 was considerably increased by 0.114 eV, implying that THF could more significantly improve the adsorption of CO_2 molecules than CH_4 molecules. In contrast, THF had little effect on the distance between the pentagonal ring and H_2 ($\Delta d = 0.017$ Å), because of the small size of H_2 molecules (non-heavy atom); However, the stabilization energy was increased by 0.061 eV, which was more significant than that of CH_4 and CO_2 , although the interaction energy was just increased by 0.012 eV.

In the case of THF as a guest molecule, we found that two THF molecules favored adsorbing on opposite sides of the pentagonal water ring and retained their positions throughout the formation of hydrogen bonds with water molecules, leading to a sandwich structure, as shown in Figure 3. Interestingly, two THF molecules could not bind to one water molecule, agreeing well with the previous results of Shultz and Vu [38], which suggested that water did not form a bridging donor–donor structure with two THF molecules. Instead, the additional THF molecule joined with a different free water molecule, forming a cluster enriched in THF. From Table 1, we can see that the additional THF molecule enhanced the structural stability and the adsorption strength of the water face to THF, although THF had a larger distance to the water face. Therefore, THF was favorable for the pentagonal water face to adsorb CH_4 , CO_2 , H_2 , or other THF molecules to form a cage precursor.

Subsequently, we constructed another system consisting of THF and a hexagonal water ring and considered its attraction to CH_4 , CO_2 , H_2 , and other THF molecules. The stabilization energy of the hexagonal water face with a guest molecule (CH_4 , CO_2 , H_2 , and THF), the interaction energy, and the distance between them without and with adding an additional THF molecule are given in Table 2. The optimized structures for all considered clusters are shown in Figure 4. It can be seen that the adsorbed THF ring could be either vertical or parallel to the hexagonal water face, with a stabilization energy of 0.384 eV and 0.392 eV, respectively. This indicated that THF was likely parallel to the hexagonal water face due to the formation of an extra hydrogen bond, which was similar to the case of the pentagonal water face. However, the THF became much closer to the hexagonal face than the pentagonal face (3.327 Å vs 3.431 Å), because the stereo-hindrance and hydrophilic–hydrophobic effects were weakened by the larger radius of the hexagonal ring.

For CH_4 , CO_2 , and H_2 molecules, they all preferentially located themselves along the central axis of the hexagonal water ring, and the distance between the center of the hexagonal ring and the guest molecule was 2.729, 2.715, and 2.161 Å, respectively. These distances were much smaller than the cases of the pentagonal water ring, which could be attributed to the weak stereo-hindrance effect caused by the large radius of the hexagonal ring. Upon adding one THF molecule on the opposite side of the hexagonal water ring, the distance was slightly elongated to 2.773, 2.749, and 2.276 Å for the CH_4 ,

CO_2 , and H_2 molecules, respectively: The stabilization energy was increased by 0.024 eV, 0.019 eV, and 0.061 eV, respectively, and the interaction energy was increased by 0.006 eV, 0.082 eV, and 0.028 eV, respectively. These scenarios were quite similar to those of the pentagonal water ring, suggesting that THF could enhance the stability of the initial structure of the large cages but also improve the adsorption of CH_4 , CO_2 , and H_2 molecules to the hexagonal water face.

Table 1. The stabilization energy (E_{sta}), the interaction energy (E_{int}), and the distance (d) between the guest (CH_4 , CO_2 , H_2 , and THF) and the pentagonal water ring calculated at the PBE-D/TNP level.

Guest	E_{sta} (eV)		E_{int} (eV)		d (Å)	
	without THF	with THF	without THF	with THF	without THF	with THF
CH_4	0.325	0.346	0.358	0.362	3.004	3.100
CO_2	0.326	0.365	0.389	0.502	2.861	2.946
H_2	0.279	0.340	0.112	0.124	2.497	2.514
THF	0.382	0.399	0.812	0.816	3.431	3.481

Table 2. The stabilization energy (E_{sta}), the interaction energy (E_{int}), and the distance (d) between the guest (CH_4 , CO_2 , H_2 , and THF) and the hexagonal water ring calculated at the PBE-D/TNP level.

Guest	E_{sta} (eV)		E_{int} (eV)		d (Å)	
	without THF	with THF	without THF	with THF	without THF	with THF
CH_4	0.340	0.364	0.444	0.450	2.729	2.773
CO_2	0.352	0.371	0.559	0.641	2.715	2.749
H_2	0.294	0.355	0.128	0.156	2.161	2.276
THF	0.394	0.411	0.893	0.902	3.327	3.364

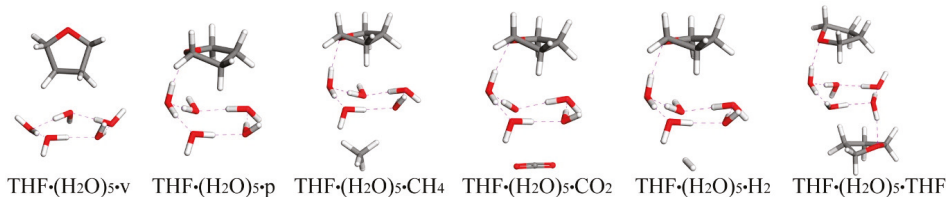


Figure 3. Low-energy structures of the clusters of THF plus a pentagonal ring of water molecules and/or $\text{CH}_4/\text{CO}_2/\text{H}_2/\text{THF}$ optimized at the PBE-D/TNP level. The hydrogen bonds are shown with violet dashed lines.

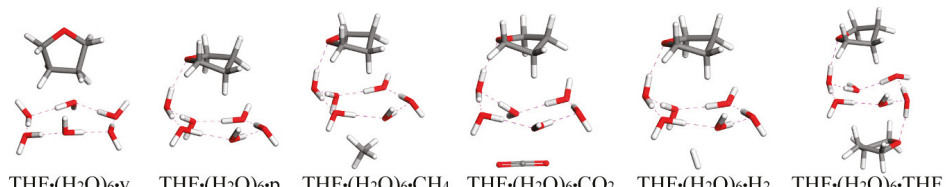


Figure 4. Low-energy structures of the clusters of THF plus a hexagonal ring of water molecules and/or $\text{CH}_4/\text{CO}_2/\text{H}_2/\text{THF}$ optimized at the PBE-D/TNP level. The hydrogen bonds are shown with violet dashed lines.

4. Conclusions

In the present work, we carried out ab initio studies of $\text{THF}\cdot(\text{H}_2\text{O})_{n=1-10}$ clusters to reveal the initial process of the formation of the THF hydrate. Although THF had a weak hydrogen bond with water molecules, it could significantly promote the rearrangement of water molecules to form a planar

pentagonal or hexagonal ring, which was responsible for the formation of water faces of a clathrate cage. As a promoter, THF could greatly improve the stability of the cage precursors for the CH₄, CO₂, and H₂ hydrates and enhance the interactions between the water faces and these gas molecules. Further, our results also suggested that THF could facilitate the adsorption of other THF molecules, resulting in an enrichment effect.

Supplementary Materials: The following are available online at <http://www.mdpi.com/2073-4352/9/2/73/s1>. Figure S1. Initial configurations of five uncorrelated THF-(H₂O)_{n=1-10} clusters extracted from the ab initio molecular dynamics simulation trajectory. Figure S2. Optimized configurations of five uncorrelated THF-(H₂O)_{n=1-10} clusters. Figure S3. Labels of H atoms of the THF molecule. Figure S4. Initial configurations of five uncorrelated CH₄-(H₂O)₁₀ clusters, which were obtained by the same procedure as the THF-(H₂O)_{n=1-10} clusters. Figure S5. Optimized configurations of five uncorrelated CH₄-(H₂O)₁₀ clusters and their stabilization energies, optimized at the PBE-D/TNP level. Figure S6. Initial configurations of five uncorrelated CO₂-(H₂O)₁₀ clusters, which were obtained by the same procedure as the THF-(H₂O)_{n=1-10} clusters. Figure S7. Optimized configurations of five uncorrelated CO₂-(H₂O)₁₀ clusters and their stabilization energies, optimized at the PBE-D/TNP level. Figure S8. Initial configurations of five uncorrelated H₂-(H₂O)₁₀ clusters, which were obtained by the same procedure as the THF-(H₂O)_{n=1-10} clusters. Figure S9. Optimized configurations of five uncorrelated H₂-(H₂O)₁₀ clusters and their stabilization energies, optimized at the PBE-D/TNP level. Figure S10. The stabilization energies of the THF-(H₂O)_{n=1-10} clusters shown in Figure 2, calculated at the different levels. Table S1. The distance between H atoms of the THF molecule and their nearest O atoms of water molecules. Table S2. The stabilization energy (Esta) of the pentagonal water ring plus a guest (CH₄, CO₂, H₂, and THF), calculated at the different functionals and basis sets. Table S3. The stabilization energy (Esta) of the hexagonal water ring plus a guest (CH₄, CO₂, H₂, and THF), calculated at the different functionals and basis sets.

Author Contributions: Methodology, Y.Y. (Yujie Yan); investigation, Y.Y. (Youguo Yan) and J.Z.; writing—review and editing, J.L.

Funding: This work was supported by the National Natural Science Foundation of China [Grant number 11504133], the China Postdoctoral Science Foundation [Grant number 2017M612376], and the Postdoctoral Application Research Project of Qingdao [Grant number 2016216].

Conflicts of Interest: The authors declare no conflict of interest.

References

- McMullan, R.K.; Jeffrey, G.A. Polyhedral Clathrate Hydrates. IX. Structure of Ethylene Oxide Hydrate. *J. Chem. Phys.* **1965**, *42*, 2725–2732. [[CrossRef](#)]
- Mak, T.C.W.; McMullan, R.K. Polyhedral Clathrate Hydrates. X. Structure of the Double Hydrate of Tetrahydrofuran and Hydrogen Sulfide. *J. Chem. Phys.* **1965**, *42*, 2732–2737. [[CrossRef](#)]
- Ripmeester, J.A.; Tse, J.S.; Ratcliffe, C.I.; Powell, B.M. A New Clathrate Hydrate Structure. *Nature* **1987**, *325*, 135–136. [[CrossRef](#)]
- Sloan, E.D. Fundamental Principles and Applications of Natural Gas Hydrates. *Nature* **2003**, *426*, 353–363. [[CrossRef](#)] [[PubMed](#)]
- Zhu, J.; Du, S.; Yu, X.; Zhang, J.; Xu, H.; Vogel, S.C.; Germann, T.C.; Francisco, J.S.; Izumi, F.; Momma, K.; et al. Encapsulation Kinetics and Dynamics of Carbon Monoxide in Clathrate Hydrate. *Nat. Commun.* **2014**, *5*, 4128. [[CrossRef](#)]
- Dickens, G.R. A Methane Trigger for Rapid Warming? *Science* **2003**, *299*, 1017. [[CrossRef](#)]
- Lee, H.; Lee, J.-W.; Kim, D.Y.; Park, J.; Seo, Y.-T.; Zeng, H.; Moudrakovski, I.L.; Ratcliffe, C.I.; Ripmeester, J.A. Tuning Clathrate Hydrates for Hydrogen Storage. *Nature* **2005**, *434*, 743–746. [[CrossRef](#)]
- Liu, J.; Hou, J.; Xu, J.; Liu, H.; Chen, G.; Zhang, J. Ab Initio Study of the Molecular Hydrogen Occupancy in Pure H₂ and Binary H₂-THF Clathrate Hydrates. *Int. J. Hydrogen Energy* **2017**, *42*, 17136–17143. [[CrossRef](#)]
- Sun, Q.; Kang, Y.T. Experimental Correlation for the Formation Rate of CO₂ Hydrate with THF (Tetrahydrofuran) for Cooling Application. *Energy* **2015**, *91*, 712–719. [[CrossRef](#)]
- Yang, H.; Fan, S.; Lang, X.; Wang, Y. Phase Equilibria of Mixed Gas Hydrates of Oxygen+Tetrahydrofuran, Nitrogen+Tetrahydrofuran, and Air+Tetrahydrofuran. *J. Chem. Eng. Data* **2011**, *56*, 4152–4156. [[CrossRef](#)]
- Mao, W.L.; Mao, H.-K.; Goncharov, A.F.; Struzhkin, V.V.; Guo, Q.; Hu, J.; Shu, J.; Hemley, R.J.; Somayazulu, M.; Zhao, Y. Hydrogen Clusters in Clathrate Hydrate. *Science* **2002**, *297*, 2247–2249. [[CrossRef](#)] [[PubMed](#)]
- Shin, W.; Park, S.; Koh, D.-Y.; Seol, J.; Ro, H.; Lee, H. Water-Soluble Structure H Clathrate Hydrate Formers. *J. Phys. Chem. C* **2011**, *115*, 18885–18889. [[CrossRef](#)]

13. Makino, T.; Sugahara, T.; Ohgaki, K. Stability Boundaries of Tetrahydrofuran+Water System. *J. Chem. Eng. Data* **2005**, *50*, 2058–2060. [[CrossRef](#)]
14. Yang, M.; Jing, W.; Zhao, J.; Ling, Z.; Song, Y. Promotion of Hydrate-Based CO₂ Capture from Flue Gas by Additive Mixtures (THF (Tetrahydrofuran)+TBAB (Tetra-N-Butyl Ammonium Bromide)). *Energy* **2016**, *106*, 546–553. [[CrossRef](#)]
15. Koh, D.-Y.; Kang, H.; Lee, H. Multiple Guest Occupancy in Clathrate Hydrates and Its Significance in Hydrogen Storage. *Chem. Commun.* **2013**, *49*, 6782–6784.
16. Zhang, B.; Wu, Q. Thermodynamic Promotion of Tetrahydrofuran on Methane Separation from Low-Concentration Coal Mine Methane Based on Hydrate. *Energy Fuel* **2010**, *24*, 2530–2535. [[CrossRef](#)]
17. Alavi, S.; Ripmeester, J.A.; Klug, D.D. Molecular-Dynamics Simulations of Binary Structure II Hydrogen and Tetrahydrofuran Clathrates. *J. Chem. Phys.* **2006**, *124*, 014704. [[CrossRef](#)]
18. Lee, Y.-J.; Kawamura, T.; Yamamoto, Y.; Yoon, J.-H. Phase Equilibrium Studies of Tetrahydrofuran (THF)+CH₄, THF+CO₂, CH₄+CO₂, and THF+CO₂+CH₄ Hydrates. *J. Chem. Eng. Data* **2012**, *57*, 3543–3548. [[CrossRef](#)]
19. Florusse, L.J.; Peters, C.J.; Schoonman, J.; Hester, K.C.; Koh, C.A.; Dec, S.F.; Marsh, K.N.; Sloan, E.D. Stable Low-Pressure Hydrogen Clusters Stored in a Binary Clathrate Hydrate. *Science* **2004**, *306*, 469–471. [[CrossRef](#)]
20. Lee, S.; Lee, Y.; Park, S.; Kim, Y.; Cha, I.; Seo, Y. Stability Conditions and Guest Distribution of the Methane+Ethane+Propane Hydrates or Semiclathrates in the Presence of Tetrahydrofuran or Quaternary Ammonium Salts. *J. Chem. Thermodyn.* **2013**, *65*, 113–119.
21. Sosso, G.C.; Chen, J.; Cox, S.J.; Fitzner, M.; Pedevilla, P.; Zen, A.; Michaelides, A. Crystal Nucleation in Liquids: Open Questions and Future Challenges in Molecular Dynamics Simulations. *Chem. Rev.* **2016**, *116*, 7078–7116. [[CrossRef](#)] [[PubMed](#)]
22. Walsh, M.R.; Koh, C.A.; Sloan, E.D.; Sum, A.K.; Wu, D.T. Microsecond Simulations of Spontaneous Methane Hydrate Nucleation and Growth. *Science* **2009**, *326*, 1095–1098. [[CrossRef](#)] [[PubMed](#)]
23. English, N.J.; MacElroy, J.M.D. Perspectives on Molecular Simulation of Clathrate Hydrates: Progress, Prospects and Challenges. *Chem. Eng. Sci.* **2015**, *121*, 133–156. [[CrossRef](#)]
24. Sloan, E.D.; Fleyfel, F. A Molecular Mechanism for Gas Hydrate Nucleation from Ice. *AIChE J.* **1991**, *37*, 1281–1292. [[CrossRef](#)]
25. Christiansen, R.L.; Sloan, E.D. Mechanisms and Kinetics of Hydrate Formation. *Ann. N. Y. Acad. Sci.* **1994**, *715*, 283–305. [[CrossRef](#)]
26. Radhakrishnan, R.; Trout, B.L. A New Approach for Studying Nucleation Phenomena Using Molecular Simulations: Application to CO₂ Hydrate Clathrates. *J. Chem. Phys.* **2002**, *117*, 1786–1796. [[CrossRef](#)]
27. Jacobson, L.C.; Hujo, W.; Molinero, V. Amorphous Precursors in the Nucleation of Clathrate Hydrates. *J. Am. Chem. Soc.* **2010**, *132*, 11806–11811. [[CrossRef](#)]
28. Guo, G.-J.; Li, M.; Zhang, Y.-G.; Wu, C.-H. Why Can Water Cages Adsorb Aqueous Methane? A Potential of Mean Force Calculation on Hydrate Nucleation Mechanisms. *Phys. Chem. Chem. Phys.* **2009**, *11*, 10427–10437. [[CrossRef](#)]
29. Wu, J.-Y.; Chen, L.-J.; Chen, Y.-P.; Lin, S.-T. Molecular Dynamics Study on the Growth Mechanism of Methane Plus Tetrahydrofuran Mixed Hydrates. *J. Phys. Chem. C* **2015**, *119*, 19883–19890. [[CrossRef](#)]
30. Alavi, S.; Ripmeester, J.A. Effect of Small Cage Guests on Hydrogen Bonding of Tetrahydrofuran in Binary Structure II Clathrate Hydrates. *J. Chem. Phys.* **2012**, *137*, 054712. [[CrossRef](#)]
31. Liu, J.; Shi, S.; Zhang, Z.; Liu, H.; Xu, J.; Chen, G.; Hou, J.; Zhang, J. Ab Initio Study of Formation of the Clathrate Cage in the Tetrahydrofuran Hydrate. *J. Chem. Thermodyn.* **2018**, *120*, 39–44. [[CrossRef](#)]
32. Nosé, S. A Molecular Dynamics Method for Simulations in the Canonical Ensemble. *Mol. Phys.* **1984**, *52*, 255–268. [[CrossRef](#)]
33. Tang, L.-G.; Li, X.-S.; Feng, Z.-P.; Li, G.; Fan, S.-S. Control Mechanisms for Gas Hydrate Production by Depressurization in Different Scale Hydrate Reservoirs. *Energy Fuel* **2007**, *21*, 227–233. [[CrossRef](#)]
34. Perdew, J.P.; Burke, K.; Ernzerhof, M. Generalized Gradient Approximation Made Simple. *Phys. Rev. Lett.* **1996**, *77*, 3865–3868. [[CrossRef](#)] [[PubMed](#)]
35. Delley, B. Ground-State Enthalpies: Evaluation of Electronic Structure Approaches with Emphasis on the Density Functional Method. *J. Phys. Chem. A* **2006**, *110*, 13632–13639. [[CrossRef](#)] [[PubMed](#)]
36. Tkatchenko, A.; Scheffler, M. Accurate Molecular Van Der Waals Interactions from Ground-State Electron Density and Free-Atom Reference Data. *Phys. Rev. Lett.* **2009**, *102*, 073005. [[CrossRef](#)] [[PubMed](#)]

37. Cox, S.J.; Towler, M.D.; Alfè, D.; Michaelides, A. Benchmarking the Performance of Density Functional Theory and Point Charge Force Fields in Their Description of Si Methane Hydrate against Diffusion Monte Carlo. *J. Chem. Phys.* **2014**, *140*, 174703. [[CrossRef](#)]
38. Shultz, M.J.; Vu, T.H. Hydrogen Bonding between Water and Tetrahydrofuran Relevant to Clathrate Formation. *J. Phys. Chem. B* **2015**, *119*, 9167–9172. [[CrossRef](#)]



© 2019 by the authors. Licensee MDPI, Basel, Switzerland. This article is an open access article distributed under the terms and conditions of the Creative Commons Attribution (CC BY) license (<http://creativecommons.org/licenses/by/4.0/>).

MDPI
St. Alban-Anlage 66
4052 Basel
Switzerland
Tel. +41 61 683 77 34
Fax +41 61 302 89 18
www.mdpi.com

Crystals Editorial Office
E-mail: crystals@mdpi.com
www.mdpi.com/journal/crystals



MDPI
St. Alban-Anlage 66
4052 Basel
Switzerland

Tel: +41 61 683 77 34
Fax: +41 61 302 89 18
www.mdpi.com



ISBN 978-3-03921-891-2